Astrometry of 6.7 GHz Methanol Maser Sources and the Bar Structure of the Milky Way Galaxy

Naoko MATSUMOTO

Doctor of Philosophy

Department of *Astronomical Science*
School of *Physical Science*
The Graduate University for Advanced Studies

2010

Abstract

The goal of this thesis is to kinematically establish the existence of the bar structure in the Milky Way Galaxy based on VLBI astrometry of masers in star-forming regions. To achieve this goal, the thesis consists of three parts described below.

First, we measured annual parallax and absolute proper motions of the 6.7 GHz methanol maser source W3(OH) with the JVN/VERA (Japanese VLBI Network / VLBI Exploration of Radio Astrometry). We derived the trigonometric annual parallax to be 0.633 ± 0.112 mas, corresponding to a distance of $1.58^{+0.34}_{-0.24}$ kpc. This is the first detection of a parallax for 6.7 GHz methanol maser with the JVN/VERA, and demonstrates that the JVN/VERA is capable of conducting VLBI astrometry for 6.7 GHz methanol maser sources within a few kpc from the Sun. We also measured the internal proper motions of 6.7 GHz methanol maser of W3(OH) for the first time. The internal proper motions basically show north-south expansion with velocities of few km s^{-1}, being similar to OH masers. The global distributions and the internal proper motions of 6.7 GHz methanol masers suggest a rotating and expanding torus structure surrounding ultracompact H II region. We also obtained averaged absolute proper motions for all six spots of W3(OH), which is $\mu_\alpha \cos\delta = -1.10 \pm 0.30$ mas yr^{-1} and $\mu_\delta = -0.16 \pm 0.38$ mas yr^{-1}. The accuracy of the absolute proper motion obtained here indicates that we will be able to detect the non-circular motion caused by the Galactic bar, which is expected to be an order of sub-mas yr^{-1}.

Next, we conducted the fringe check observations to select observable target sources toward the Galactic bar. We selected sources from the 6.7 GHz methanol maser catalog of Pestalozzi et al. (2005). In our sources selection, we used four criteria as follows: First, sources must have the galactic longitude $|l| < 40^\circ$ and Dec> -37 deg. Second, the sources must have a galacto-centric radius less than 5 kpc, which is estimated from the kinematic distance. Third, we chose strong sources with the flux are 15 Jy or more at single dish observations except some sources that were specially included to investigate the detection limit for the flux under the 15 Jy. Fourth, the maser sources must have one or more detectable reference sources with the JVN or the VERA within 4 degree separations from the maser sources. In this

selection, we chose the reference sources with the peak flux about 100 mJy beam^{-1} or more at 8 GHz (X-band) in the VLBA Calibrator Survey. The fringe check observations were conducted with six sessions from October 2008 to June 2009 with the JVN/VERA. In total, 75 maser sources were observed. 26 maser sources were detected with signal to noise ratio of more than 5σ at the baseline of about 1,000 km or longer in the 75 sources, corresponding to the detection rate of about 35%.

For astrometric observations, out of the 26 sources detected in the fringe check observations, we chose ten maser sources, which are easy to observe with phase referencing because of high flux at longer than 1,000 km VERA baselines and suitable reference sources. These ten sources were G 353.4−0.36, G 351.41+0.64, G 30.76−0.05, G 29.95−0.02, G 28.14+0.00, G 25.70−0.04, G 25.65+1.04, G 24.78+0.08, G 23.01−0.41 and G 9.98−0.02. We obtained the three dimensional velocities with VLBI phase-reference observations. With these data sets for 2, 3 or 4 epochs, we fitted linear proper motions with least-square fittings without a parameter of annual parallax. Finally, we obtained the suitable proper motions for nine sources.

By combining our data with previous results from the VERA/VLBA, we compared the 3-D data of star forming regions with the flat/non-flat circular rotation models and a dynamical model proposed by Wada (1994) and Sakamoto et al. (1999). We find clearly a deviation from the flat/non-flat circular rotation models in the absolute proper motions at the three dimension of (l, $\mu_l \cos b$, $V_{\rm LSR}$). Around the maximum region of $V_{\rm LSR}$, the absolute proper motions are smaller than the flat rotation model for the five sources out of eight. From the dynamical models and VLBI data, an acceptable parameter of the inclination angle of the Galactic bar are derived as $\sim 30^\circ$ - 50°, which is consistent with previous studies. Thus, with the existence of the Galactic bar, observed proper motions with VLBI can be explained better.

Acknowledgements

I am deeply grateful to my supervisor, associate professor Mareki HONMA for his useful advices and fruitful discussions. I would like to express my gratitude to my second supervisor, associate professor Katsunori SHIBATA for his support of observations for this study and helpful advices. I would also like to thank my third supervisor, assistant professor Tomoya HIROTA for his useful advice for data reductions and scientific discussions for the star formation and astrometry.

I would like to appreciate to professor Kenta FUJISAWA, Dr. Satoko SAWADA-SATOH, Dr. Akihiro DOI, student Koichiro SUGIYAMA and Yasuko ISONO for their supports of observations, data reductions and useful discussions about this study especially for W3(OH). I also thank assistant professor Takaaki JIKE and research engineer Takeshi BUSHIMATA for correlations of VLBI data for this study, and Dr. Tomoharu KURYAMA for helpful support of UVW recalculation in the data reduction of this study. I also thank student Kouhei MATSUMOTO for his support for 6.7 GHz receiver and photo credit of VERA receivers. I would like to thank Dr. Nanako MOCHIZUKI for antenna operations of Usuda 64 m telescope. I would also like to thank Dr. Tomoaki OYAMA for his useful advice of data reduction and scientific planning. I would also like to appreciate to student Kazuyoshi YAMASHITA for his advice of data reduction and his useful tool. I also thank Dr. Tomofumi UMEMOTO for his helpful advice about star forming region. I also thank student Kazuhiro HADA, Kenta SUZUKI for advice about data reductions. I would like to thank professor Hiroyuki NAKANISHI for his figure of longitude-velocity maps of H I and CO emissions. I also thank professor Keiichi WADA for his useful comments for this study and introducing his bar model. I also appreciate to associate professor Shuji DEGUCHI for his useful advisor about discussion of kinematics with bar model in this study. I also thank student Kazunori AKIYAMA for his support of observational data obtaining, Mayumi SATOH for her useful advice for data reduction. I want to thank student Mikyong KIM for her helps in my research life. I also thank engineers, scientists and students in Mizusawa VLBI observatory (NAOJ) and staffs and students in Kagoshima University for their help. Finally, I would like to thank

my parents, my sisters, my grandparents, my uncles, my aunt and my dears.

This study is supported by Grant-in-Aid for JSPS Fellows.

Contents

Abstract **ii**

Acknowledgements **iv**

1 Introduction **1**

1.1 The Bar of the Milky Way Galaxy 1

1.2 VLBI Astrometry 8

1.3 Aim of This Thesis 16

2 6.7 GHz Methanol Maser Toward W3(OH) Ultracompact H II Region **17**

2.1 Introduction 17

2.2 Observations and Data Analysis 19

2.2.1 Observations 19

2.2.2 In-beam and Phase-referencing Mappings 20

2.2.3 Derivation of Internal Proper Motions 22

2.2.4 Derivation of Annual Parallax and Absolute Proper Motion . . 22

2.3 Results 25

2.3.1 Spatial Distribution and Internal Proper Motion 25

2.3.2 Parallax and Absolute Proper Motion 28

2.4 Discussion 32

2.4.1 Astrometry with the VERA/JVN 32

2.4.2 Structure of Maser Emitting Region 33

2.4.3 Conclusion 36

3 Fringe Check Observations of 6.7 GHz Methanol Maser with the VERA/JVN 39

3.1 Introduction 39
3.2 Source Selection 40
3.2.1 Criteria for Source Selection 40
3.2.2 Fringe Check Observations 44
3.3 Data Analysis 45
3.4 Results and Discussion of Fringe Check Observations 46

4 The Molecular Gas Motion with the Bar Structure of the Milky Way Galaxy 56

4.1 Introduction 56
4.2 Observations 56
4.3 Data Analysis 60
4.4 Results 61
4.5 Discussion 62
4.5.1 Flat Circular Rotation Model 68
4.5.2 Non-flat Circular Rotation Model 71
4.5.3 Damped Oval Orbit Model 79
4.6 Summary 88

5 Conclusions 94

5.1 Conclusions 94
5.2 Future Works 95

Bibliography 97

A Spectra and Maps of the 6.7 GHz Methanol Maser Sources in Chapter 4 107

Chapter 1

Introduction

1.1 The Bar of the Milky Way Galaxy

The Milky Way Galaxy is believed to be a barred spiral galaxy from various observational and theoretical studies like figure 1.1. de Vaucouleurs (1964) first proposed that the Milky Way Galaxy is a barred galaxy from the large positive and negative velocities in the H I profiles near the galactic center and the spiral pattern of other SAB(r) or SAB(rs) galaxies. Since then, there have been many studies on the Galactic bar. They can be mainly categorized as those based on photometry, based on motions of gases and stars, and here we briefly review them to summarize what has been done in the research of the Galactic bar.

Photometric structure: The Galactic bar is strong supported by direct evidences of a large scale stellar asymmetry in the central a few kpc of the Milky Way. For instance, discrete source counts of AGB sources were performed by Weinberg (1992a), and IRAS sources were performed by Nakada et al. (1991), Weinberg (1992b) and Nikolaev & Weinberg (1997). In these studies, the size and shape of density contour suggested a bar semi-major axis of $\approx$3 kpc and position angle of $18^\circ \pm 2^\circ$ at the outer edge of the bar. Whitelock (1992) conducted the source counts of Miras, and estimated the tilt angle of the bulge-bar at roughly 45°. Blitz (1993a) showed the elongate distribution of the globular clusters within a 4 kpc centered on the Galactic Center with a tilt angle of $25^\circ \pm 8^\circ$. Hammersley et al. (2000) first claimed a "long

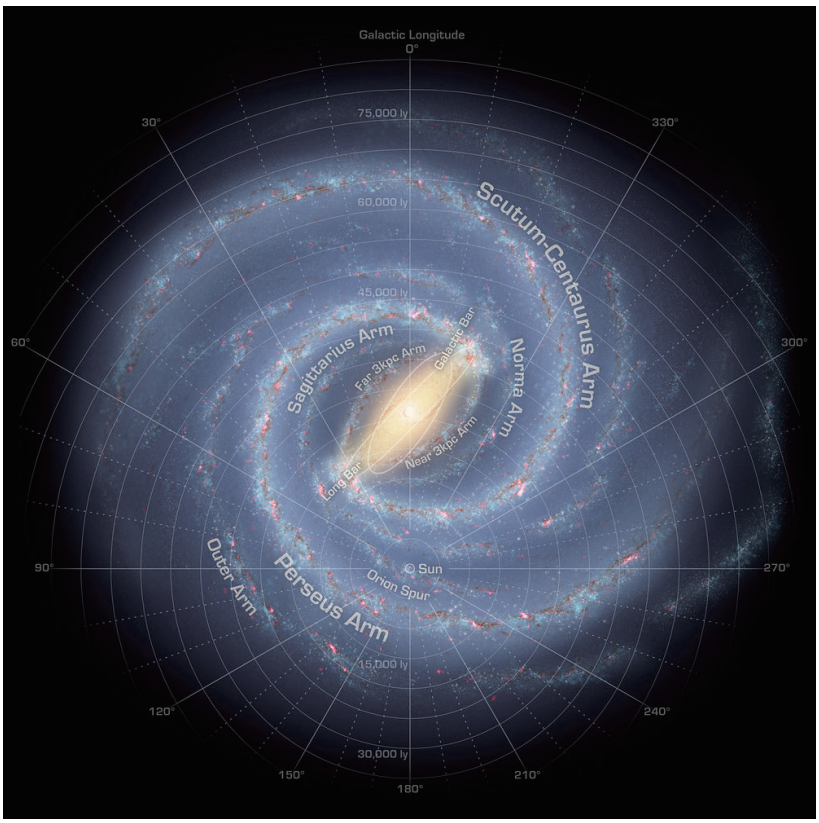

Figure 1.1: An artist's conception of Milky Way (R. Hurt: NASA/JPL-Caltech/SSC) viewed from the north Galactic pole from which the Galaxy rotates clock wise.

bar" based-on star counts and color-magnitude map of K giant stars, suggesting a bar with half-length of around 4 kpc and a position angle of about $43^\circ \pm 7^\circ$. The non-axisymmetry in the number of OH/IR stars along the line-of-sight as a function of galactic longitude was investigated by Sevenster (1996). Deguchi et al. (2002) estimated a tilt angle of $22^\circ \pm 8^\circ$ with near-infrared color-magnitude map of IRAS/SiO sources. The large microlensing optical depths towards the bulge were investigated with the OGLE/MACHO data (Paczynski et al. (1994); Zhao & Mao (1996); Zhao et al. (1996); Bissantz et al. (1997); Gyuk (1999)).

The COBE/DIRBE near-infrared surface photometry also supported the total image for the distribution of old stars in the inner Galaxy. The near side of the bar is in the first Galactic quadrant and the bulge-bar is tilted with respect to the Galactic plane (Blitz & Spergel (1991b)). The scale height of bulge minor axis is found to be $2^\circ.2 \pm 0^\circ.2$ (Weiland et al. (1994)). The tilt angle of the bulge-bar was estimated by Dwek et al. (1995) at $20^\circ \pm 10^\circ$ between its major axis and the line of sight to the Galactic center, with typical axis ratios of $x_0 : y_0 : z_0 = 1 : 0.33 \pm 0.11 : 0.23 \pm 0.08$. Fux (1997) also estimated the inclination angle of the Galactic bar relative to the Sun-Galactic center line is $28^\circ \pm 7^\circ$. Binney et al. (1997) also estimated the axis ratios with non-parametrical light distribution as $x_0 : y_0 : z_0 = 1 : 0.6 : 0.4$ with semi-major axis length$\sim$2 kpc. In their models, based on identification of the Lagrange point L_4 and the length of the bulge-bar, they inferred a pattern speed $\Omega_b \simeq$ 60-70 km s^{-1} kpc^{-1} for the bar.

Recently, the GLIMPSE survey data also revealed the bar structure of the Milky Way Galaxy (e.g. Churchwell et al. (2009); Benjamin et al. (2005)). For instance, Benjamin et al. (2005) showed a linear bar with half-length $R_{\rm bar} = 4.4 \pm 0.5$ kpc, tilted by $44^\circ \pm 10^\circ$ to the Sun-Galactic center line.

The linear distributions of red-clump stars were also discovered within a few kpc from the Galactic center along the Galactic plane, which strongly suggested the existence of bar structure (Stanek et al. (1997); Babusiaux & Gilmore (2005); Nishiyama et al. (2005); Rattenbury et al. (2007a); Rattenbury et al. (2007b)). With OGLE data, Stanek et al. (1997) suggested a bar model which has the major axis inclined to

the line of sight from 20°-30°, with axial ratio corresponding to $x_0 : y_0 : z_0 = 7 : 3 : 2$. With OGLE-II data, Rattenbury et al. (2007a) found the bar major-axis is oriented at an angle of 24°-27° to the Sun-Galactic Center line-of-sight, with the axis ratio $x_0 : y_0 : z_0 = 10 : 3.5 : 2.6$. Babusiaux & Gilmore (2005) also estimated the angle of $22 \pm 5°.5$ and the bar length of 5.0-6 kpc. Nishiyama et al. (2005) found that a magnitude peak changes continuously along the Galactic plane in the color-magnitude diagrams of red clump stars, and claimed an additional inner structure at $|l| \lesssim 4°$ with the bar length of ≈2 kpc. Cabrera-Lavers et al. (2007) showed that there are two very different large-scale triaxial structures coexist in the inner Galaxy with the samples of ranges $-5° < l < 30°$ and $|b| < 10°$. One is a long thin stellar bar constrained to the Galactic pane ($|b| < 2°$) with a position angle of $43.0° \pm 1.8°$, and other is a distinct triaxial bulge that extends to at least $|b| \leq 7.5°$ with a position angle of $12.6° \pm 3.2°$. On the other hand, McWilliam & Zoccali (2010) found two red clump populations co-existing in the same fields toward the Galactic bulge at higher latitudes $|b| > 5.5°$, instead of a body of a bar. They estimated a tilt angle of a line connecting the maxima of the foreground and background populations to the line of sight at $\sim 20° \pm 4°$. The photometric observations have all suggested the existence of the Galactic bar, and the length of the bar is approximately 2-6 kpc, and the tilt angle is approximately 10°-50°.

Kinematic structure from line-of-sight velocity of gasses: There have been many studies dealing with the l-v diagrams of H I (e.g., Hartman & Burton (1997); Kerr et al. (1986); Burton & Listz (1983); Rodriguez-Fernandez & Combes (2008); McClure-Griffiths et al. (2005)), CO (e.g., Dame et al. (2001); Clemens (1985)) and CS (e.g., Bally et al. (1988)). By several gas flow models or simple assumption (flat rotation or rotation curve), the produced l-v diagrams may be qualitatively understood, such as the bar, the 3 kpc arm, the non-circular velocities around the end of the bar, x_1/x_2-orbits, the molecular ring and the spiral arm tangent locations (e.g., Englmaier & Gerhard (2006); Englmaier & Gerhard (1999); Bissanz et al. (2003); Nakanishi et al. (2003); Fux (1999); Weiner & Sellwood (1999); Wada et al. (1994); Blitz & Spergel (1991b); Blitz et al. (1993b); Binney et al. (1991); Liszt & Burton

(1978); Manabe & Miyamoto (1975); Simonson & Mader (1973)), although above previous models did not provides a satisfactory account quantitative of the entire observed l-v diagrams. Recently, Baba et al. (2010) modeled the gas dynamics of barred galaxies using a 3-D, high-resolution, N body+hydrodynamical simulation, and reproduced both the large-scale structure and the clumpy morphology observed in the Galactic H I and CO l-v diagrams with the parameters of $\Omega_{\rm b} \sim 27$ km s^{-1} kpc^{-1}, $R_{\rm ILR} \approx 1$ kpc, $v_0 = 163$ km s^{-1}, $R_{\rm CR} \approx 5$ kpc, $R_{\rm OLR} \approx 10$ kpc, and inclination angle of the long axis of the bar 25°. They also showed transience of the various galactic structures.

The diagonal structure called Galactic Molecular Ring (GMR) is one of the most prominent structures in the l-v diagram. The orbit of the GMR in l-v diagram could be explained by circular motion. If the GMR was a real ring, it could be associated with a resonance. Binney et al. (1991) proposed that the GMR is probably associated with the Outer Lindblad Resonance. On the other hand, Combes (1996) suggested that the GMR could be better explained by the Ultra Harmonic Resonance, just inside the corotaion. However, the real spatial distribution of the GMR is not known and it could be composed of imbricated spiral arms instead of being an actual ring. Englmaier & Gerhard (1999) identified the GMR as one of the bars emanating from the ends of the bar. Nakanishi & Sofue (2006) found that the GMR seems to be the inner part of the two spiral arms (the Scutum-Crux arm and the Sagittarius-Carina arm), which are also reproduced by Rodriguez-Fernandez & Combes (2008) and Baba et al. (2010) based on simulation of the gas dynamics.

Frequently, the pattern speed and inclination angle of the bar have been estimated from comparing the gas flow in hydrodynamic simulations with the observed Galactic H I and CO l-v diagrams. These simulations generally reproduced a number of characteristic features in the l-v plot very well, but none of them reproduced all the observed features, like multiple complicated arms and/or small expansion structures. Thus the derived pattern speeds vary somewhat depending on studies. (Following values are based on standard values of $R_0 = 8$ kpc and $v_0 = 220$ km s^{-1}.) Binney et al. (1991) obtained $R_{\rm CR} = 2.4 \pm 0.5$ kpc and a bar angle of $16° \pm 2°$ from its

major axis from H I and CO l-v diagrams with the region $l \leq 12°$. Blitz & Spergel (1991a) obtained a position angle of the long axis of $45° \pm 20°$ from H I l-v diagrams. Wada et al. (1994) obtained $\Omega_{\rm b} = 20 \pm 5$ km s^{-1} kpc^{-1} and a bar angle of less than 20°. Combes (1996) obtained $\Omega_{\rm b}$ = 40-50 km s^{-1} kpc^{-1} ($R_{\rm CR}$ = 4-5 kpc) and the bar length $\sim$ 4-5 kpc in radius. Weiner & Sellwood (1999) obtained $\Omega_{\rm b} \approx 42$ km s^{-1} kpc^{-1} ($R_{\rm CR}$ = 5.0 kpc) and the inclination angle of 34° with a semi-major axis of the bar of 3.6 kpc from matching the terminal velocity of H I l-v diagrams. Englmaier & Gerhard (1999) obtained $\Omega_{\rm b} \simeq$60km s^{-1} kpc^{-1} ($R_{\rm CR} \simeq 3.5 \pm 0.5$ kpc) and inclination angle of $\approx$ 20°-25° by placing the corotation radius R_{CR} outside the 3 kpc arm and inside the molecular ring, and by matching mainly to the spiral arm tangents. Fux (1999) obtained $\Omega_{\rm b} \sim 50$ km s^{-1} kpc^{-1} ($R_{\rm CR}$ = 4.0-4.5 kpc) and an inclination angle of $25° \pm 4°$ from a comparison to several reference features in the CO l-v diagrams with a COBE-like bar. Bissanz et al. (2003) obtained $\Omega_{\rm b} = 60 \pm 5$ km s^{-1} kpc^{-1}, corresponding to corotation at 3.4±0.3 kpc with $20° \lesssim \phi_{\rm bar} \lesssim 25°$ from comparing with the ^{12}CO l-v diagrams. Rodriguez-Fernandez & Combes (2008) obtained $\Omega_{\rm b}$ = 30-40 km s^{-1} kpc^{-1} ($R_{\rm CR}$ = 5-7 kpc) and a bar tilt angle of 20°-35° with respect to the Sun-Galactic Center line. The previous studies about the kinematic structure derived from the l-v diagrams of gasses also indicated a existence of the Galactic bar, and the pattern speed of the bar is approximately 40-60 km s^{-1} kpc^{-1}, the inclination angle of the bar is approximately 10°-30°, and the half length of the bar is approximately 2-5 kpc.

Kinematic structure from radial velocities of stars: Most recent study of the streaming motions of the AGB stars in the Milky Way Galaxy was that by Deguchi et al. (2010) at the Galactic longitude between 20° and 40° based on the systemic velocities of the SiO masers and the distances derived from the magnitudes of K-band. They showed that deviant motions of $>$ 100 km s^{-1} of maser stars are created by periodic gravitational perturbations of the bar, and that the effect appears most strongly at radii between the corotation and the Outer Lindblad Resonance.

Since Nakada et al. (1993), large SiO/H_2O maser surveys for bulge IRAS sources observed with Nobeyama 45 m telescope were conducted. Izumiura et al. estimated

tilt angles (ϕ) and rotation rates of the Galactic bulge from l-v diagrams of SiO maser samples in several regions of $|l| \leq 15^\circ$ and $3^\circ \leq |b| \leq 15^\circ$, $-15^\circ < l < 15^\circ$ and $7^\circ < |b| < 8^\circ$, $|l| < 15^\circ$ and $4^\circ < |b| < 5^\circ$, $|l| < 15^\circ$ and $3^\circ < |b| < 15^\circ$ (exclude $4^\circ < |b| < 5^\circ$ and $7^\circ < |b| < 8^\circ$), which are 9.3±1.4 km s^{-1} (l deg^{-1}) (corresponding to the bulge rotation velocity (V_{rot}) of 66.4±10.0 km s^{-1} kpc^{-1} assuming $R_0 = 8$ kpc, Izumiura et al. (1993)), $\phi \approx 18^{+18}_{-14}$ deg and 10.4 ± 2.6 km s^{-1} (l deg^{-1}) (corresponding to V_{rot} = 74.3 km s^{-1} kpc^{-1}, Izumiura et al. (1994)), $\phi = 8^{+27}_{-31}$ deg and 10.8 ± 2.7 km s^{-1} (l deg^{-1}) (corresponding to V_{rot} = 77.1 km s^{-1} kpc^{-1}, Izumiura et al. (1995a)), $\phi = 6.9^{+31.5}_{-6.7}$ deg and 10.8 ± 1.2 km s^{-1} (l deg^{-1}) (corresponding to V_{rot} = 77.1 km s^{-1} kpc^{-1}, Izumiura et al. (1995b)), respectively. They have also surveyed SiO maser sources of the galactic central region. Fujii et al. (2006) suggested that l-v diagrams of the galactocentric SiO maser sources explained by x_1/x_2 orbital motions with distance modulus of K-band. For the SiO maser surveys in the galactic disk, Deguchi et al. (2000a) and Deguchi et al. (2000b) also estimated similar rotation rate of 10.7±1.4 km s^{-1} (l deg^{-1}), corresponding to V_{rot}=76.4 km s^{-1} kpc^{-1} assuming $R_0 = 8.0$ kpc and a tilt angle of 19^{+31}_{-20} deg of the bulge.

For the OH maser sources, with Tremeine & Weinberg method, Debattista et al. (2002) estimated a pattern speed of the non-axisymmtertric feature as $59 \pm 5 \pm 10\,(sys)$ km s^{-1} kpc^{-1} assuming $R_0 = 8$ kpc and $v_0 = 220$ km s^{-1}, and the corotation radius is $3.7 \pm 0.3^{+0.8}_{-0.5}$ kpc. Habing et al. (2006) discussed about the distribution of OH/IR and SiO-maser stars in the l-v diagrams with CO and model orbits in a galactic potential. They found a strong effect of the corotation resonance at r =3.3 kpc, a small effect of the outer lindblad resonance at 5 kpc and no effect of the inner lindblad resonance at 0.8 kpc. The stellar orbits are almost circular at $r \gtrsim 3.5$ kpc and the orbits become more and more elongated toward the Galactic Center in their model. The stellar kinematics of the Galactic bulge obtained with optical spectroscopy were also estimated, for instance, giants (e.g., Minniti (1996)), planetary nebulae (e.g., Beaulieu et al. (2000)) and so on.

Kinematic structure from proper motions of stars: Stellar proper motions in the Galactic bar region have been observed in some cases, for instance, in Baade's

window (e.g., Kozłowski et al. (2006) with HST; Spaenhauer et al. (1992)), Plaut's window (e.g., Vieira et al. (2007); Mendez et al. (1996)), Sgr I (Kuijken & Rich (2002) with HST), NGC 6558 (Soto et al. (2007)). Kuijken & Rich (2002) concluded that the bulge population is rotating from observed proper-motion anisotropy in bulge fields, and the bulge is dominated by old stars. Dehnen (1999) and Dehnen (2000) argued the bimodal (OLR and LSR modes) distributions of stellar velocities of late-type star in the solar neighborhood, as observed by HST, and estimated the pattern speed of the bar as 53 ± 3 km s^{-1} kpc^{-1} with an assumption of $\Omega_0 \approx 28.5$ km s^{-1} kpc^{-1}. In their studies, they also suggested that the Sun is situated slightly outside the radius $R_{\rm OLR}$ and bar angles between about 10° and 70°. Soto et al. (2007) reported the progress in their measurement of the 3-D kinematics of the stars of the Galactic Bulge obtained with HST (proper-motions) and VLT (radial velocities) data. They showed that a significant vertex deviation close to the galactic minor axis field, and suggested the signature of triaxial structure of the stellar bar in the galactic bulge.

As above description, there are many studies and approaches for the bar structure of the Milky Way Galaxy, and it is widely accepted that the Galaxy has a bar in its central region. However, there are no studies of "3-D" kinematics of gases around the bar by simultaneously obtaining accurate proper-motions and systemic velocities of gases. For the stellar 3-D motions, there is only one case of Soto et al. (2007) which is still preliminary result. Others, Sjouwerman et al. (2003) only proposed a study of the Galactic central region around few degrees with stellar 3-D motions of SiO maser. However, the high-accurate VLBI astrometry is able to provide 3-D motions of gasses around the Galactic bar, and this is a new approach to the bar studies.

1.2 VLBI Astrometry

Since Kurayama et al. (2005), VLBI (Very Long Baseline Interferometry) astrometric measurements have been providing highly-accurate annual parallax and absolute proper motions of individual maser sources toward star forming regions and AGB stars with typical error of ≈ 10 - 50 μas (microarcsecond) for parallaxes and $\approx$ a few

10 - 100 μas yr^{-1} for proper motions, respectively. In these measurements, the position reference sources of distant QSOs are supposed as fixed coordinates. As an example, Honma et al. (2007) showed the flatness of the outer rotation curve of the Galaxy with S269 which is located at 13.1 kpc away from the Galactic center.

The highly-accuate measurements have been extensively conducted by three VLBI arrays in the world. The american VLBI array called the VLBA (Very Long Baseline Array) have ten telescopes with 25 m dish, and maximum baseline length is more than 8,000 km between Mauna Kea on the Big Island of Hawaii and St. Croix in the U.S. Virgin Islands. In Europe, the EVN (European VLBI Network) is being operated. The EVN have 20 telescopes include 305 m telescope of Arecibo in the U.S and the most sensitive VLBI array in the world. On the other hand, the only array dedicated to astrometry is the VERA (VLBI Exploration of Radio Astrometry) in Japan (figure 1.2). The VERA have four telescopes with 20 m dish, and the maximum baseline length is about 2,270 km (see table 1.1). The VERA telescopes are marked by having dual-beam system, which effectively correct for atmospheric fluctuations. The VERA is also used as part of the JVN (Japanese VLBI Network, figure 1.3) as its expansion. The JVN have large telescopes (Yamaguchi 32 m, Usuda 64 m) and shorter baselines below $\sim$1,000 km (see table 1.1).

The VERA telescopes have 6.7/22/43 GHz receivers to observe maser sources (figure 1.4-(b-e)). Especially, the 6.7 GHz receivers are newly installed in the VERA antennas in May 2009 (figure 1.4-(a)). The 6.7 GHz receivers in the VERA are used at room temperature and system temperature is about 110 K. As the first results of 6.7 GHz observation with the JVN including the VERA, Sugiyama et al. (2008a) presented VLBI image of 13 methanol sources at 6.7 GHz with the JVN (W3(OH), Mon R2, W 33A, IRAS 18151$-$1208, G 24.78+0.08, G 29.95$-$0.02, IRAS 18556+0136, W 48, OH 43.8$-$0.1, ON 1, Cep A and NGC 7538), and they demonstrated the possibility of VLBI observation of 6.7GHz methanol maser with long baseline of $\sim$50 Mλ. The EVN also observe the 6.7 GHz methanol maser sources (e.g., Rygl et al. (2010)). However, their observation schedules are limited only three sessions per one year. The VLBA currently do not have 6.7 GHz receiver, and they will install it as described

Table 1.1: Baseline length of the VERA and the Japanese VLBI Network at 6.7 GHz observation.

Array	Baseline* [m]	Baseline† [Mλ]
Iriki-Yamaguchi (RY)	292,955	6.516428
Usuda-Yamaguchi (UY)	655,019	14.57010
Usuda-Iriki (UR)	878,168	19.53378
Iriki-Ishigaki (RS)	1,018,524	27.82780
Ogasawara-Usuda (OU)	1,065,666	23.70444
Iriki-Ogasawara (RO)	1,251,037	27.82780
Mizusawa-Iriki (MR)	1,266,754	28.17740
Ogasawara-Yamaguchi (OY)	1,287,848	28.64661
Ishigaki-Yamaguchi (SY)	1,298,939	28.89332
Mizusawa-Ogasawara (MO)	1,336,885	29.73738
Ogasawara-Ishigaki (OS)	1,826,711	40.63296
Usuda-Ishigaki (US)	1,874,175	41.68874
Mizusawa-Ishigaki (MS)	2,270,416	50.50264

$*$: Baseline length on the earth.

†: $f = 6.668518$ GHz or $\lambda = 4.495638 \times 10^2$ m

The JVN web page (http://www.astro.sci.yamaguchi-u.ac.jp/ kenta/jvnhp/)

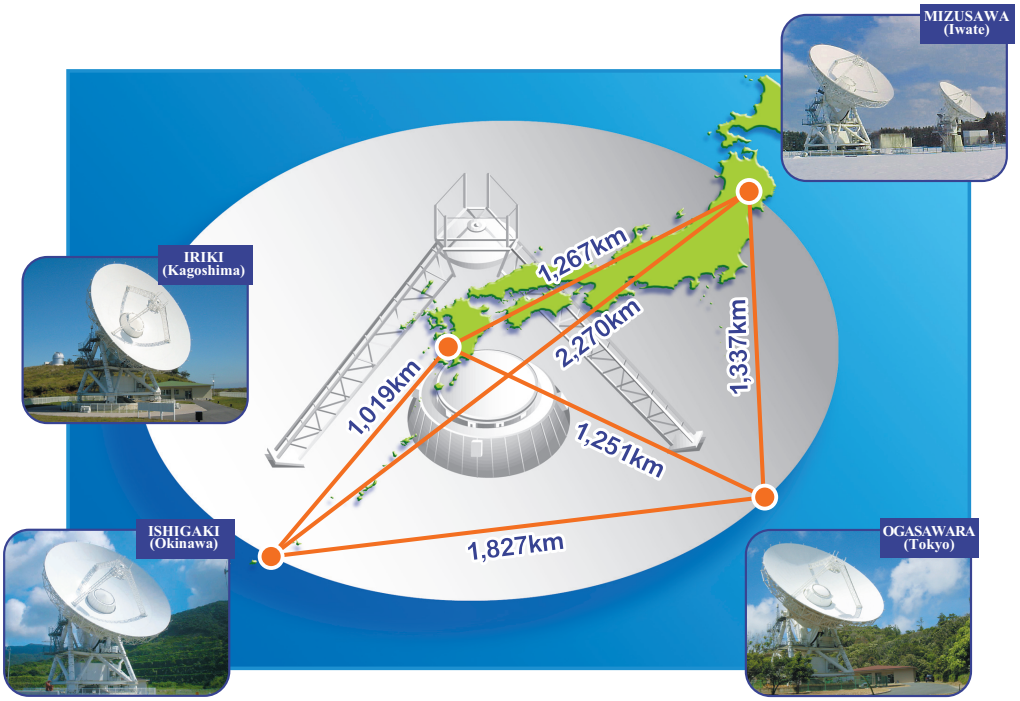

Figure 1.2: The VERA array

in the astro2010 science white paper (Reid et al. (2009c)). On the other hand, the VERA can operate monthly observations at 6.7 GHz. Thus the VERA would play a big role in the VLBI astrometry with 6.7 GHz methanol maser now.

In the previous studies, 22 GHz H_2O maser sources are dominant targets in VLBI astrometry. H_2O masers are emitted from high/low mass star forming regions and circumstellar envelopes of AGB stars. There are many strong H_2O maser sources and listed in Arcetri H_2O Maser catalog (Comoretto et al. (1990); Brand et al. (1994); Valdettaro et al. (2001)). Currently, parallaxes and absolute proper motions of about 30 H_2O maser sources have been already obtained (e.g., Hirota et al. (2008); Nakagawa et al. (2008); Reid et al. (2009b); Sato et al. (2010)).

43 GHz SiO maser sources are also observed for VLBI astrometry. SiO masers are mostly emitted from circumstellar envelopes of AGB stars and from a few star forming regions (Orion, W51, Sgr B2). Many SiO maser sources were discovered in previous surveys (c.f. Deguchi et al. (2010); Feast & Whitelock (2000)). SiO maser also provided high accuracy measurements of trigonometric parallaxes for a star forming

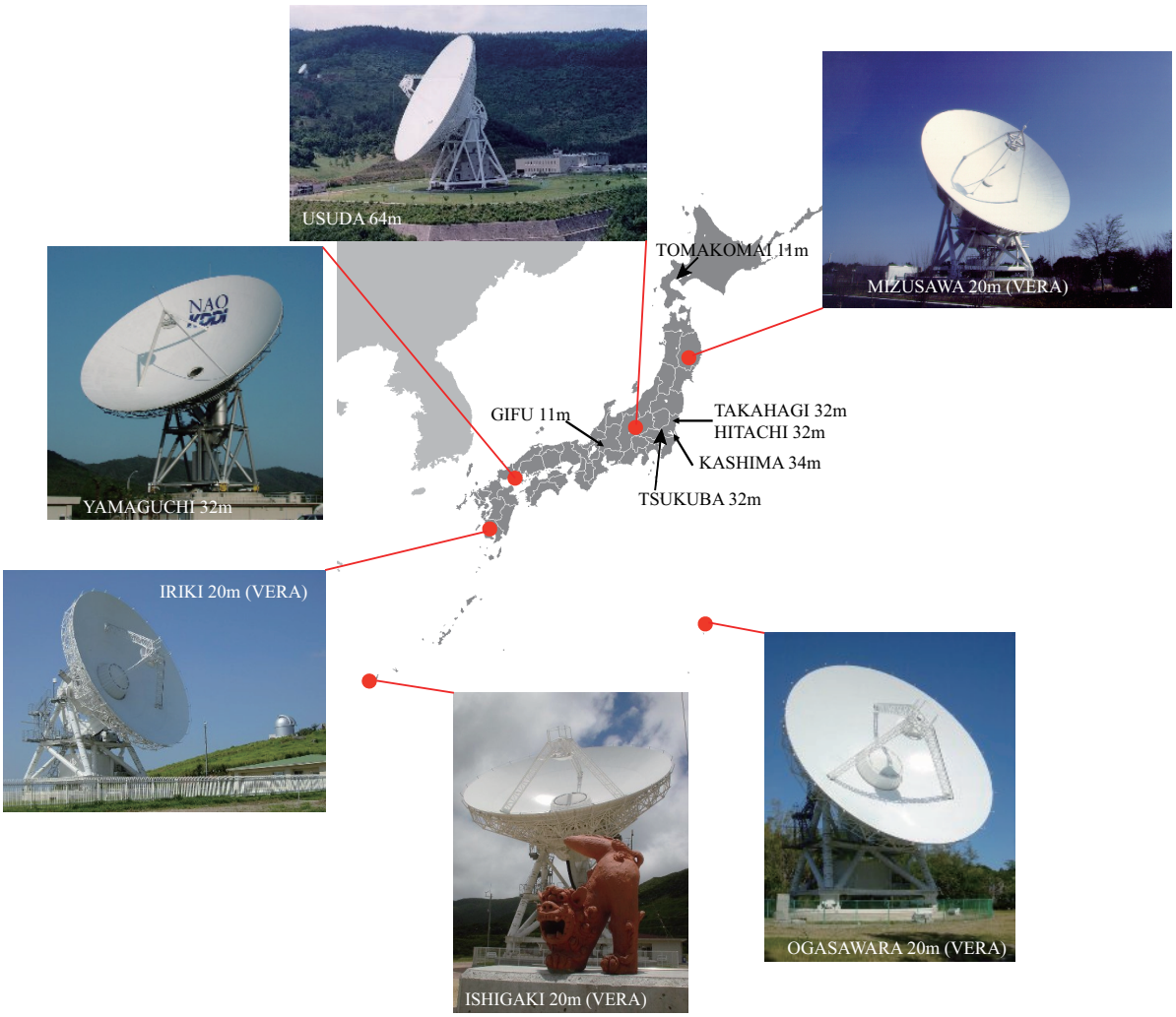

Figure 1.3: Arrays of the Japanese VLBI Network. The pictures show the telescopes having 6.7 GHz receiver.

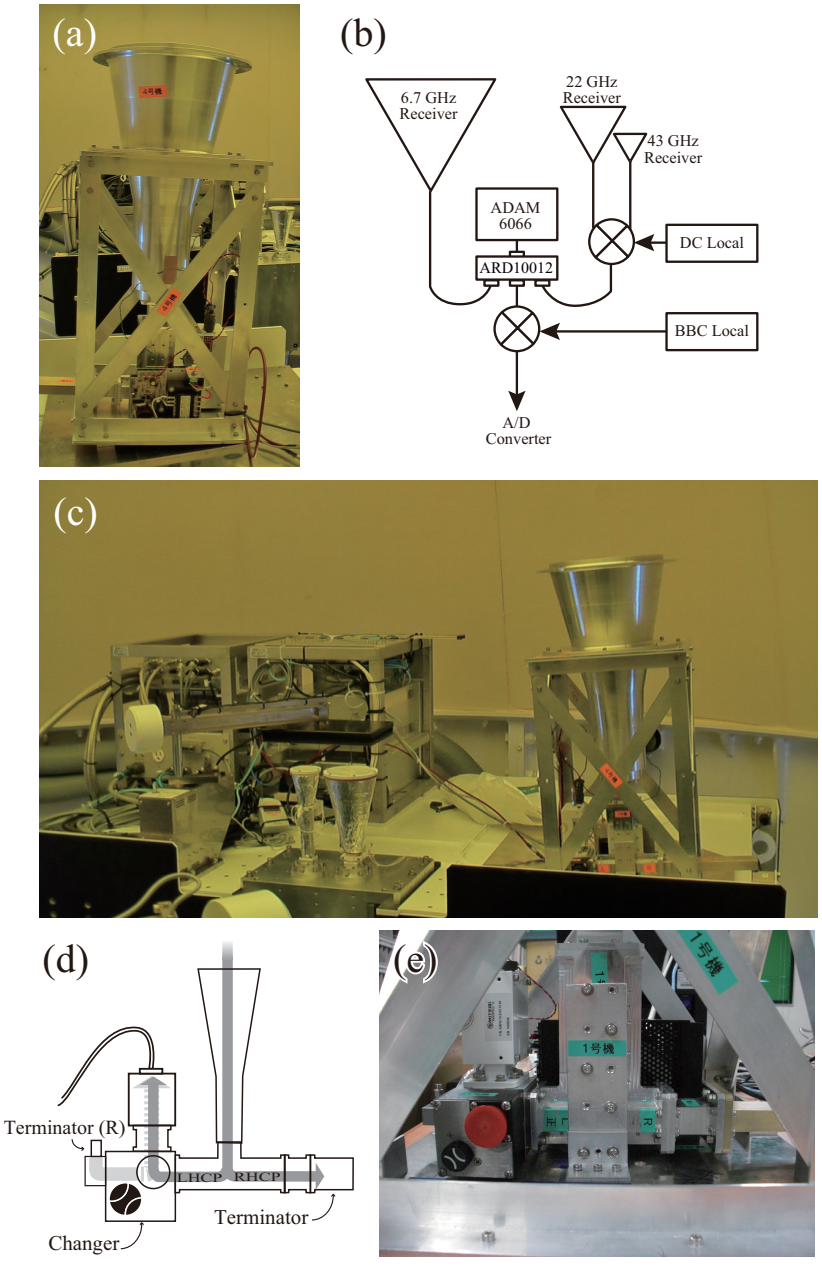

Figure 1.4: Pictures of the VERA receivers.

region (Orion KL by Kim et al. (2008)) and a AGB stars (R Aqr by Kamohara et al. (2010)). The lifetime of SiO masers toward evolved stars are generally several months or less than one year (e.g., Diamond & Kemball (2003); Matsumoto et al. (2008)), which is shorter than H_2O masers. There have been only two studies about parallax measurements of SiO maser sources now.

Recently, 6.7/12 GHz methanol maser sources are receiving more attentions as new targets of VLBI observations (e.g., Sugiyama et al. (2008a); Sugiyama et al. (2008b); Goedhart et al. (2005)). 6.7/12 GHz maser lines of methanol are categorized in Class II (Menten et al. (1991a); Menten et al. (1991b)), and compact to be observed with VLBI (Menten et al. (1992)). These methanol maser sources are currently considered to be emitted only from massive star forming regions (Xu et al. (2008)). The number of detected sources is above 1,000, and still increasing by various surveys (e.g., Caswell (2009); Pandian et al. (2007); Pestalozzi et al. (2005); Pestalozzi et al. (2007); Szymczak et al. (2002)). Astrometric observations with the methanol masers has just been started recently (Sanna et al. (2009); Rygl et al. (2010)).

Reid et al. (2009a) combined results obtained by VLBI astrometries, and provided accurate galactic parameters, demonstrating that the VLBI astrometry is a powerful tool to explore the structure of the Milky Way Galaxy. They estimated the distance of the Galactic center $R_0 = 8.4 \pm 0.6$ kpc and a circular rotation speed $\Theta_0 = 254 \pm 16$ km s^{-1}. On the other hand, the current IAU values for the LSR motion are $R_0 = 8.5$ kpc and $\Theta_0 = 220$ km s^{-1}. Further more, combining positions, distances, proper motions, and radial velocities, Reid et al. (2009a) yielded complete three-dimensional kinematic informations, and found that star-forming regions are orbiting the Galaxy about 15 km s^{-1} slower than expected rotation speed for circular orbits. This trend is theoretically supported by Baba et al. (2009), which represent the results of the high-resolution, self-consistent N-body+hydrodynamical simulation of the Milky Way Galaxy. They found that arms are not quasi-stationary but transient and recurrent, as suggested in alternative theories of spiral structures. Because of this transient nature of the spiral arms, star-forming regions exhibit a trend of large and complex non-circular motions, which is qualitatively consistent with the VLBI

observations.

Recent years, four sources around the Galactic bar were observed with 12 GHz methanol maser (Bartkiewicz et al. (2008); Brunthaler et al. (2009); Sanna et al. (2009)). The large peculiar motions are found in these sources. These peculiar motions are considered to be the results of gravitational perturbations from the Galactic bar. Baba et al. (2009) also showed larger peculiar motions around the bar structure than the motions around spiral arms. However, it is difficult to judge whether they are tracing the effect of the bar based on only four sources. Thus we need more sample sources to investigate the effect of the bar based on the 3-D motions of the sources. Around the bar, there are many 6.7 GHz methanol maser sources tracing massive star forming regions. In fact, the 6.7 GHz methanol maser sources are concentrated in the molecular ring on the longitude-velocity maps in Pestalozzi et al. (2007).

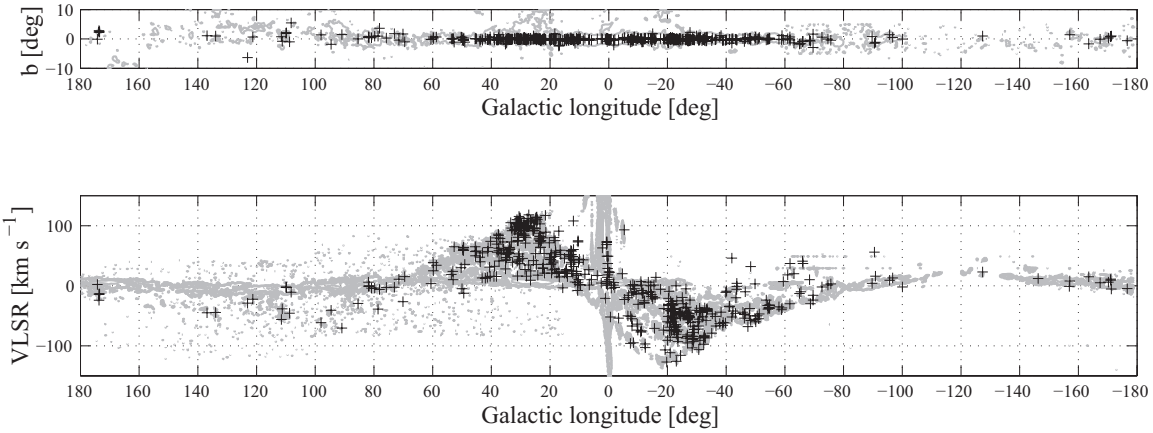

Figure 1.5: 6.7 GHz methanol maser sources and the CO contours from Dame et al. (1987) (Pestalozzi et al. (2007)).

The 6.7 GHz methanol maser sources are attractive sources in investigations of distant galactic structures. The 6.7 GHz methanol maser sources have second-strongest next to H_2O maser and stronger than 12 GHz methanol maser (Menten et al. (1991b)). In addition, in higher frequencies such as 12 to 43 GHz the phase-reference sources become weak because the QSOs as the phase-reference sources usually become fainter at higher frequency (e.g., 22/43 GHz). Also, the 6.7 GHz methanol maser sources

generally have stable space distributions with flux time variations (e.g., Goedhart et al. (2004)), and small internal proper motions compared to the Galactic rotations (the velocity widths typically less than 10 km s^{-1}, see Szymczak & Kus (2000)). Although lifetimes of H_2O and SiO maser are month or one year scale, that of the methanol maser is decade scale (e.g., Moscadelli et al. (2010)). Therefore, the methanol maser sources are suitable for astrometric observations, which track same maser spot for one year or more.

Thus, with VLBI observations of 6.7 GHz methanol maser sources, we will be able to trace 3-D gas motions (systemic velocities and proper motions) to investigate the Galactic structure around the bar.

1.3 Aim of This Thesis

The aim of this thesis is an investigation of peculiar motions affected by the galactic bar structure and kinematically establish of the bar structure based on the 3-D gas motions. For this purpose, the present thesis consists of three steps as below. First, in order to test the astrometric performance of the VERA/JVN at 6.7 GHz, we measured the annual parallax and absolute proper motions of the 6.7 GHz methanol maser sources for the test source, W3(OH) (section 2). Second, we conduct the fringe check observations to select observable sources which can be used to trace the effect of the bar (section 3). Finally, we measure the three dimensional velocities for the sources considered to exist around the galactic bar structure, and discuss the bar effect seen in the 3-D gas motions (section 4).

Chapter 2

6.7 GHz Methanol Maser Toward W3(OH) Ultracompact H II Region

2.1 Introduction

6.7 GHz methanol maser sources are potential targets for VLBI astrometry to trace the 3-D structure of the Galaxy. The 6.7 GHz methanol maser line is the brightest line among methanol maser emissions (Menten et al. (1991b)). Nearly 1,000 of 6.7 GHz methanol maser sources are already discovered in the Galactic plane (e.g., Green et al. (2009)). In addition, internal proper motions of the 6.7 GHz methanol masers are generally smaller than that of H_2O masers, and structures of maser spots are stable for a period required by astrometric monitorings (1 year or more). Recently Rygl et al. (2010) reported first parallax measurements of 6.7 GHz methanol maser sources with the European VLBI Network (EVN). They show that the 6.7 GHz methanol maser sources can be used for VLBI astrometry. In order to conduct the VLBI astrometry of 6.7 GHz methanol masers, we have installed C-band receivers to the VERA (VLBI Exploration of Radio Astrometry). Test observations have already started with the VERA or the Japanese VLBI Network (JVN) at 6.7 GHz

observation mode. The VERA is also included in the JVN Network. As one of the test observations, we conducted phase-referencing observations of W3(OH) to evaluate the astrometric capability of the JVN/VERA. W3(OH) is one of the brightest sources in the 6.7 GHz methanol maser sources, and have been extensively studied. Accurate distances toward W3(OH) have been already reported by Xu et al. (2006) and Hachisuka et al. (2006). Hence W3(OH) is one of the best targets to investigate the astrometric capability of the JVN/VERA array.

W3(OH) is a massive star forming region located in the Perseus arm at 1.95 ± 0.04 kpc far from the Sun (Xu et al. (2006)). W3(OH) is famous as an UC H II region associated with a far-infrared source. A total luminosity of the far-infrared source was estimated to be 10^5 $L_\odot$ (Campbell et al. (1989); Harper (1974)), which corresponds to a luminosity of a main-sequence star with spectral class O7 (Dreher & Welch (1981)). This exciting star is also detected by X-Ray observation with the Chandra (Feigelson & Townsley (2008)). And a coordinate is determined as $\alpha_{J2000.0}$=02h27m03.84s, $\delta_{J2000.0}$=+61d52'24".9 with a position error of 0.4". For the UC H II region itself, it is a limb-brightened shell with diameter about 10^3 AU measured at 15 GHz (Dreher & Welch (1981)). The expansion of the UC H II region was detected with typical speeds of 3 - 5 km s^{-1} by Kawamura & Masson (1998). In the western part of the UC H II region, various maser emissions were detected: 12 GHz methanol maser (Moscadelli et al. (1999), (2002), (2010); Xu et al. (2006)), 6.7 GHz methanol maser (Menten et al. (1992); Harvey-Smith & Cohen (2006); Etoka et al. (2005)), 1.6/1.7/4.7/6/13 GHz OH masers (Norris et al. (1982); Bloemhof et al. (1992); Wright et al. (2004a, b); Fish et al. (2006); Harvey-Smith & Cohen (2006); Desmurs et al. (1998); Fish & Sjouwerman (2007); Baudry et al. (1998)). In addition to maser emissions, thermal lines of OH emissions/absorptions (Baudry et al. (1993)) and NH_3 absorptions (Reid et al. (1987); Guilloteau et al. (1983)) were also detected in the western part of the UC H II region. In contrast to the western part, only few maser spots were found in the eastern part of the UC H II region (Fish & Sjouwerman (2007)). From these observations, several pictures were proposed by previous studies, for instance, a torus (Fish & Sjouwerman (2007); Dickel & Goss (1987); Guilloteau et al. (1983)), a disk

(Moscadelli et al. (2010); Wright et al. (2004b)), an expansion or a cometary bow-shock (Bloemhof et al. (1992)), an collapsing envelope (Reid et al. (1980)). To test these pictures, high resolution images and three-dimensional velocity structures are needed.

In this paper, we report two kinds of results about the 6.7 GHz methanol maser toward W3(OH) observed with JVN/VERA. The first results are about distributions and internal motions obtained with in-beam VLBI imaging and the second results are about phase-referencing astrometry.

2.2 Observations and Data Analysis

2.2.1 Observations

We observed a 6.7 GHz methanol maser emission toward W3(OH) ($\alpha_{J2000.0}$=02h27m 03.81920s, $\delta_{J2000.0}$=+61d52'25.2300", Xu et al. (2006)) from May 2008 to April 2010 with the JVN including the VERA. Table 2.1 summarizes these observations. For the phase-referencing, we conducted one-beam switching observations because all 6.7 GHz receiving systems are single-beam in the JVN as well as the VERA. W3(OH) and a phase-reference source of J0244+6228 were alternately observed with five-minute cycles (typically 2 and 1.8 min on-source integration times for the target maser and the reference source, and rest for slewing). The coordinate of J0244+6228 is $\alpha_{J2000.0}$=02h44m57.69667s, $\delta_{J2000.0}$ = +62d28'06.5155" from ICRF, which is 2.17° separating from W3(OH). 3C 84 was also observed once one hour as a calibrator. Radio frequency of 6.668518 GHz are adopted in this observations as the rest frequency of CH_3OH $5_1 \rightarrow 6_0A^+$ transition. Left-handed circular polarization was received except at Iriki and Ogasawara stations at epochs 1 and 2, in which linearly polarized receivers were used. The received signals were filtered in a 16 MHz bandwidth channel (epoch 1 - 3), or 16 channels with 16 MHz bandwidth each (epoch 4 - 6). The filtered signals were recorded with SONY DIR1000 recorder at a rate of 128 Mbit s^{-1} (epoch 1 - 3) or DIR2000 recorder at a rate of 1024 Mbit s^{-1} (epoch 4 - 6). The recorded signals were correlated with the Mitaka FX correlator (Chikada

Table 2.1: Summary of the JVN observations.

Epoch	Date YYYY/DOY	Duration [UT]	Telescope*	Synthesized beam†] (mas^2, deg)
1§	2008/131	22:00 - 29:00	M, R‡, S, O‡, Y, U	5.6×3.2, −33.5
2§	2008/301	13:00 - 18:00	M, R‡, S, O‡, Y, U	6.1×3.1, −38.4
3§	2009/143	23:05 - 31:00	M, R, S, O, Y	4.5×2.8, −58.0
4	2009/338	08:15 - 16:23	M, R, S, O	4.2×2.6, −24.0
5	2010/046	03:30 - 11:38	M, R, S, O	3.8×2.6, −35.2
6	2010/102	23:44 - 31:53	M, R, S, O	3.6×2.7, −35.1

∗: Telescope code. M: VERA telescope at Mizusawa station, R: Iriki (VERA), S: Ishigaki (VERA), O: Ogasawara (VERA), Y: Yamaguchi, U: Usuda.

†: Synthesized beam size and position angle.

‡: The received signal was linear polarization.

§: The resolution of each velocity channel in the visibility data is 3.91kHz in marked epochs, and 15.63 kHz in other epochs.

et al. (1991)). Since the maser line is narrow and since the phase-reference calibrator is bright enough, we selected a small portion of bandwidth (4 MHz for epoch 1 - 3 or 8 MHz for epoch 4 - 6) in the correlation process. The selected band was centered at the maser line to obtain high spectral resolution. This produced auto-correlation and cross-correlation spectra consisting of 1024 spectral channels with a frequency spacing of 3.91 kHz ($\sim$ 0.18 km s^{-1}) for epoch 1 - 3, or 512 spectral channels with a frequency spacing 15.63 kHz ($\sim$ 0.70 km s^{-1}) for epoch 4 - 6.

2.2.2 In-beam and Phase-referencing Mappings

In this paper, we produced two types of maser maps: one is in-beam map for researching internal maser proper motions with respect to a reference maser spot, and the other is phase-referencing map for measuring absolute positions with respect to

the position reference source.

In both mappings, data reductions were performed using the NRAO AIPS package basically in a standard manner. The delay and delay-rate offset were calibrated using 3C 84. Bandpass responses were also calibrated using 3C 84. Amplitude calibrations were performed by template method with the total-power spectra of W3(OH). For data of Iriki and Ogasawara stations in epochs 1 and 2, we also applied special calibrations to correct amplitudes for the polarization difference (linear/circular) by using the method described in Sugiyama et al. (2008b).

For the in-beam mapping, fringe-fitting was conducted for a reference maser spot of $v_{\rm LSR} = -45.4$ km s^{-1} in W3(OH), which is the brightest spot in a W3(OH) methanol maser. In self calibration of the reference maser spot, models of clean components were made by the DIFMAP software package provided by Caltech, to obtain faint components of the continuum emission from the reference maser spot. The solutions of self-calibration were applied to other velocity channels of maser.

For the phase-referencing mapping, instead of the reference maser spot, fringe solutions were estimated for J0244+6228 with solution intervals of one minute. In self calibration of J0244+6228, models of clean components were also made with the DIFMAP, to obtain faint components of the continuum emission from J0244+6228, if exists. However, the source had no distinct structure in any epoch, and peak flux of J0244+6228 was about 600 - 1,000 mJy beam^{-1}. The self-calibration solutions of J0244+6228 were applied to the data of W3(OH). Since the apriori delay model used in the correlator was not accurate enough for VLBI astrometry, we recalculated more precise delays and we corrected for the differences between them. The difference in optical path length was $\sim$ 2 mm or less between our recalculated model and the CALC9 model developed by the NASA/GSFC VLBI group. In this correction, the visibility phase errors caused by tropospheric delay were calibrated based on GPS measurements (Honma et al. (2008)). The ionospheric delay was also calibrated based on the data of the total vertical electron content produced by JPL.

Synthesis imaging and deconvolution were performed using the AIPS task IMAGR with uniform weighting. The results of synthesized beam size (FWHM) and position

angle are listed in table 2.1. Both kinds of maps were made with 4086 pix × 4086 pix, and a pixel size of 0.5 mas pix^{-1}). When we made the phase-referencing maps, for epochs 1 - 3, every four velocity channels were combined into one to make a velocity resolution equal through all the epochs. For in-beam maps, there was no need to combine channels as above because we used the data with the same velocity resolution in epochs 1 - 3. Finally, the maser positions were derived by gaussian fitting using the AIPS task JMFIT for the in-beam maps.

2.2.3 Derivation of Internal Proper Motions

To investigate maser distribution and internal proper motion, we used the in-beam maps of epochs 1 - 3. This is because epochs 4 - 6 did not include antennas with large apertures such as Yamaguchi 32 m and Usuda 64 m, and hence the number of detected spots were decreased drastically compared to epochs 1 - 3. All maser spots whose signal-to-noise ratios are larger than 10 were considered for maser identification to derive proper motions. We identified maser spots with the same velocity within a beam size (θ_{beam}) between epochs, because the proper motions of the methanol maser were expected to be small. In fact, most of the spots were identified within a separation of one mas. For maser spots identified at all three epochs, we conducted least-square fitting of the linear proper motion to position-time data sets. In the present study, minimum proper motions which we can detect are roughly estimated by $0.1\theta_{\rm beam} \,/\, \Delta t_{\rm obs}$, which are $\sim$ 0.58 mas yr^{-1} or $\sim$ 5.4 km s^{-1} using the distance of 1.95 kpc. $\Delta t_{\rm obs}$ is a maximum time-span between observations, which is 378 days between epochs 1 and 3. The value of 0.1 corresponds to the lowest signal-to-noise ration of 10 in our map. Signal-to-noise ratio ranged typically about 10 - 150.

2.2.4 Derivation of Annual Parallax and Absolute Proper Motion

Using spot positions in the phase-referenced maps, we obtained absolute proper motions of 6.7 GHz maser spots toward W3(OH) with respect to the extragalactic source

of J0244+6228. Finally, six maser spots were selected to derive an annual parallax and absolute proper motions on the following conditions. Each maser spot has the same systemic velocity, apparently similar structure and been living throughout all epochs. These six maser spots have signal-to-noise rations greater than 10. The absolute motion of each maser spot can be modeled by the sum of a linear proper motion and an annual parallax. In this astrometric analysis, we assumed that all maser spots have a same annual parallax, and we simultaneously determined the proper motions and the initial positions in right ascension and declination along with the common annual parallax by a least-squares analysis of the six maser spots. When the common annual parallax and the absolute proper motion of each spot were estimated, these six maser spots were assumed to have the same error bars which were determined so that the reduced χ^2 becomes unity. In error estimations of the values from the fitting, the degrees of freedom were recalculated after the fitting because spots in a same feature were supposed not to be independent. We adopted the most conservative approach of assuming 100% correlation and the errors of the parallax and proper motions of each spots are enlarged by a factor of 1.23 ($= \sqrt{47/31}$) compared to the error from the least-square fitting. This is because degree of freedom of independent six spots data is 47 [= 6 (spots) $\times$ 6 (epochs) $\times$ 2 (positions of RA and Dec) $-$ 25 (parameters of one π and each spots of RA position, Dec position, $\mu_l \cos b$, and μ_b)], in spite of a degree of freedom of independent four spots data is 31 [= 4 (spots) $\times$ 6 (epochs) $\times$ 2 (positions of RA and Dec) $-$ 17 (parameters of one π and each spots of RA position, Dec position, $\mu_l \cos b$, and μ_b)]. With the fitting results, averaged proper motions of the six spots were also estimated. A deviation of the proper motions was also estimated with a degree of freedom (ν) of 3 = [6 (spots) $-$ 2 (same feature) $-$ 1] in a equation of $\sigma = \sqrt{\{\sum_{i=1}^{6}(x_i - \bar{x})^2\}/\nu}$.

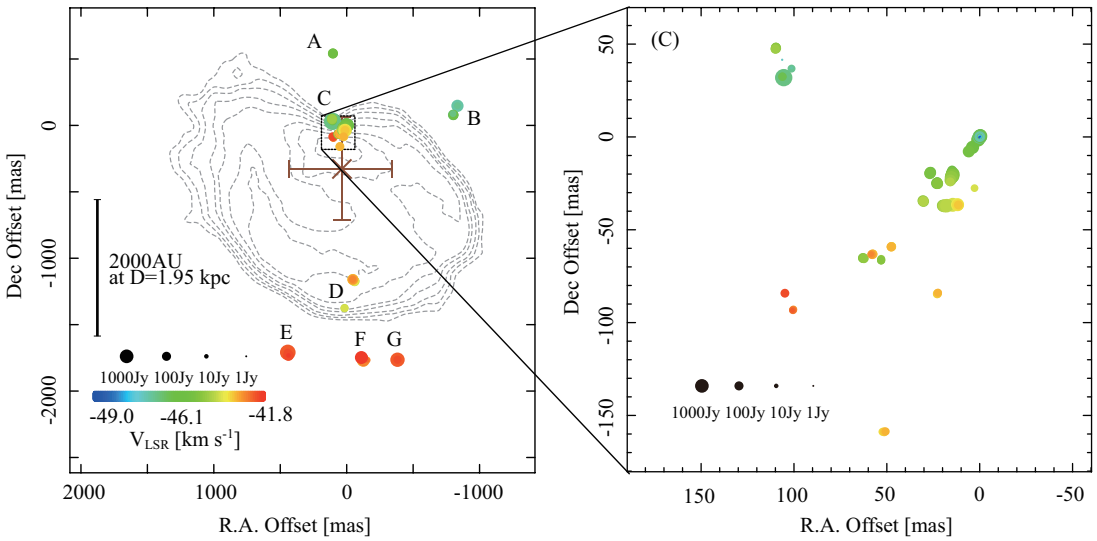

Figure 2.1: Left : The distribution of 6.7 GHz methanol maser spots. The sizes of the plotted circles are proportional to the integral flux intensity of the spots which was observed on DOY 301 in 2008 (epoch 2), on the logarithm scale. The errors in the positions of the features are smaller than the circle sizes. Color-codes represent the LSR velocity. The dashed line is a 15 GHz radio continuum map of the UC H II region (Bloemhof et al. (1992)). The position of the ionizing star is shown by brown cross with error bar (Feigelson & Townsley (2008)). The origin of this map is $\alpha_{J2000.0}$=02h27m03.818s, $\delta_{J2000.0}$=61d52'25.248". Right: Zoom-in view of the left panel around the map origin.

2.3 Results

2.3.1 Spatial Distribution and Internal Proper Motion

The number of spots detected in the in-beam map was 129 in epoch 1, 135 in epoch 2 and 149 in epoch 3. Figure 2.1 shows the spatial and velocity distribution of 6.7 GHz methanol maser spots with the integral flux intensity at epoch 2. The absolute position of the maser spot with $v_{\rm LSR} = -45.4$ km s^{-1} at (0, 0) coordinate in figure 2.1 (301 doy in 2008) is $\alpha_{J2000.0}$ =02h27m03.8178s $\pm$ 0.0080s, $\delta_{J2000.0}$ = +61d52'25.24824" $\pm$ 0.00049" which is obtained from the absolute astrometry with respect to J0244+6228 (see section 2.3.2). This error is dominated by the position accuracy of phase-reference source J0244+6228 in the ICRF catalog. In figure 2.1, 15 GHz radio continuum in Bloemhof et al. (1992) is superimposed by using methanol and OH maser coordinates in figure 6 in Bloemhof et al. (1992). The ionizing star position from Feigelson & Townsley (2008) is also plotted.

We found seven clusters denoted as clusters A - G in figure 2.1. The radial velocity of spots ranges from $v_{\rm LSR} = -41.5$ to -48.9 km s^{-1}. The red-shifted components are in the south part (clusters D - G), and the blue-shifted components are in the north part (clusters B, C). These seven clusters of maser spots extended over an area of about 1.3" $\times$ 2.3" area. This distribution indicates that 6.7 GHz methanol masers spread much wider than the UC H II region in the south-north direction. These methanol masers are mainly distributed in the western part of the UC H II region on the sky plane. Maser distribution of the 6.7 GHz methanol maser is similar to OH maser distribution, but 6.7 GHz methanol maser has a more patchy than the distribution of the 6035 MHz OH maser (see figure 1 of Fish & Sjouwerman (2007)).

The most complicated velocity/spatial distribution was seen in cluster C in figure 2.1. Only cluster C have a wide velocity range of about 6.7 km s^{-1} ($v_{\rm LSR}$ is from -42.2 to -48.9 km s^{-1}). On the other hand, the other maser clusters have narrower velocity range, being 1.2 km s^{-1} or less. These trends have basically been maintained for more than 16 years between our results and Menten et al. (1992). However, the velocity range of the cluster C is about 2.4 km s^{-1} wider than the results of Menten

et al. (1992), and there are some velocity shifts less than 1 km s^{-1} for the other clusters.

Figure 2.2 shows internal proper motions of 107 maser spots in the in-beam map. These motions are relative to the reference maser spot with $v_{\rm LSR} = -45.4$ km s^{-1}. We note that measured internal proper motions are fairly small. In fact, only 14 maser spots were detected their proper motions with 3σ or larger value in the least-square fitting. Nearly half (56 spots) have only 1σ detection. Therefore, most of proper motions of individual spots did not have high accuracies and hence, motions of each spot may not be reliable. In addition, variations of maser spots structures could also have an influence on the proper motion measurements of spots. Thus, to obtain more reliable motions, we averaged the maser proper motions with equal-weighting in each maser cluster with that of A to G, and derived relative motions of each maser cluster (A, B, D - F) to cluster C. These motions are also plotted in bottom-left panel of figure 2.2 with thick black vector. The global motions for South-North direction were larger than for East-West direction. Southern maser clusters E - G show motions toward the south, and moving away from cluster C.

In the bottom-left panel in figure 2.2, internal proper motions of 1665 MHz OH maser and 15 GHz radio continuum of Bloemhof et al. (1992) were superposed to our results. Note that the reference spot of $v_{\rm LSR} = -43.88$ km s^{-1} was used to derive internal proper motions in Bloemhof et al. (1992) while we used the reference spot of $v_{\rm LSR} = -45.4$ km s^{-1} for methanol masers. Therefore, there could be an unknown proper motion offsets between our results and Bloemhof et al. (1992). However, since these reference spots are in the same region of cluster C and the difference in systemic velocities is only 1.5 km s^{-1}, the proper motion offset is expected to be small. Actually, most of the derived internal proper motions are about 3 to 5 km s^{-1}, and proper motions of OH and methanol masers show a similar trend of expansions in figure 2.2, implying that the proper motion offset is fairly small. Detailed discussion on the proper motions of the maser spots are given in section 4.2

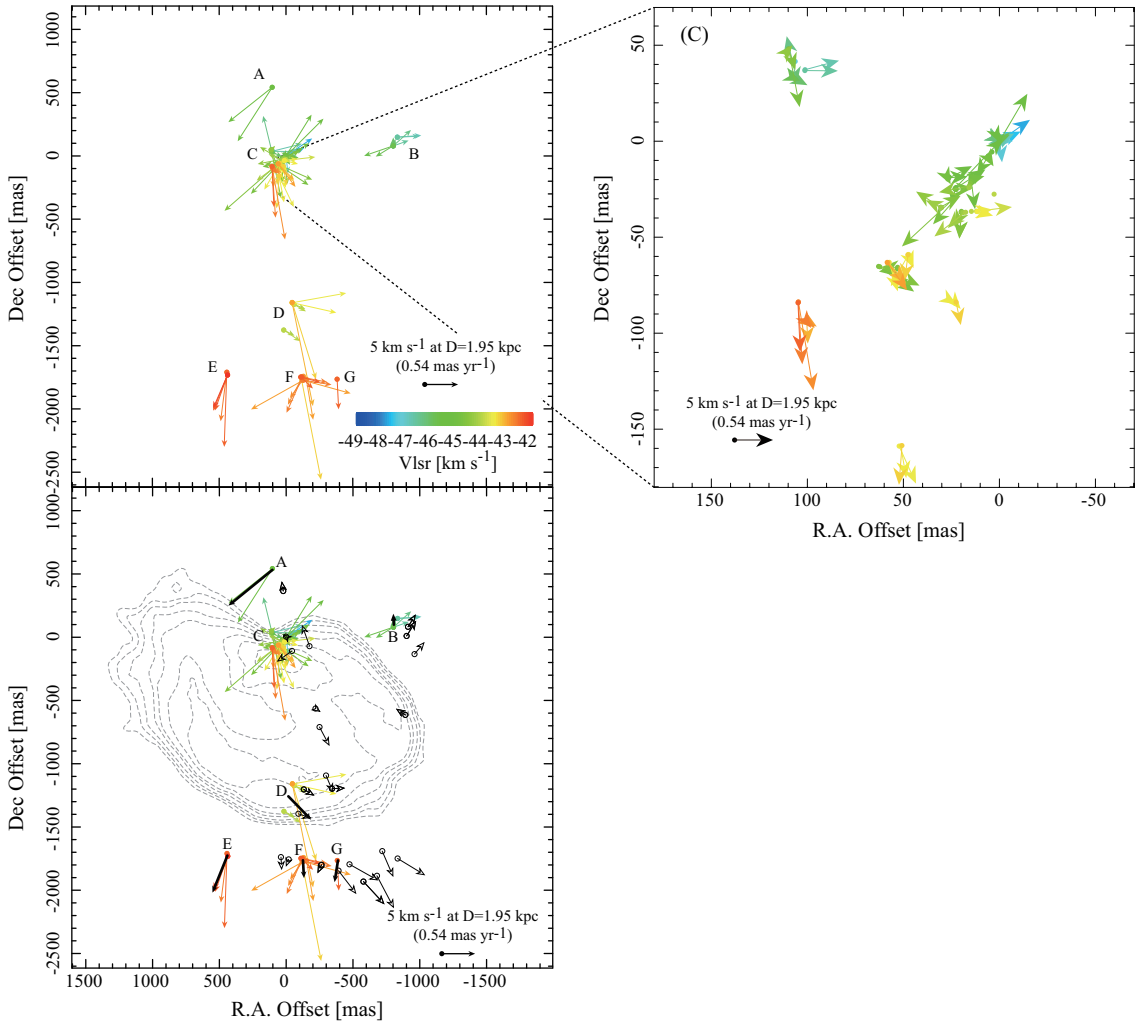

Figure 2.2: Left: The internal proper motion for 6.7 GHz methanol maser spots toward W3(OH). Color-codes represent the LSR velocity. The colored vectors show directions and amplitudes of relative proper motions on the sky plane to the reference spot with -45.4 km s^{-1} LSR velocity. The scale of vector is presented by a black colored thin vector. Right: Zoom-in view of top-left panel around origin. Bottom-left: The colored vectors are the same as the top-left one. The thick black vectors show averaged relative proper motion at each A - G cluster to the C cluster around the origin. The proper motion vectors of 1665 MHz OH maser and the contour map of 15 GHz radio continuum emission of the UC H II region taken from figure 7 of Bloemhof et al. (1992) are also shown as outlined black vectors and broken lines, respectively.

2.3.2 Parallax and Absolute Proper Motion

We detected the absolute proper motions of six maser spots in the cluster C based on the method described in section 2.2.4. These motions are presented in figure 2.3. The fitting results with the annual parallax and the absolute proper motions are also shown in figures 2.3 and 2.4, and listed in tables 2.2 and 2.3. The fitting yielded the annual parallax $\pi = 0.633 \pm 0.112$ (err: 18%) mas for 6.7 GHz methanol maser toward W3(OH). This parallax corresponds to a distance of $1.58^{+0.34}_{-0.24}$ kpc from the Sun. This result is almost consistent with the previous results (Xu et al. (2006); Hachisuka et al. (2006)), as will be discussed in detail in section 2.4. The fitting error of the absolute proper motion of each maser spot is 0.39 toward the east and 0.25 toward the north. The average proper motion also estimated as -1.10 ± 0.30 mas yr^{-1} toward the east and -0.16 ± 0.38 mas yr^{-1} toward the north. Each error in the average proper motion is standard deviation of the averaged proper motions of six maser spots in table 2.2.

The standard deviations of the post-fit residuals, which are determined so that reduced χ^2 becomes unity, was obtained as $\sigma_\alpha = 0.53$ mas and $\sigma_\delta = 0.33$ mas in right ascension and declination, respectively. These residuals are likely to represent the positional uncertainties in the present astrometric observations. These residuals are larger than the errors derived from the dynamic ranges of the phase-referencing maps for each maser spot, which can be estimated as $0.5\theta_{beam}$/SNR (Reid et al. (1988)), corresponding to 0.02 - 0.18 mas in our data. These residuals are most likely originate in atmospheric zenith delay residuals and/or structural variations of the maser spots (for examples of detailed discussions, see Honma et al. (2007) and Hirota et al. (2008)).

In our results, it is unusual that the residual value of right ascension is larger than the value of declination. This result could be attributed to a large position offsets in the third epoch (2009/143) as can be seen in figure 2.4. If we fit the data excluding the third epoch, the resultant distance value is consistent within the mutual error (17%; $\pi = 0.626 \pm 0.105$ mas, corresponding to D = $1.60^{+0.32}_{-0.23}$ kpc) and the residual become comparable between right ascension and declination ($\sigma_\alpha = 0.30$, $\sigma_\delta = 0.30$). Thus, the large residual in right ascension is probably affected by the outliers in the third epoch. However, to be conservative, we take the results including the 3rd epoch

as the final astrometric results in the present paper.

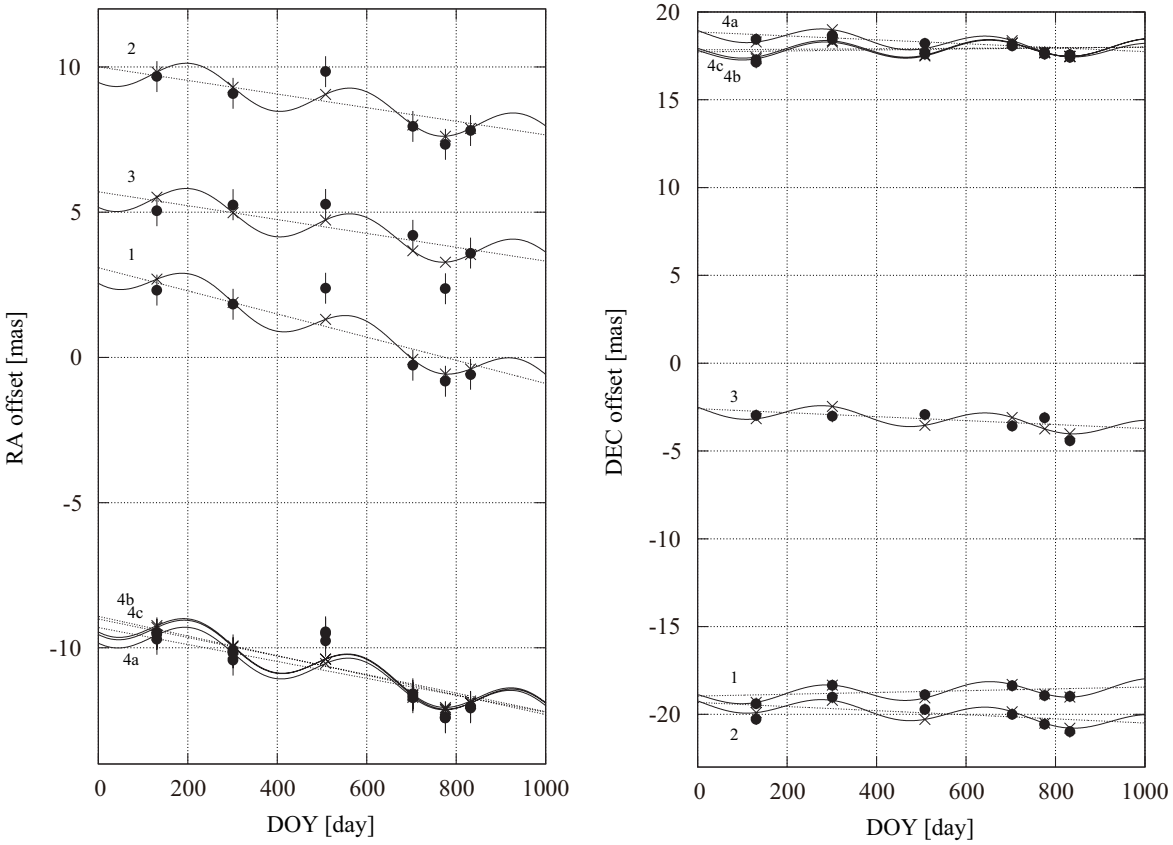

Figure 2.3: Results of fitting the parallax with absolute proper motion. Labels of 1, 2, 3, 4a, 4b, 4c correspond to the LSR velocity $v_{LSR} = -43.10$, -43.80, -44.50, -45.91, -45.20, -46.60 km s^{-1}, respectively. Left : The movement in right ascension as a function of time. The first day is New Year's day, 2008. Black circles and vertical vars represent the position offset of the spots and fitting weight, respectively. Black $\times$-marks represent the ideal position offset of the spots on the least-square fitting. Solid lines and broken lines represent the results of the least-square fitting of absolute proper motion for the spots, and the absolute proper motion modulated by the annual parallax, respectively. Right : The same as the left in declination.

Table 2.2: Parallax and absolute proper motion fitting.

ID	$\Delta\alpha \cos\delta^*$ [mas]	$\Delta\delta^*$ [mas]	$V_{\rm LSR}$ [km s^{-1}]	Epochs used‡ for fitting	$F_{\rm peak}$ [Jy beam^{-1}]	SNR	$\mu_\alpha \cos\delta$ [mas yr^{-1}]	μ_δ [mas yr^{-1}]
1	2.3	-19.4	-43.10	123456	53 - 175	17 - 42	-1.46 ± 0.39	$+0.19 \pm 0.25$
2	9.7	-20.3	-43.80	123456	55 - 228	18 - 32	-0.86 ± 0.39	-0.43 ± 0.25
3	5.0	-3.0	-44.50	123456	53 - 232	13 - 22	-0.87 ± 0.39	-0.41 ± 0.25
4a†	-9.7	18.5	-45.91	123456	9 - 176	12 - 50	-1.06 ± 0.39	-0.41 ± 0.25
4b†	-9.5	17.1	-45.20	123456	104 - 422	19 - 43	-1.23 ± 0.39	$+0.10 \pm 0.25$
4c†	-9.5	17.3	-46.60	123456	0.9 - 40	11 - 50	-1.16 ± 0.39	$+0.05 \pm 0.25$
Average (Standard deviation)							-1.10 (0.30)	-0.16 (0.38)

$*$: The relative coordinate to the phase center at epoch 1.

†: Spots in the same maser feature. Each data in this feature is supposed to be not independence when we estimated the fitting errors.

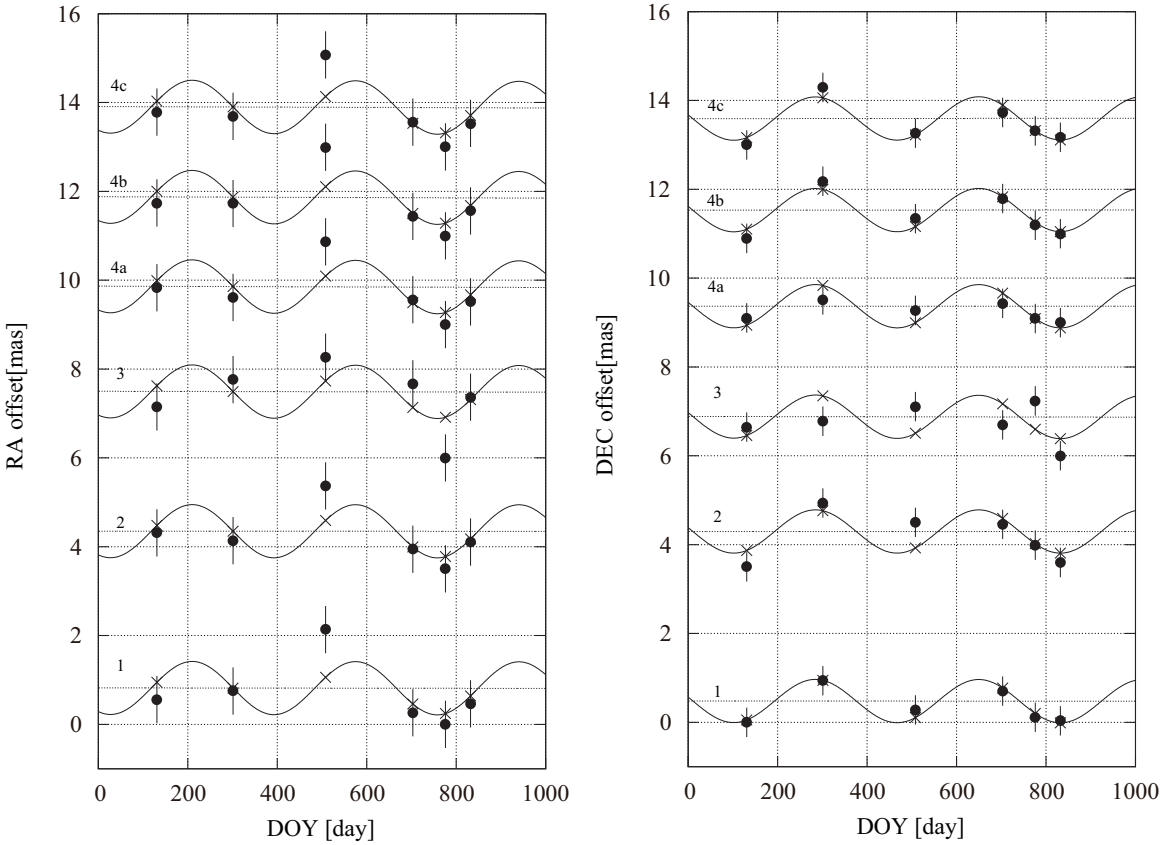

Figure 2.4: Results of positional offsets variation for the maser spots of v_{LSR} = −43.10 (1), −43.80 (2), −44.50 (3), −45.91 (4a), −45.20 (4b), −46.60 (4c) km s^{-1} after subtracting the best-fit proper motions. Left : The movement in right ascension as a function of time. The first day corresponds to New Year's day, 2008. Black circles represent the position offset of the spots with vertical vars as fitting weight. Black ×-marks represent the ideal position offset of the spots on the least-square fitting. Solid lines and broken lines represent the modulation in the positions due to the annual parallax, and the results of subtracting the best-fit absolute proper motion for the spots, respectively. Right : The same as the left in declination. For details refer to tables 2.2 and 2.3.

Table 2.3: Parallax and absolute proper-motion fitting.2

Parallax π [mas]	0.633 ± 0.112
Distance D [kpc]	$1.58\ ^{+0.34}_{-0.24}$
σ_α [mas]	0.53
σ_δ [mas]	0.33

2.4 Discussion

2.4.1 Astrometry with the VERA/JVN

Our parallax value $\pi = 0.633 \pm 0.112$ mas is consistent with Xu et al. (2006) of $\pi = 0.512 \pm 0.010$ mas within their error, and little larger than Hachisuka et al. (2006) of $\pi = 0.489 \pm 0.017$ mas. The average proper motion is $\mu_\alpha \cos\delta = -1.10 \pm 0.30$ mas yr^{-1} and $\mu_\delta = -0.16 \pm 0.38$ mas yr^{-1}. In Xu et al. (2006), average proper motion for nine spots is $\mu_\alpha \cos\delta = -1.204 \pm 0.02$ mas yr^{-1} and $\mu_\delta = -0.147 \pm 0.01$ mas yr^{-1}. Although we did not use the same maser spots as Xu et al. (2006), our average proper motion is consistent with Xu et al. (2006) within the errors. These comparisons ensure that our astrometric results are reliable and do not include unknown systematics. However, the error of the parallax with the JVN/VERA is about 7 or 11 times larger than Hachisuka et al. (2006) and Xu et al. (2006). The largest reason for this error difference is thought to be the difference in baseline length and observational frequency. Both Xu et al. (2006) and Hachisuka et al. (2006) were based on observations with the VLBA. The maximum baseline length of the VERA/JVN is 2,300 km. This length is about 0.27 times that of the VLBA. If the accuracies in phase calibration are the same, the astrometric accuracy is determined by baseline length. Thus, in such a case, the error of parallax for the JVN/VERA simply becomes 3.7 times the error of VLBA. Moreover, our observational frequency was 6.7 GHz, while the frequency in Xu et al. (2006) was 12 GHz and in Hachisuka et al. (2006) was 22 GHz. Therefore, our beam size in synthesis images is about 7-12 times larger than Xu et al. (2006) and Hachisuka et al. (2006) in the worst case. If the phase-referenced map has a low signal-to-noise ratio, the astrometric accuracy would be determined by beam size.

Thus, the error of parallax for the JVN/VERA can be 7-12 times the error of Xu et al. (2006) and Hachisuka et al. (2006). Also, if there are some structures in maser spots, astrometric results can be more influenced with a larger beam. In addition, effects of the ionosphere are also larger in the lower frequency. Given the discussions described above, our results are fairly reasonable when compared with those obtained with the VLBA. Thus, we conclude that the VERA/JVN is able to conduct astrometry for the sources within a few kpc.

The VERA is an array dedicated to astrometry, able to observe many sources routinely. In addition, combination of large telescopes in the JVN (e.g., Usuda 64 m, and Yamaguchi 32 m telescopes) dramatically improves the sensitivity of the array. Also, in near future, the VERA/JVN will expand toward the East Asia VLBI Network including stations in Korea and China, providing a longer baseline up to about 6,000 km and hence better accuracy. On the other hand, the VLBA can only observe methanol maser sources at 12 GHz now, and the European VLBI Network has only three sessions per year for the observation of 6.7 GHz methanol maser. We note that 6.7 GHz methanol maser sources are now becoming more important in the study of the galactic structure with VLBI astrometry (e.g., measuring the spiral structure and galactic rotation; Rygl et al. (2010)), because a 6.7 GHz methanol maser is bright and stationary, and large number of sources have already been discovered in the galactic plane as noted in section 2.1. Therefore, the VERA/JVN can (and the EAVN in near future) will play an important role in the VLBI astrometry of the Galaxy through the observations of 6.7 GHz methanol masers.

2.4.2 Structure of Maser Emitting Region

Based on the previous observations, the structure of the W3(OH) region showed the following characteristics. (i) The ammonia absorption line are associated with the western part of the UC H II region. The NH_3 (2,2) absorption line of W3(OH) suggests that the molecular gas is the front of the torus-like structure overlying UC H II region with a north-south extension (Guilloteau et al. (1983)). They suggest that the back side of the torus cannot be observed because the UC H II region is opti-

cally thick at this wavelength (Dreher & Welch (1981)). (ii) OH maser emissions are more clumpy than that of molecular gas traced with NH_3, but also show continuous distributions along the ammonia absorption line (e.g., Fish & Sjouwerman (2007); Harvey-Smith & Cohen (2006, 2005); Wright et al. (2004a, b); Menten et al. (1992)). Velocities and spatial distributions are basically similar to the 6.7 GHz methanol maser (Menten et al. (1992); Harvey-Smith & Cohen (2006)). (iii) North-south expansion was seen in the internal proper motions of the 1665 MHz OH maser (Bloemhof et al. (1992); Wright et al. (2004b)). In addition, in the 1667 MHz OH maser (Wright et al. (2004a)), there are several arc structures which were suggested to be shock fronts caused by an interaction with the expanding UC H II region. The systemic velocity of the UC H II region can be estimated from the line peak of $C^{18}O$ (1−0) and CS (2−1) in Kim et al. (2006) as being about -39 km s^{-1}. Thus, all OH and methanol maser spots are blue shifted components with respect to the systemic velocity, which suggests that these spots move outward from the UC H II region to the observer. (iv) The velocity gradient in the north-south direction was seen in the 1665 MHz OH maser (Wright et al. (2004b)), which implies rotation from north to south. On the other hand, Fish & Sjouwerman (2007) suggests a rotation in the opposite direction from that suggested by Wright et al. (2004b). The opposite direction of rotation is based on their internal proper motions and newly detected blue-shifted components in the southeast of 6035 MHz OH maser. Thus, there is a disagreement in the rotational direction in the previous observation of OH maser. These differences in the rotation direction from internal proper motion could be dependent on the interpretation of complicated velocity structure of maser clusters. In any case, the structure of NH_3 absorption and OH masers indicates a torus with expansion and clockwise or counter-clockwise rotation.

On the other hand, as seen in figure 2.1, our data suggest that the 6.7 GHz methanol maser spots are only distributed in the western part of UC H II region in our data. The blue-shifted components are mostly located in the northern part and the red-shifted components are located in the southern part. As for the internal proper motions, the separations between cluster C and southern clusters (D - F) increase over

time as seen in figure 2.2. This trend suggests north-south expansion. This sense is consistent with the OH maser motions obtained by Bloemhof et al. (1992) and Wright et al. (2004b). Here, if this expansion is outflow, maser spots belong to the outflow and do not necessarily to have any consistency with UC H II region. However, there exists a maser spot concentration associated with the 'pinch' of the UC H II region (cluster C) - which could be caused by a denser clump in the outlying gas which suppresses the expansion of UC H II region, as suggested by Wright et al. (2004b). This fact suggests an association between the maser clouds and expanding UC H II region. Also, we note that typical expansion velocity of 6.7 GHz methanol maser in figure 2.2 is consistent with that of the UC H II region, 3 - 5 km s^{-1} (Kawamura & Masson (1998)). Therefore, our results favor the expanding torus scenario proposed earlier, whose schematic view is shown in figure 2.5.

The torus model can also naturally explain the excitation of the 6.7 GHz methanol maser. The 6.7 GHz methanol maser is thought to be excited by infrared photons emitted from dusts at the temperature around 100 - 200 K (e.g., De Buizer et al. (2000); Sugiyama et al. (2008a)). In the expanding torus model, we can estimate the dust temperature ($T_{\rm dust}$) by assuming an equilibrium of energies absorbed and re-emitted by dusts. In this estimation, we simply suppose that dusts in the torus are warmed by the central star and re-radiate as a black body with the temperature of $T_{\rm dust}$. Under such an assumption, we can express the temperature of the dust as a function of radial distance from the ionizing star by using the Stefan-Boltzmann's law as,

$$4\pi\sigma r^2 T_{\rm dust}^4 = \frac{\pi r^2}{4\pi R^2} L_*. \tag{2.1}$$

The left-hand side of equation (1) is the luminosity emitted by a spherical dust with a radius of r, and right-hand side is the energy received by the dust from the central star. We also note that L_* is the total luminosity of ionizing star, σ is the Stefan-Boltzmann constant and R is the torus radius. From this equation, the dust temperature $T_{\rm dust}$ can written as,

$$T_{\rm dust} = \frac{1}{2}\left(\frac{L_*}{\pi\sigma R^2}\right)^{\frac{1}{4}}. \tag{2.2}$$

Taking that L_* is 10^5 $L_\odot$ from infrared luminosity by Harper (1974), and the radius

R is 2,000 AU from the 6.7 GHz methanol maser distribution in figure 2.1, we obtain $T_{\rm dust}$ is $\sim$ 110 K. This estimation is consistent with other research reporting the dust temperature of 111 K (Campbell et al. (1989)). Thus, the expanding torus model can also explain the dust temperature which is most suitable for methanol maser excitation. Therefore, the torus model can reasonably explain observed physical properties including the distributions, proper motions and excitations of methanol masers.

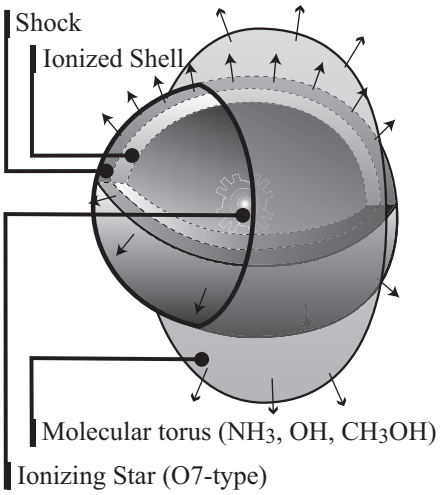

Figure 2.5: A possible model of the W3(OH) region. The UC H II region is expanding and has shell structure as described in Dreher & Welch (1981). Several maser emissions and NH_3 absorption come from the molecular torus out of the UC H II region. Only the front of the torus can be observed because the UC H II region is optically thick at those wavelengths. The molecular torus expands with the expansion of the UC H II region.

2.4.3 Conclusion

We have presented the results of multi-epoch VLBI astrometry with JVN/VERA for the 6.7 GHz methanol maser associated with W3(OH). We derived the annual parallax of W3(OH) with the five maser spots to be 0.633 $\pm$ 0.112 mas, corresponding to the

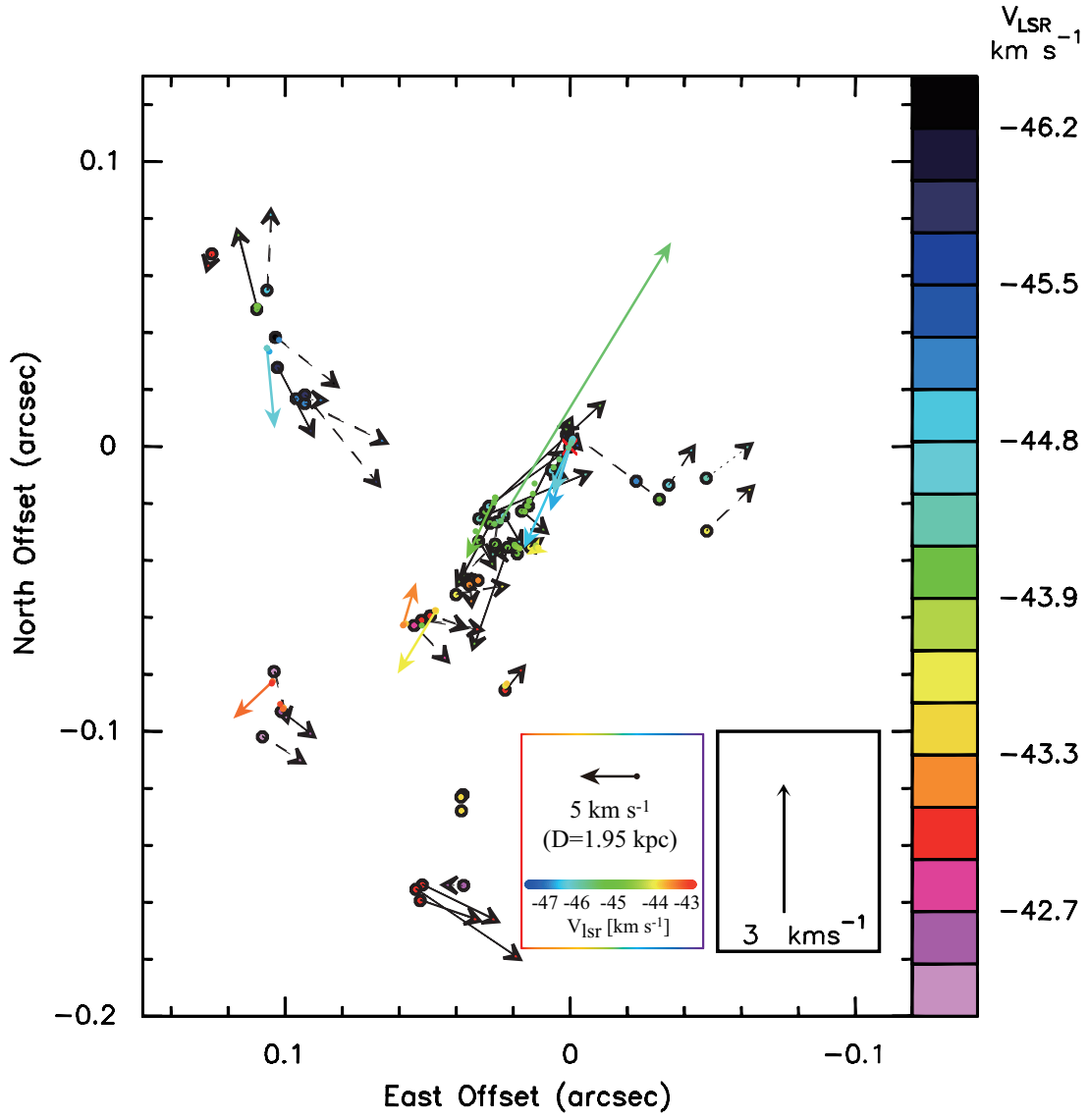

Figure 2.6: Maser proper motions in the cluster C with Moscadelli et al. (2010). Our results are plotted with colored vector, and the proper motions of Moscadelli et al. (2010) are plotted with black vector. Each color of systemic velocity is showed in colored square (our results) and right-hand side (Moscadelli et al. (2010)).

distance of $1.58^{+0.34}_{-0.24}$ kpc from the Sun. Absolute proper motions were also measured for the six maser spots. These are the first results of JVN/VERA astrometry for 6.7 GHz methanol maser sources.

Internal proper motions of 6.7 GHz methanol masers toward W3(OH) were also obtained. The motions of the tendency to expand are similar to previous 1.6 GHz OH maser observations Bloemhof et al. (1992) and Wright et al. (2004b), and favor that the torus with rotation and expansion following to the UC H II region.

Chapter 3

Fringe Check Observations of 6.7 GHz Methanol Maser with the VERA/JVN

3.1 Introduction

To date, more than 1,000 methanol maser sources have been discovered (Caswell (2009), Caswell (2010); Pandian et al. (2007); Pestalozzi et al. (2005), Pestalozzi et al. (2007); Szymczak et al. (2002); Green et al. (2010)). Among methanol maser lines, a 6.7 GHz line is the strongest and allows for VLBI observations of distant massive star-forming regions in detail. In the 6.7 GHz methanol maser catalog of Pestalozzi et al. (2005), most of methanol maser sources are located at $|l| < 40°$ (see figure 1.5). The 6.7 GHz methanol maser is generally thought to trace the disk (e.g., Minier et al. (2000)) or low velocity outflow (e.g., Walsh et al. (1998)) with the small velocity range less than $\approx$10 km s^{-1}, and the internal proper motion is generally much smaller than H_2O maser which traces high/low velocity flow (e.g., Elitzur (1992)) or disk (e.g., Seth et al. (2002)) with velocity ranges from several dozen to over 100 km s^{-1}. Thus VLBI astrometry of 6.7 GHz methanol maser sources, which could provide high accuracy proper motions on the sky plane with milliarcsecond (mas) scale, is excepted to be

useful to trace Galactic kinematics around the bar.

Generally, maser structure is compact. However, SiO and H_2O maser sources are still partially resolved out at long baselines of VLBI. Similarly, 6.7 GHz methanol maser sources are partially resolved out at long baselines. Thus we have to investigate fluxes of target sources with respect to each baseline of the JVN/VERA, and select observable sources for astrometry. In this chapter, we report about our fringe check observations of 6.7 GHz methanol maser sources and their reference sources, which will provide potential candidates of VLBI astrometry to investigate the bar structure in the Milky Way Galaxy.

3.2 Source Selection

3.2.1 Criteria for Source Selection

For the fringe check observations, we selected sources from the 6.7 GHz methanol maser catalog of Pestalozzi et al. (2005). In our source selections, in addition to declination more than $-37°$ for observations in the Northern Hemisphere, we used four criteria as follows: [1] The galactic longitude of $|l| < 40°$: Our target sources are expected to be associated with the Galactic bar structure or rings/arms possibly excited by the bar. [2] The kinematic distances from the galactic center $D_{GC} < 5$ kpc: This limitation is also based on the first criterion to select the sources around the bar. We made this condition after U08299B, and did not use the criterion within $|l| < 3°$ where is large indefiniteness for distances. [3] The flux of 15 Jy or more at single dish observations: We referred to the fluxes in Pestalozzi et al. (2005). A flux of more than 15 Jy have a high probability to be detected. However, we also observed some weak sources on a trial basis (G 0.21−0.00, G 0.39−0.03, G 0.49+0.18). [4] Maser sources have one or more detectable reference sources (QSOs) with the JVN/VERA within a separation of 4°: We chose the reference sources with the peak flux of about 100 mJy beam^{-1} or more at 8 GHz (X-band) in the VLBA Calibrator List (`http://www.vlba.nrao.edu/astro/calib/`).

Table 3.1: An Objects List for Fringe Check Observation 1.

No.	Source Name	R.A.* (J2000)	Dec* (J2000)	$V^*_{\rm LSR}$ [km s^{-1}]	$Flux^*_{\rm peak}$ [Jy]	$D^*_{\rm GC}$ [kpc]
1	G 350.10+0.08	17h19m27.03s	−37d10'53.5"	−74	41	2.8
2	G 350.29+0.12	17h19m50.86s	−37d00'0.5"	−64	26.9	3
3	G 351.41+0.64	17h20m53.37s	−35d47'02"	−10	3300	6.5
4	G 351.58−0.35	17h25m25.19s	−36d12'45.5"	−95	63	2.1
5	G 353.40−0.36	17h30m26.18s	−34d41'45"	−20	90	4.7
6	G 354.61+0.47	17h30m16.8s	−33d14'13"	−23	216	3.9
7	G 354.72+0.30	17h31m15.55s	−33d14'06"	93	16	0
8	G 358.27−2.08	17h49m41.6s	−31d29'30"	5.2	16.2	0
9	G 359.13+0.03	17h43m25.67s	−29d39'17.5"	−4	17	3.8
10	G 359.43−0.10	17h44m40.66s	−29d28'17.6"	−52	27	0.3
11	G 359.61−0.24	17h45m39.08s	−29d23'29"	22.5	48	0
12	G 0.21−0.00	17h46m07.66s	−28d45'20"	49.2	3.5	0.1
13	G 0.31−0.20	17h47m09.12s	−28d46'16"	18	41.2	0.5
14	G 0.39−0.03	17h46m41.12s	−28d37'05.5"	28.7	5.8	0.4
15	G 0.49+0.18	17h46m04s	−28d24'51.5"	0.8	10	5.9
16	G 0.54−0.85	17h50m14.53s	−28d54'31"	14	68	1
17	G 0.64−0.04	17h47m18.65s	−28d24'25"	49.1	69	0.4
18	G 0.66−0.02	17h47m18.61s	−28d22'56"	72.2	33.7	0.3
19	G 0.69−0.03	17h47m24.81s	−28d21'43.5"	68.5	26	0.3
20	G 2.14+0.01	17h50m35.5s	−27d05'55"	63	88	5.8
21	G 6.78−0.27	18h01m57.2s	−23d12'37"	26.9	146.4	4.1
22	G 8.68−0.36	18h06m23.5s	−21d37'23"	43	148	3.6
23	G 9.98−0.02	18h07m50.11s	−20d18'57"	44	35.4	3.9

∗: Pestalozzi et al . (2007)

Table 3.1: Continue.

No.	Source Name	R.A.* (J2000)	Dec* (J2000)	$V^*_{\rm LSR}$ [km s^{-1}]	$Flux^*_{\rm peak}$ [Jy]	$D^*_{\rm GC}$ [kpc]
24	G 10.44−0.01	18h08m44.9s	−19d54'38"	73	25	2.9
25	G 10.47+0.02	18h08m38.21s	−19d51'49.5"	75	61	2.9
26	G 11.90−0.14	18h12m11.44s	−18d41'29"	42.6	49	4.3
27	G 11.93−0.61	18h14m0.89s	−18d53'26.5"	32	47	4.9
28	G 12.02−0.03	18h12m01.851s	−18d31'55.5"	108	82	2.4
29	G 12.68−0.18	18h13m54.2s	−18d01'44"	52	544	4
30	G 12.71−0.11	18h13m43.4s	−17d58'06"	57.7	264	3.8
31	G 12.89+0.49	18h11m51.4s	−17d31'30"	39	93	4.7
32	G 12.90−0.26	18h14m39.52s	−17d52'00"	39	317	4.7
33	G 13.65−0.57	18h17m18.6s	−17d21'50"	51	33	4.2
34	G 15.67−0.48	18h20m58.3s	−15d32'34"	−3.4	33	9.1
35	G 16.58−0.05	18h21m09.13s	−14d31'48.5"	59	21	4.3
36	G 18.34+1.78	18h17m54.1s	−12d06'48"	27.7	65	6
37	G 18.46−0.00	18h24m36.35s	−12d51'08"	49	23	4.9
38	G 18.65+0.04	18h24m48.7s	−12d39'17"	80.2	22	3.9
39	G 20.24+0.08	18h27m41s	−11d14'05"	71.4	94	4.3
40	G 23.01−0.41	18h34m40.2s	−09d00'36"	75	405	4.5
41	G 23.04−0.32	18h34m26.2s	−08d56'35"	75	29	4.5
42	G 23.19−0.38	18h34m54.4s	−08d50'04"	81.8	23.4	4.3
43	G 23.39+0.19	18h33m13.1s	−08d23'56"	74.1	17	4.5
44	G 23.43−0.18	18h34m39.27s	−08d31' 39"	103	77	3.8
45	G 23.98−0.08	18h35m22.9s	−08d01'11"	70.9	17	4.7
46	G 24.50−0.03	18h36m08.7s	−07d30'55"	114.4	29	3.7
47	G 24.54+0.32	18h34m53s	−07d19'11"	106.2	15	3.8
48	G 24.78+0.08	18h36m12.57s	−07d12'11.5"	113	97	3.7
49	G 25.41+0.10	18h37m16.92s	−06d38'28"	96	24.9	4.1
50	G 25.65+1.04	18h34m20.91s	−05d59'40.5"	41.9	178	5.9

∗: Pestalozzi et al . (2007)

Table 3.1: Continue.

No.	Source Name	R.A.* (J2000)	Dec* (J2000)	$V^*_{\rm LSR}$ [km s^{-1}]	$Flux^*_{\rm peak}$ [Jy]	$D^*_{\rm GC}$ [kpc]
51	G 25.70+0.04	18h38m03.15s	−06d24'15"	92.8	364	4.2
52	G 25.82−0.17	18h39m03.63s	−06d24'09.5"	91.2	70	4.3
53	G 26.60−0.22	18h40m38.55s	−05d43'56"	109	19	3.9
54	G 27.22+0.13	18h40m30.43s	−05d00'59"	118	22	3.8
55	G 27.36−0.16	18h41m50.98s	−05d01'28"	99.4	29	4.2
56	G 28.14+0.00	18h42m42.59s	−04d15'32"	100.9	34	4.2
57	G 28.30−0.38	18h44m21.99s	−04d17'38.5"	80.7	62	4.7
58	G 28.82+0.48	18h42m12.43s	−03d25'39.5"	83.3	65	4.7
59	G 28.83−0.25	18h44m51.09s	−03d45'48"	86	73	4.6
60	G 29.86−0.04	18h45m59.53s	−02d44'47"	101.4	67	4.3
61	G 29.95−0.02	18h46m03.741s	−02d39'21.43"	96	206	4.5
62	G 30.20−0.17	18h47m03.5s	−02d30'31"	108	18.7	4.2
63	G 30.70−0.07	18h47m36.9s	−02d01'05"	88	87	4.7
64	G 30.76−0.05	18h47m39.73s	−01d57'22"	92	68	4.6
65	G 30.78+0.00	18h47m29.9s	−01d54'39"	91.5	23	4.6
66	G 30.79+0.20	18h46m48.09s	−01d48'46"	86	23	4.7
67	G 30.82−0.05	18h47m46.2s	−01d54'14"	101	18	4.4
68	G 30.91+0.14	18h47m15s	−01d44'07"	104	95.2	4.3
69	G 30.94+0.11	18h47m23.8s	−01d42'39"	101.5	33	4.4
70	G 31.28+0.06	18h48m12.39s	−01d26'22.6"	110	71	4.2
71	G 32.03+0.06	18h49m37.3s	−00d45'47"	92.8	93	4.7
72	G 32.11+0.09	18h49m36.7s	−00d41'05"	93.2	31	4.7
73	G 32.97+0.04	18h51m23s	+00d03'46"	91.7	27	4.7
74	G 33.09−0.07	18h51m58.9s	+00d07'27"	96	30	4.6
75	G 33.40+0.01	18h52m10.6s	+00d25'09"	105	20	4.5

∗: Pestalozzi et al . (2007)

3.2.2 Fringe Check Observations

We conducted the fringe check observations with six sessions from October 2008 to June 2009 with the JVN/VERA (table 3.2). A total of 75 maser sources were observed (see table 3.1; source selection is section 3.2.1). 28 QSOs were also observed in the fringe check (table 3.4) for following phase referencing in chapter 4.

Radio frequency of 6.668518 GHz was adopted as the rest frequency of CH_3OH $5_1 \rightarrow 6_0A^+$ transition. At the start of each observation, G 9.62+0.19 was scanned for 3 minutes for system check. Totally, on-source time of each maser source was 4 - 7 minutes, and on-source time of each reference source was 5 - 10 minutes. In each observation schedule, G 9.62+0.19 was observed for 5 minutes once one hour as an amplitude calibrator at the JVN observation (U08299B and U09155A). On the other hand, in the observations only with the VERA stations (R09153A - R09162B), the amplitude calibration values were obtained with R-SKY instead of the amplitude calibrator just before each observation.[1] 3C 345, 3C 418 and NRAO 530 were also observed about 5 minute once one hour as a calibrator for clock, clock delay and band pass calibrations. In our observations, left-handed circular polarization was received in each antenna and epoch after U08299B. At U08299B, linearly polarized receivers were used in Iriki and Ishigaki stations, and left-handed circular polarized receivers were used in other stations. After U08299B, their linearly polarized receivers were replaced with new receivers receiving left-hand circular polarization.

The received signals were filtered in a 16 MHz bandwidth channel (U08299B and U09141A), or 16 bandwidth channels with 16 MHz bandwidth each (R09153A - R09162B). Filtered signals were recorded with SONY DIR1000 recorder at a rate of 128 Mbit s^{-1} (U08299B and U09141A) or DIR2000 recorder at a rate of 1024 Mbit s^{-1} (R09153A-R09162B). The recorded signals were correlated with the Mitaka FX correlator (Chikada et al. (1991)). The correlated data recorded with DIR1000 had a bandwidth channel with 16 MHz bandwidth, and 1024 spectral channels in auto-correlation and cross-correlation spectra, respectively. Thus, a frequency spacing of

[1]We used system temperature at EL= 0° and optical depth of atmosphere τ_0 at Sec$Z$ for amplitude calibration. In the receive system of 6.7 GHz band at VERA, room temperature was obtained with noise diode instead of traditional absorber.

maser data was 15.63 kHz ($\sim$ 0.72 km s^{-1}). As for the maser data recorded with DIR2000, we selected a small portion of two 8 MHz bandwidth channels centered at the maser line to obtain high spectral resolution in the maser correlation process. In this process, auto-correlation and cross-correlation spectra were consisted of 512 spectral channels. Thus, a frequency spacing of maser data was 15.63 kHz ($\sim$0.72 km s^{-1}) as in the data recorded with DIR1000. On the other hand, as for the QSOs data recorded with DIR2000, we selected all 16 bandwidth channels with 16 MHz bandwidth and 128 spectral channels in each base band channel.

Table 3.2: Summary of fringe check observations.

Epoch	Obs. Code *yyddd*	Duration [UT]	Antennas†	Calibrator
1	U08299B	06:00 - 09:55	M, R, S, Y, U	3C 345
2	U09141A	14:00 - 18:00	R, O, Y, U	3C 345, NRAO 530
3	R09153A	15:30 - 22:41	M, R, O, S	3C 345, NRAO 530
4	R09155A	15:30 - 21:03	M, R, O, S	3C 345, NRAO 530
5	R09161A	19:30 - 22:03	M, R, O, S	3C 345, 3C 418
6	R09162B	12:00 - 22:11	M, R, O	3C 345, 3C 418, NRAO 530

†: M=Mizusawa 20 m, R=Iriki 20m, S=Ishigaki 20 m, O=Ogasawara 20 m, Y=Yamaguchi 32 m, U=Usuda 64 m

3.3 Data Analysis

We analyzed the data using the NRAO AIPS package basically in a standard manner. The delay and delay-rate offsets were calibrated using 3C 345 and NRAO 530. Bandpass responses were also calibrated using 3C 345 and NRAO 530. Amplitude calibrations were performed by template method with total-power spectrum of G 9.62+0.19 at Yamaguchi station for U08299B and U09141A. For other observations, we used system temperatures estimated from R-SKY to calibrate amplitude. The system temperature estimated from R-SKY can be obtained as

$$T_{\rm sys} = T_{\rm sky}(1 - e^{-\tau}) + T_{\rm rx}, \tag{3.1}$$

$$\tau = \tau_0 \sec Z, \tag{3.2}$$

where atmosphere is parallel plate air, $T_{\rm sys}$ [K] is system temperature, Z [deg] is zenith direction of the elevation of antenna, $T_{\rm sky}$ [K] is sky temperature, $T_{\rm rx}$ [K] is receiver temperature, τ is optical depth of atmosphere, and τ_0 is optical depth for zenith direction.

For data of Iriki and Ogasawara station at U08299B, we also applied special amplitude calibration to correct for polarization difference (linear/circular) using a method described in Sugiyama et al. (2008b). Fringe solutions were obtained by all calibrators and reference sources. Finally we used a detection criterion of 5σ.

3.4 Results and Discussion of Fringe Check Observations

Results of the fringe check observations are listed in table 3.3 and table 3.4 for maser sources and for reference sources, respectively. Figure 3.1 also show results of the fringe check observations with l-v diagram. An accuracy of the flux information in these tables are typically $\sim$10 %. Among 75 sources observed, 26 sources were detected with signal-to-noise ratio of 5σ or larger at baselines of more than 1,000 km, corresponding to a detection rate of 35 % (The shortest baseline length is $\sim$1,019 km in the VERA.). Thus 6.7 GHz methanol maser sources are highly resolved out at 1,000 km order baselines. However, time variation of the maser flux of each sources is not considered here. In addition, there was no detectable phase-reference sources for 9 sources out of 26 sources. Thus, 17 sources were detected with more than 1,000 km baseline and have detectable phase-reference sources for astrometry. As reference, only one source which is the brightest one in our sample with flux is lower than 15 Jy, G 0.49+0.18 was detected with shorter base line at $\sim$300 - 880 km. This indicates that the source with a total power flux above $\sim$10 Jy have a possibility to be detected at shorter baselines with VLBI observation.

If we assumes the same detection rate for all 140 sources with a flux larger than 15 Jy and declination more than -36 degree in Pestalozzi et al. (2005), 49 sources (which is 35% of 140 sources) are expected to be detectable with more than 1,000 km baselines of the JVN/VERA.

Figure 3.2 also show the result of our fringe check observation. We can see that the number of the detected sources distribute every longitude contrary to bias of the number of the observed sources. With a increasing trend of number of observed sources to the higher galactic longitude, there is same trend for the number of the detected sources about the galactic longitude.

For astrometry observations in chapter 4, we finally chose ten maser sources which are relatively easy to observe with phase referencing about brighter flux and detectable source at longer baseline with only the VERA antennas. The selected sources are marked with filled-star (★) in table 3.3.

Since methanol masers are resolved significantly with more than 1,000 km baselines of the VERA, observations with medium-length/high-sensitive baselines of the JVN are effective to increase observable sources. More 7 sources marked with $\circ$ and $\odot$ in table 3.3 can be observed with the JVN.

In addition to the spacial resolved out, a low velocity resolution is also considered to give the low detection rate, because each maser line is not frequently resolved enough and could be averaged with noise signal in each velocity channel. The ideal velocity resolution is maybe less than 0.1 km s^{-1} from the maser line width around 0.1 km s^{-1} (Szymczak & Kus (2000)), which is 7 times smaller than the highest resolution of DIR 2000 recording in the VERA. In the near future, VERA will be start to fully operate with software correlator and solve this problem.

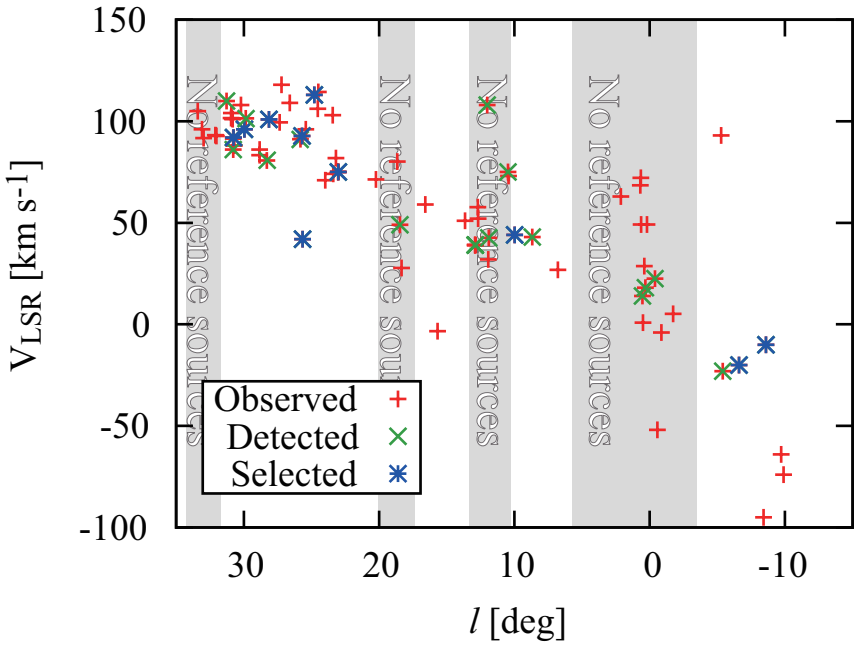

Figure 3.1: A l-v diagram of the results of the fringe check observations with the VERA/JVN. Red colored points show observed sources. Green colored points show detected sources with signal to noise ratio of more than 5σ at $\sim$1,000 km or longer baseline. Blue colored points show selected sources for following astrometry. There are no phase-reference sources in gray colored regions.

Table 3.3: Results of Fringe Check Observation 1.

	Array	RY	UY	UR	RS	OU	RO	MR	OY	SY	MO	OS	US	MS	Obs. Code
	Source Name	[Jy]	[Jy]	[Jy]	[Jy]	[Jy]	[Jy]	[Jy]	[Jy]	[Jy]	[Jy]	[Jy]	[Jy]	[Jy]	∗yyddd∗
◯	G 350.10+0.08	-	-	-	-	-	<2.5	<2	-	-	<2	-	-	-	R09162B
◯	G 350.29+0.12	-	-	-	-	-	< 2	<2	-	-	<2.5	-	-	-	R09162B
◯	G 351.58−0.35	-	-	-	-	-	<3	<3	-	-	<3	-	-	-	R09162B
◯◎★	G 351.41+0.64	-	200 (2)	-	-	-	-	-	-	193 (2)	-	-	59 (1)	-	U08299B†
◯◎★	G 353.40−0.36	6 (1.8)	8 (0.5)	5 (0.8)	-	25 (0.5)	20 (3)	-	<2	-	-	-	-	-	U09141A
◯	G 354.72+0.30	1.2 (1)	1 (0.2)	<0.4	-	1 (0.5)	<2	-	<1	-	-	-	-	-	U09141A
◯ ⊙	G 354.61+0.47	4 (1)	2.2 (0.3)	<0.4	-	6 (0.5)	<2	-	2.5 (1)	-	-	-	-	-	U09141A
	G 358.27−2.08	-	-	-	-	-	<3.5	<3	-	-	<2	-	-	-	R09162B
		-	-	-	<1	-	-	<1	-	-	-	-	-	<1	R09153A
	G 359.13+0.03	-	-	-	<1	-	-	<1	-	-	-	-	-	<1	R09153A
		-	-	-	-	-	<3	<3	-	-	<2.5	-	-	-	R09162B
	G 359.43−0.10	-	-	-	<1	-	-	<1	-	-	-	-	-	<0.8	R09153A
		-	-	-	-	-	-	<3	-	-	<3	-	-	-	R09162B
⊙	G 359.61−0.24	-	-	-	-	-	<2	<3	-	-	<3	-	-	-	R09162B
		7 (1)	2 (0.3)	1.3 (0.1)	-	6 (0.5)	<3	-	5 (1)	-	-	-	-	-	U09141A
	G 0.21−0.00	-	-	-	<1	-	-	<1	-	-	-	-	-	<1	R09153A
◎	G 0.31−0.20	9 (1)	6 (0.2)	7.5 (0.5)	-	9 (0.5)	10 (2)	-	13 (1)	-	-	-	-	-	U09141A
		-	-	-	-	-	<1.1	<0.8	-	-	2.5 (1)	-	-	-	R09162B
	G 0.39−0.03	-	-	-	-	-	-	-	-	-	-	-	-	-	U08299B
△	G 0.49+0.18	16 (3)	3.5 (0.3)	6.5 (1.5)	<5	-	-	-	-	<2	-	-	2 (0.5)	-	U08299B
◎	G 0.54−0.85	-	40.5 (0.5)	-	-	-	-	-	-	29 (1.5)	-	-	23 (1.8)	-	U08299B

†: Error of the calibrated fluxes could be larger than 10 %, especially U08299B.
‡: There is a possibility of splias.
★: Target sources of phase reference observations.
◯: Reference sources were detected with a detection limit of 5σ.
◎: Fringe detected (or expected to be detected) with the baseline length more than 1,000 km and a detection limit of 5σ at only VERA baselines.
⊙: Fringe detected (or expected to be detected) with the baseline length more than 1,000 km and a detection limit of 5σ at the baselines include Yamaguchi and/or Usuda.
△: Fringe detected (or expected to be detected) enough with the baseline length less than 1,000 km and a detection limit of 5σ.
-: Lack of baseline data since observation trouble or absent station.
(...) or <... : 1σ noise level.

Table 3.3: Results of Fringe Check Observation 2.

	Array	RY	UY	UR	RS	OU	RO	MR	OY	SY	MO	OS	US	MS	Obs. Code
	Source Name	[Jy]	[Jy]	[Jy]	[Jy]	[Jy]	[Jy]	[Jy]	[Jy]	[Jy]	[Jy]	[Jy]	[Jy]	[Jy]	*yyddd*
△	G 0.64−0.04	-	14 (0.6)	-	-	-	-	-	-	7 (1.5)	-	-	2.3 (0.7)	-	U08299B
△	G 0.66−0.02	11 (2)	18.5 (0.5)	9 (1)	<3.5	-	-	-	-	5.7 (1.5)	-	-	<0.8	-	U08299B†
△	G 0.69−0.03	-	1.6 (0.3)	-	-	-	-	-	-	<1.2	-	-	0.6 (0.6)	-	U08299B†
	G 2.14+0.01	-	-	-	<1	-	-	<1	-	-	-	-	-	<1	R09153A
◯△	G 6.78−0.27	5 (1)	7.7 (0.3)	<0.4	-	<0.5	<2	-	<1	-	-	-	-	-	U09141A
◯ ⊙	G 8.68−0.36	22 (1)	3.3 (0.2)	1.2 (0.3)	-	4 (0.2)	<1	-	<1	-	-	-	-	-	U09141A
◯◎★	G 9.98−0.02	-	-	-	1 (0.2)	-	0.5 (0.3)	1.2 (0.2)	-	-	2.5 (0.5)	<0.3	-	<0.4	R09155A
●	G 9.62+0.19	-	-	-	160 (2)	-	-	150 (2)	-	-	-	-	-	110 (2)	R09153A
		150	200	90	-	85	250	-	240	-	-	-	-	-	U09141A
		-	-	-	44 (1)	-	1.6 (0.4)	33 (2)	-	-	2 (0.5)	10 (1)	-	2.5 (0.5)	R09161A
		4100 (3)	1530 (3)	1300 (3)	1380 (3)	-	-	-	-	1040 (3)	-	-	380 (3)	-	U08299B†
	G 10.44−0.01	-	-	-	<0.3	-	<2.5	<2.5	-	-	<0.3	<0.5	-	<0.4	R09155A
⊙	G 10.47+0.02	4 (1)	1.5 (0.3)	1 (0.3)	-	3 (0.3)	2 (2)	-	3 (1)	-	-	-	-	-	U09141A
◎	G 11.90−0.14	57 (3)	53 (0.5)	49 (2)	47 (4)	-	-	-	-	41 (2)	-	-	33	-	U08299B
	G 11.93−0.61	-	-	-	<0.3	-	<0.3	0.9 (0.3)	-	-	0.9 (0.3)	<0.3	-	<0.4	R09155A
◎	G 12.02−0.03	30 (3)	31 (0.5)	19 (1)	-	26 (1)	19 (3)	-	24 (2)	-	-	-	-	-	U09141A
	G 12.68−0.18	28 (2)	<0.6	<1	-	<1	<4	-	<3	-	-	-	-	-	U09141A
	G 12.71−0.11	-	-	-	<0.4	-	<0.4	<0.4	-	-	<0.3	<0.4	-	<0.4	R09155A
⊙	G 12.89+0.49	-	-	-	<1	-	2 (1)	<1	-	-	3.5 (1)	<1	-	5 (1)	R09153A
◎	G 12.90−0.26	24 (1)	20 (0.3)	45 (0.5)	-	29 (0.3)	23 (1)	-	15 (1)	-	-	-	-	-	U09141A
◯	G 13.65−0.57	-	-	-	<1	-	<1	<1	-	-	<1	<1	-	<1	R09153A
◯	G 15.67−0.48	-	<0.6	-	-	-	-	-	-	<2	-	-	<0.9	-	U08299B†

†: Error of the calibrated fluxes could be larger than 10 %, especially U08299B.
‡: There is a possibility of splias.
●: An amplitude calibrator.
★: Target sources of phase reference observations.
◯: Reference sources were detected with a detection limit of 5σ.
◎: Fringe detected (or expected to be detected) with the baseline length more than 1,000 km and a detection limit of 5σ at only VERA baselines.
⊙: Fringe detected (or expected to be detected) with the baseline length more than 1,000 km and a detection limit of 5σ at the baselines include Yamaguchi and/or Usuda.
△: Fringe detected (or expected to be detected) enough with the baseline length less than 1,000 km and a detection limit of 5σ.
-: Lack of baseline data since observation trouble or absent station.
(...) or <... : 1σ noise level.

Table 3.3: Results of Fringe Check Observation 3.

	Array	RY	UY	UR	RS	OU	RO	MR	OY	SY	MO	OS	US	MS	Obs. Code
	Source Name	[Jy]	[Jy]	[Jy]	[Jy]	[Jy]	[Jy]	[Jy]	[Jy]	[Jy]	[Jy]	[Jy]	[Jy]	[Jy]	∗yyddd∗
◯	G 16.58−0.05	-	-	-	<1	-	<1	<1	-	-	3 (1)	<1	-	<1	R09153A
	G 18.34+1.78	<3.5	<0.5	<1.3	<7	-	-	-	-	<3	-	-	<1.2	-	U08299B†
⊙	G 18.46−0.00	7.5 (1)	4.5 (0.3)	4 (0.3)	-	2.8 (0.5)	<1.5	-	<1	-	-	-	-	-	U09141A
	G 18.65+0.04	<1	<0.2	<0.4	-	<0.4	<2	-	<1	-	-	-	-	-	U09141A
◯	G 20.24+0.08	-	-	-	<1	-	<1	<1	-	-	<1	<1	-	<0.8	R09153A
◯◎ ★	G 23.01−0.41	23 (1)	48 (0.5)	33 (0.5)	-	8 (0.5)	12 (1.5)	-	10 (1)	-	-	-	-	-	U09141A
◯	G 23.04−0.32	-	-	-	<1	-	<1	<1	-	-	<1	<0.8	-	<0.8	R09153A
◯	G 23.19−0.38	-	-	-	<0.8	-	<1	<1	-	-	<1	<0.8	-	<1	R09153A
◯	G 23.39+0.19	-	-	-	<1	-	<1	<1	-	-	<1	<1	-	<0.8	R09153A
◯	G 23.43−0.18	-	-	-	<1	-	<1	<1	-	-	<1	<1	-	<0.8	R09153A
◯	G 23.98−0.08	-	-	-	<1	-	<1	<1	-	-	<1	<0.8	-	<1	R09153A
◯	G 24.50−0.03	<0.8	<0.2	<0.3	-	<0.3	<1	-	<1	-	-	-	-	-	U09141A
◯	G 24.54+0.32	-	-	-	<1	-	<1	<1	-	-	<1	<1	-	<0.8	R09153A
◯◎★	G 24.78+0.08	10 (1)	5 (0.2)	14 (0.3)	-	10 (0.3)	15 (1)	-	6 (1)	-	-	-	-	-	U09141A
	G 25.41+0.10	-	-	-	<1	-	<1	<1	-	-	<1	<1	-	<0.8	R09153A
◯◎ ★	G 25.65+1.04	42 (2.5)	61 (2)	18.5 (1)	71 (2.5)	-	-	-	-	25 (1)	-	-	8 (0.5)	-	U08299B†
◯◎★	G 25.70+0.04	450 (2)	230 (2)	107 (2)	24 (3)	-	-	-	-	<1.5	-	-	1.8 (0.7)	-	U08299B†
◯ ⊙	G 25.82−0.17	-	-	-	2.5 (1)	-	<1	2.3 (1)	-	-	5.5 (1)	<1	-	<1	R09153A
◯	G 26.60−0.22	<0.8	<0.2	<0.3	-	<0.4	<1.5	-	<1	-	-	-	-	-	U09141A
◯	G 27.22+0.13	5 (0.8)	0.8 (0.2)	<0.8	-	<0.4	<1.5	-	<1	-	-	-	-	-	U09141A
◯	G 27.36−0.16	-	-	-	<1	-	<1	3.5 (1)	-	-	<1	<0.8	-	<0.8	R09153A

†: Error of the calibrated fluxes could be larger than 10 %, especially U08299B.
‡: There is a possibility of splias.
★: Target sources of phase reference observations.
◯: Reference sources were detected with a detection limit of 5σ.
◎: Fringe detected (or expected to be detected) with the baseline length more than 1,000 km and a detection limit of 5σ at only VERA baselines.
⊙: Fringe detected (or expected to be detected) with the baseline length more than 1,000 km and a detection limit of 5σ at the baselines include Yamaguchi and/or Usuda.
△: Fringe detected (or expected to be detected) enough with the baseline length less than 1,000 km and a detection limit of 5σ.
-: Lack of baseline data since observation trouble or absent station.
(...) or <... : 1σ noise level.

Table 3.3: Results of Fringe Check Observation 4.

	Array	RY	UY	UR	RS	OU	RO	MR	OY	SY	MO	OS	US	MS	Obs. Code
	Source Name	[Jy]	[Jy]	[Jy]	[Jy]	[Jy]	[Jy]	[Jy]	[Jy]	[Jy]	[Jy]	[Jy]	[Jy]	[Jy]	∗yyddd∗
○◎ ★	G 28.14+0.00	-	-	-	<1	-	<1.5	<1	-	-	6 (1)	<1	-	3 (1)	R09153A
○ ⊙	G 28.30−0.38	-	-	-	<1	-	<1	<1	-	-	4 (1)	<1	-	<1	R09153A
○	G 28.82+0.48	-	-	-	<0.8	-	<0.8	<1	-	-	<1	<0.8	-	<1	R09161A
○ ⊙	G 29.86−0.04	-	-	-	2.5 (0.8)	-	<0.8	<1	-	-	<1	2 (1)	-	<1	R09161A
○◎ ★	G 29.95−0.02	63 (1)	20 (0.3)	23 (0.3)	-	40 (1)	17 (1)	-	10 (1)	-	-	-	-	-	U09141A
○	G 30.20−0.17	-	-	-	<0.3	-	<0.3	<0.4	-	-	<0.3	<0.3	-	<0.4	R09161A
○	G 30.70−0.07	-	-	-	<1	-	<1	<1	-	-	<1	<1	-	<1	R09161A
○◎★	G 30.76−0.05	-	-	-	4.5 (1)	-	<1	2.5 (1)	-	-	10 (1)	4 (1)	-	1.2 (0.8)	R09153A
○	G 30.78+0.00	-	-	-	<1	-	<1	<1	-	-	<1	<1	-	<0.8	R09153A
○ ⊙	G 30.79+0.20	1.7 (0.8)	1.8 (0.3)	1.5 (0.3)	-	2 (0.3)	4 (1)	-	<1	-	-	-	-	-	U09141A
○	G 30.82−0.05	-	-	-	<1	-	<1	<1	-	-	<1	<1	-	<0.8	R09153A
○	G 30.91+0.14	<0.8	<0.2	<0.3	-	<0.3	<1.5	-	<1	-	-	-	-	-	U09141A
○	G 30.94+0.11	-	-	-	<1	-	<1	<1	-	-	<1	<1	-	<0.8	R09153A
○ ⊙	G 31.28+0.06	8 (1)	10 (0.3)	1.6 (0.4)	-	2.8 (0.4)	4 (1)	-	7 (1)	-	-	-	-	-	U09141A
	G 32.03+0.06	<0.8	<0.2	2.2 (0.4)	-	<0.4	<1	-	<1	-	-	-	-	-	U09141A
	G 32.11+0.09	-	-	-	<1	-	<1	<1	-	-	<1	<1	-	<1	R09153A
	G 32.97+0.04	-	-	-	<1	-	<1	<1	-	-	<1	<1	-	<1	R09153A
△	G 33.09−0.07	4.5 (0.5)	0.9 (0.2)	<0.3	-	<0.4	<1	-	<1	-	-	-	-	-	U09141A
○	G 33.40+0.01	-	-	-	<0.8	-	<0.8	<1	-	-	<0.8	<0.8	-	<0.5	R09153A

†: Error of the calibrated fluxes could be larger than 10 %, especially U08299B.
‡: There is a possibility of splias.
★: Target sources of phase reference observations.
○: Reference sources were detected with a detection limit of 5σ.
◎: Fringe detected (or expected to be detected) with the baseline length more than 1,000 km and a detection limit of 5σ at only VERA baselines.
⊙: Fringe detected (or expected to be detected) with the baseline length more than 1,000 km and a detection limit of 5σ at the baselines include Yamaguchi and/or Usuda.
△: Fringe detected (or expected to be detected) enough with the baseline length less than 1,000 km and a detection limit of 5σ.
-: Lack of baseline data since observation trouble or absent station.
(...) or <... : 1σ noise level.

Table 3.4: Results of Fringe Check Observation for QSOs 1.

No	Name	RY [Jy]	UY [Jy]	UR [Jy]	RS [Jy]	RO [Jy]	MR [Jy]	SY [Jy]	MO [Jy]	OS [Jy]	US [Jy]	MS [Jy]	Obs. Code
1	J1713−3226	-	-	-	-	0.8	0.8	-	0.8	-	-	-	R09162B
2	J1717−3948	-	-	-	-	×	×	-	×	-	-	-	R09162B
		-	-	-	×	×	×	-	×	×	-	×	R09155A
3	J1733−1304	-	-	-	2.0	2.0	2.0	-	2.0	2.0	-	2.0	R09155A
		-	-	-	-	2.0	2.0	-	2.0	-	-	-	R09162B
4	J1733−3722	-	-	-	-	0.8	0.8	-	0.8	-	-	-	R09162B
		-	○	-	-	-	-	○	-	-	○	-	U08299B†
5	J1736−3400	-	-	-	×	×	×	-	×	×	-	×	R09155A
		-	-	-	-	×	×	-	×	-	-	-	R09162B
6	J1743−3058	-	-	-	×	×	×	-	×	×	-	×	R09155A
		-	-	-	-	×	×	-	×	-	-	-	R09162B
7	J1744−3116	-	-	-	-	×	×	-	×	-	-	-	R09162B
		-	-	-	×	×	×	-	×	×	-	×	R09155A
8	J1745−2820	-	-	-	×	×	×	-	×	×	-	×	R09155A
		-	-	-	-	×	×	-	×	-	-	-	R09162B
9	J1745−2900	△	×	×	×	-	-	×	-	-	×	-	U08299B†
10	J1752−2956	-	-	-	×	×	×	-	×	×	-	×	R09155A
		-	-	-	-	×	×	-	×	-	-	-	R09162B
11	J1755−2232	-	-	-	0.4	0.4	0.4	-	0.4	0.4	-	0.4	R09155A
		-	-	-	-	0.4	0.4	-	0.4	-	-	-	R09162B
12	J1756−2807	-	-	-	×	×	×	-	×	×	-	×	R09155A
		-	-	-	-	×	×	-	×	-	-	-	R09162B
13	J1808−2124	-	-	-	-	×	×	-	×	-	-	-	R09162B
		×	×	×	×	-	-	×	-	-	×	-	U08299B†
14	J1818−1108	○	○	○	×	-	-	×	-	-	×	-	U08299B†
		-	-	-	-	×	×	-	×	-	-	-	R09162B
15	J1819−2036	-	-	-	-	×	×	-	×	-	-	-	R09162B

†: Error of the cross collirated fluxes could be larger than 10 %, especially U08299B.
○: Detected with enough flux as phase reference source.
△: Detected without enough flux as phase reference source.
×: Not detected.
-: No data.

Table 3.4: Results of Fringe Check Observation for QSOs 2.

No	Name	RY [Jy]	UY [Jy]	UR [Jy]	RS [Jy]	RO [Jy]	MR [Jy]	SY [Jy]	MO [Jy]	OS [Jy]	US [Jy]	MS [Jy]	Obs. Code
16	J1824+0119	△	○	○	△	-	-	○	-	-	○	-	U08299B†
17	J1825−0737	-	-	-	-	0.4	0.4	-	0.4	-	-	-	R09162B
		○	○	○	△	-	-	○	-	-	○	-	U08299B†
18	J1825−1718	-	-	-	0.4	0.4	0.4	-	0.4	0.4	-	0.4	R09155A
		△	×	×	△	-	-	○	-	-	△	-	U08299B†
		-	-	-	-	0.4	0.4	-	0.4	-	-	-	R09162B
19	J1828−0530	-	-	-	×	×	∼0.3	-	×	×	-	×	R09155A
		-	-	-	-	×	∼0.3	-	×	-	-	-	R09162B
20	J1832−1035	-	-	-	×	×	×	-	×	×	-	×	R09155A
		-	-	-	-	×	∼0.3	-	×	-	-	-	R09162B
21	J1834−0301	-	-	-	0.4	0.4	0.4	-	0.4	0.4	-	0.4	R09153A
		-	-	-	-	0.4	0.4	-	0.4	-	-	-	R09162B
22	J1835−1115	-	-	-	×	×	×	-	×	×	-	×	R09155A
		-	-	-	-	×	×	-	×	-	-	-	R09162B
23	J1838+0927	-	-	-	×	×	×	-	×	×	-	×	R09161A
		-	-	-	×	×	×	-	×	×	-	×	R09155A
		-	-	-	-	×	×	-	×	-	-	-	R09162B
		-	-	-	×	×	×	-	×	×	-	×	R09153A
24	J1844+0137	-	-	-	×	×	×	-	×	×	-	×	R09155A
		-	-	-	-	×	×	-	×	-	-	-	R09162B
25	J1846−0003	-	-	-	-	×	×	-	×	-	-	-	R09162B
26	J1846−0651	-	-	-	×	×	×	-	×	×	-	×	R09155A
		-	-	-	-	×	∼0.3	-	×	-	-	-	R09162B
		×	○	×	×	-	-	×	-	-	○	-	U08299B†
27	J1855+0251	-	-	-	×	×	×	-	×	×	-	×	R09153A
28	J1907+0127	-	-	-	0.4	0.4	0.4	-	0.4	0.4	-	0.4	R09153A

†: Error of the cross collirated fluxes could be larger than 10 %, especially U08299B.
○: Detected with enough flux as phase reference source.
△: Detected without enough flux as phase reference source.
×: Not detected.
-: No data.

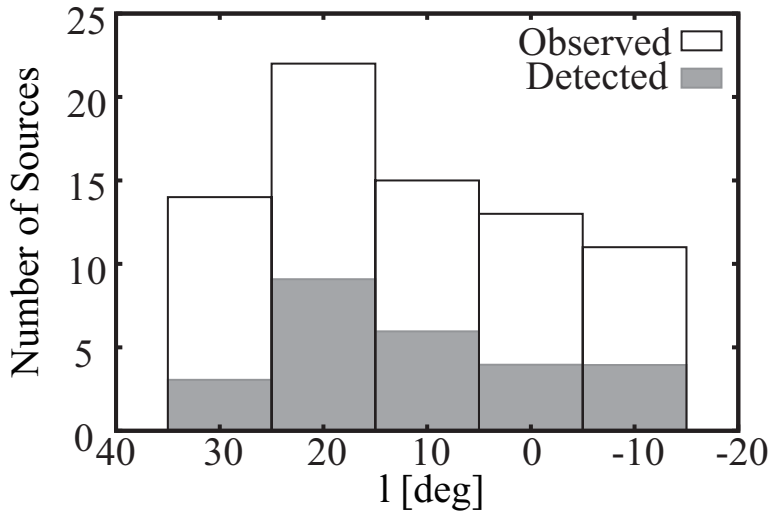

Figure 3.2: Number of 6.7 GHz methanol maser sources as function of galactic longitude in fringe check observation with the VERA/JVN. The shaded and blanked bars represent detected with signal to noise ratio of more than 5σ at $\sim$1,000 km or longer baseline and observed sources, respectively.

Chapter 4

The Molecular Gas Motion with the Bar Structure of the Milky Way Galaxy

4.1 Introduction

Our purpose of this study is to obtain full 3-D motions of maser sources simultaneously, and study kinematic motions of methanol molecular gas around the Galactic bar. In chapter 2, we have evaluated the phase-referencing astrometry of 6.7 GHz methanol maser sources with the VERA/JVN.

In this chapter, we present astrometric observations of ten 6.7 GHz methanol maser sources, which were selected by the fringe-check observation in chapter 3. These sources are expected to locate around the Galactic bar having $|l| < 40^\circ$ and kinematic distances from the Galactic center less than 5 kpc.

4.2 Observations

The ten 6.7 GHz methanol maser sources and their phase-reference sources were observed with the VERA. These ten sources were selected based on the fringe check

observations in chapter 3. These sources are located $|l| < 40°$, and their position reference sources were also detected in the fringe check observations. Observations were done in a period between November 2009 and September 2010 for 2 - 4 epochs in each sources. Radio frequency of 6.668518 GHz is adopted in this paper as the rest frequency of $CH_3OH\,5_1 \rightarrow 6_0A^+$ transition, and left-hand circular polarization was received at all antennas. For details of these observations, see table 4.1. In our astrometry observations, we conducted one-beam switching observations for phase-referencing. Therefore maser sources and a phase-reference sources were alternately observed with a four-minute cycle (typically 1.75 minute on-source integration times for a maser source and a phase-reference source, respectively, and the rest for slewing). 3C 345 was also observed once or twice for 10 minutes in the each observation as a calibrator and fringe finder. NRAO 530 or J1824+0119 were also observed for 5 minutes every one hour as bandpass calibrators. G 9.62+0.19 was also observed once one hour for system check and amplitude calibration. On the other hand, at the observations in 2009, G 9.62+0.19 were only observed for 3 minute at the beginning of schedules as a system check source, because amplitude calibration data were scheduled to obtain R-SKY data at all antennas in the observations in 2009. However, the all VERA antennas except Mizusawa station had R-SKY system failure, and this 3 minute scan of G 9.62+0.19 was also used for amplitude calibration. The received signals were filtered in 16 MHz bandwidth channels. Filtered signals were recorded with SONY DIR2000 recorder at a rate of 1024 Mbit s^{-1}. The recorded signals were correlated with the Mitaka FX correlator (Chikada et al. (1991)). Since the maser line is narrow, in the correlation process for the maser lines, we selected a small portion of bandwidth (8 MHz) centered at the maser lines to obtain high spectral resolutions. This produced auto-correlation and cross-correlation spectra consisting of 512 spectral channels with a frequency spacing 15.63 kHz ($\sim$ 0.72 km s^{-1}). On the other hand, for the reference sources, we set lower spectral resolutions of 32 or 64 channels per 16 MHz bandwidth, with total band width of 16 MHz $\times$ 14 bandwidth channels.

Table 4.1: Summary of astrometric observations and reductions.

Epoch	Date [yyyy/DOY]	Duration [UT]	Synthesized beam [mas, deg]	Ref. $V_{\rm LSR}^{\dagger}$ [km s^{-1}]	Peak Flux‡ [Jy beam^{-1}]	rms of image [Jy beam^{-1}]
G 353.4−0.36 (17h30m26.18651408s, −34d41'45.630") / J1733−3722 (17h33m15.19s, −37d22'32.39726", Sep: 2.95°)						
1	2009/327	01:15 - 06:31	8.86×2.72, −21.2	−20.2	1.86	0.36
2	2010/038	20:10 - 01:12	8.68×2.77, −19.7	−20.2	2.15	0.34
3	2010/136	13:45 - 18:47	8.74×2.74, −19.3	−20.2	3.84	0.47
G 351.41+0.64 (17h20m53.3742934s, −35d47'01.48353") / J1733−3722 (17h33m15.19s, −37d22'32.39726", Sep: 2.74°)						
1	2010/023	21:10 - 02:12	8.05×2.66, −17.9	−10.0	9.86	1.53
2	2010/102	16:00 - 21:02	8.53×2.70, −17.9	−10.0	10.06	1.34
3	2010/235	07:15 - 12:17	8.68×2.80, −16.9	−10.0	6.60	1.35
4	2010/306	02:35 - 07:37	8.66×2.79, −15.7	−10.0	7.60	1.59
G 25.70−0.04 (18h38m3.1413472s, −6d24'15.53385") / J1834−0301 (18h34m14.074558, −3d01'19.62740", Sep: 3.51°)						
1	2010/025	20:00 - 05:14	7.68×5.57, −31.0	95.3	7.76	1.04
2	2010/099	15:10 - 00:24	9.44×4.43, −40.4	95.3	3.59	0.44
3	2010/236	06:15 - 15:29	8.60×5.34, −39.8	95.3	-	1.93
4	2010/317	00:55 - 10:09	8.35×5.24, −44.1	95.3	6.22	0.97
G 28.14+0.00 (18h42m42.5898992s, −4d15'35.11517") / J1834−0301 (18h34m14.074558, −3d01'19.62740", Sep: 2.45°)						
1	2010/025	20:00 - 05:14	5.71×3.01, −37.1	101.0	3.07	0.11
2	2010/099	15:10 - 00:24	5.89×2.89, −36.8	101.0	2.12	0.09
3	2010/236	06:15 - 15:29	5.81×3.10, −37.0	101.0	3.00	0.22
4	2010/317	00:55 - 10:09	5.73×3.00, −37.3	101.0	2.53	0.16
G 9.98−0.02 (18h07m50.1156680s, −20d18'56.49403") / J1755−2232 (17h55m26.284784s, −22d32'10.61651", Sep: 3.64°)						
1	2009/339	00:25 - 07:35	7.12×3.30, −22.7	42.0	3.87	0.37
2	2010/039	19:25 - 04:39	6.83×3.73, −22.4	42.0	2.61	0.39
3	2010/129	14:15 - 21:25	Bad weather data	-	-	-

The coordinates of right ascension and declination are J2000.0 and these are phase center after recalculation for (u, v, w).
†: Line of sight velocity of a imaging channel.
‡: Result of imaging.

Table 4.1: Continue.

Epoch	Date [yyyy/DOY]	Duration [UT]	Synthesized beam [mas, deg]	Ref. $V_{\rm LSR}^{\dagger}$ [km s^{-1}]	Peak Flux‡ [Jy beam^{-1}]	rms of image [Jy beam^{-1}]
G 29.95−0.02 (18h46m03.7403894s, −2d39'22.31670") / J1834−0301 (18h34m14.074558s, −3d01'19.62740", Sep: 2.98°)						
1	2010/026	20:00 - 05:14	5.52×2.91, −36.0	95.5	8.58	0.45
2	2010/105	14:50 - 00:04	5.58×3.44, −38.2	95.5	7.44	0.58
3	2010/289	02:45 - 11:59	5.72×2.94, −38.8	95.5	2.97	0.34
G 30.76−0.05 (18h47m39.7257666s, −1d57'24.93898") / J1834−0301 (18h34m14.074558s, −3d01'19.62740", Sep: 3.52°)						
1	2010/026	20:00 - 05:14	5.63×2.92, −39.0	91.0	2.55	0.13
2	2010/105	14:50 - 00:04	5.60×3.37, −41.2	91.0	2.32	0.15
3	2010/289	02:45 - 11:59	5.71×2.92, −36.2	91.0	8.00	0.93
G 23.01−0.41 (18h34m40.2889383s, −9d00'38.16124") / J1825−0737 (18h25m37.609553s, −7d37'30.01266", Sep: 2.63°)						
1	2009/329	00:00 - 09:14	6.07×2.99, −33.6	75.0	10.96	0.84
2	2010/034	19:25 - 23:20	5.95×2.95, −32.2	75.0	7.28	0.66
3	2010/130	13:10 - 22:24	5.97×2.88, −33.1	75.0	10.80	0.87
4	2010/327	00:20 - 09:34	6.04×2.93, −33.2	75.0	10.91	0.91
G 24.78+0.08 (18h36m12.5620118s, −7d12'10.82626") / J1825−0737 (18h25m37.609553s, −7d37'30.01266", Sep: 2.66°)						
1	2009/329	00:00 - 09:14	6.14×2.89, −35.2	113.5	5.63	0.27
2	2010/034	19:25 - 23:20	5.77×2.98, −34.3	113.5	5.30	0.28
3	2010/130	13:10 - 22:24	5.94×2.92, −34.3	113.5	5.93	0.39
4	2010/327	00:20 - 09:34	6.04×2.93, −33.2	113.5	5.59	0.35
G 25.65+1.04 (18h34m20.9021583s, −5d59'42.16268") / J1825−0737 (18h25m37.609553s, −7d37'30.01266", Sep: 2.71°)						
1	2009/333	00:50 - 08:00	6.68×2.67, −35.5	41.9	5.77	0.22
2	2010/061*	18:40 - 01:50	5.73×2.85, −31.5	41.9	2.40	0.068
3	2010/131	14:05 - 21:15	5.78×2.89, −29.4	41.9	9.73	0.44
4	2010/248	06:25 - 13:35	5.74×2.82, −31.6	41.9	4.12	0.06

The coordinates of right ascension and declination are J2000.0 and these are phase center after after recalculation for (u, v, w).

$*$: 64 channels

†: Line of sight velocity of a imaging channel.

‡: Result of imaging.

4.3 Data Analysis

Data reductions were performed with the NRAO AIPS package basically in a standard manner. Delay and delay-rate offsets were calibrated using 3C 345. Bandpass responses were also calibrated using 3C 345 and NRAO 530. Amplitude calibrations were performed by the template method with total-power spectrum of G 9.62+0.19. Here, we obtained absolute flux of G 9.62+0.19 from an auto-correlation spectra of the Mizusawa station calibrated by system temperature estimated from R-SKY measurements. On the other hand, incase that we calibrated the data which have no G 9.62+0.19 scan at the Mizusawa station due to observational failure, the system temperature of the Mizusawa station was assumed to be common to other antennas, and this system temperature was applied to the scan of G 9.62+0.19. Fringe solutions of the reference sources were obtained with solution interval of two minutes. In self-calibrations for the reference sources, models of clean components were obtained by the DIFMAP software package provided by Caltech, to obtain faint components of the continuum emissions, if exist. However, each reference sources had no distinct structure throughout whole epochs. For the phase-referencing, the solutions of the reference sources obtained by self-calibration were applied to the data of the maser sources. Since the apriori delay model used in the correlator was not accurate enough for VLBI astrometry, we recalculated more precise delays and we corrected for the differences between them. The difference of path length was ~ 2 mm or less between our recalculated model and the CALC9 model developed by the NASA/GSFC VLBI group. In this correction, the visibility phase error caused by tropospheric delay were calibrated based on GPS measurements at each station (Honma et al. (2008)). Maser coordinates as phase center were also changed in this process to correct for the maser position offsets. The maser coordinates after the corrections are listed in table 4.1. The ionospheric delay was also calibrated based on the total vertical electron content (TEC) produced by JPL. At the re-calculation of the apriori delay model, the coordinates of the maser sources at the phase center was also changed to be nearly the coordinates of the brightest maser spots at the certain epoch. These coordinates were commonly used in all epochs at each sources. Thus, the brightest maser spots

in each maser sources were around the center of each maps. There synthesis imaging and de-convolutions were performed with the AIPS task IMAGR with uniform weighting. The maps with 2048 pix × 2048 pix were obtained with a pixel scale of 0.1 mas. Finally, the maser positions were derived by gaussian fitting using the AIPS task JMFIT for each maps.

4.4 Results

In our data reductions, we selected only one spot with the strongest flux density in each source to avoid misidentification of the spot between epochs. Table 4.2 shows time variations of relative positions of the maser spots to the phase center in each source. The coordinates of the phase center are listed in table 4.1. The position errs in table 4.2 are obtained by gaussian fitting using the AIPS task JMFIT. Signal-to-noise ratios are from 5 to 69, and beam sizes are about 6×3 mas^2 to 9×4 mas^2 (table 4.1 and 4.2). These statuses are listed in table 4.1. Peak fluxes of reference sources of J1733−3722, J1834−0301, J1755−2232, and J1825−0737 were about 180 mJy, 100 mJy, 150 mJy, and 300 mJy, respectively. A maser emission of G 25.70−0.04 was significantly resolved out, and fringes were only detected at baselines include IRIKI station. Thus, the beam size of G 25.70−0.04 is larger than the beam size of G 28.14+0.00 although these two sources were observed in same observations. In table 4.2, some outlier were excluded as follows. The data points make too large deviation with too large motion such as more than ∼200 km s^{-1}, which is corresponding to ∼10 mas yr^{-1} at distance of 5 kpc and expected from H I gas, and these data points can regard outlier. Outlier in the data of G 353.4−0.36 and G 351.41+0.64 had low signal-to-noise ratio below 6. The value of 6 in signal-to-noise ratio is near the lowest criterion value of certain maser image. Other outlier also had relatively lower signal-to-noise ratio than other epochs. These outlier are attributed to the fact of miss identification of the spot or calibration failure or simply weak maser flux to the observational noises.

We fitted linear proper motions with least-square fitting for right ascension and

declination with the data described in table 4.2. The fitting results are shown in table 4.3 and figure 4.1. In this fitting, we did not add a parameter of annual parallax in the least-square fitting because lack of epoch number. As fitting weights we used the error of JMFIT in table 4.2. We could see some deviation to the fitting results in the figure 4.1. The amplitudes of the deviation are within $\sim$1 mas.

After the least-square fittings, we transformed the coordinates from the equatorial coordinate system to the galactic coordinate system using following equation,

$$\begin{pmatrix} \mu_l \cos b \\ \mu_b \end{pmatrix} = \begin{pmatrix} -\sin l & \cos l & 0 \\ -\cos l \sin b & -\sin l \sin b & \cos b \end{pmatrix} G \begin{pmatrix} -\sin\alpha & \cos\alpha \sin\delta \\ \cos\alpha & -\sin\alpha \sin\delta \\ 0 & \cos\delta \end{pmatrix} \begin{pmatrix} \mu_\alpha \cos\delta \\ \mu_\delta \end{pmatrix}, \tag{4.1}$$

where the conversion matrix of G is

$$G = \begin{pmatrix} -0.054875539 & -0.873437105 & -0.483834992 \\ 0.494109454 & -0.444829594 & 0.746982249 \\ -0.867666136 & -0.198076390 & 0.455983795 \end{pmatrix}. \tag{4.2}$$

The proper motions for nine sources after coordinate transformation are listed in table 4.4. The linear proper motions are smaller than 10 mas yr^{-1} and negative motions to the galactic longitude.

4.5 Discussion

For the following discussion, we selected some sources with $V_{\rm LSR} > 50$ km s^{-1} in our data. This is because that most of sources with high radial velocities are expected to be located around tips of the Galactic bar and these high radial velocities are consisted with the most part of our samples at the galactic longitude of 20° - 30°, and here we focus on this region in the following discussions (c.f., figure 4.2). To discuss with more samples, the previous astrometry data are also used to increase sample (table 4.5). The referred sources are G 23.65−0.127 (Bartkiewicz et al. (2008)), G 23.01−0.41

Table 4.2: Relative maser spot positions from phase center in absolute coordinates.

Source Name	Year	DOY (offset) [day]	SNR†	$d\alpha \cos\delta$ [mas]	$d\delta$ [mas]
G 351.41+0.64	2010	23 (0)	6.4	-0.129 ± 0.277	0.537 ± 0.686
	2010	102 (79)	7.5	0.888 ± 0.205	-0.918 ± 0.385
G 25.70−0.04	2010	25 (0)	7.5	1.286 ± 0.579	-0.639 ± 0.513
	2010	99 (74)	8.2	1.593 ± 0.458	-1.566 ± 0.427
G 28.14+0.00	2010	25 (0)	27.9	0.786 ± 0.072	0.367 ± 0.087
	2010	99 (74)	23.6	0.012 ± 0.082	-0.188 ± 0.096
	2010	236 (211)	13.6	-1.189 ± 0.163	-2.202 ± 0.203
	2010	317 (292)	15.7	-1.427 ± 0.107	-3.971 ± 0.122
G 9.98−0.02	2009	339 (0)	10.5	0.269 ± 0.177	1.283 ± 0.285
	2010	39 (65)	6.7	0.425 ± 0.325	-0.279 ± 0.482
G 29.95−0.02	2010	26 (0)	19.1	-0.260 ± 0.105	-0.006 ± 0.096
	2010	105 (79)	12.8	-0.048 ± 0.220	-0.983 ± 0.178
G 30.76−0.05	2010	26 (0)	19.6	-0.017 ± 0.102	-0.258 ± 0.100
	2010	105 (79)	15.5	0.074 ± 0.138	-1.376 ± 0.121
	2010	289 (263)	8.6	-1.058 ± 0.252	-3.057 ± 0.226
G 23.01−0.41	2009	329 (0)	13.0	0.217 ± 0.129	1.820 ± 0.245
	2010	130 (166)	12.4	-0.120 ± 0.147	0.075 ± 0.294
	2010	327 (363)	12.1	-1.273 ± 0.127	-2.558 ± 0.268
G 24.78+0.08	2009	329 (0)	20.9	0.355 ± 0.094	2.798 ± 0.104
	2010	34 (70)	18.9	0.897 ± 0.117	1.126 ± 0.134
	2010	130 (166)	15.2	-0.009 ± 0.103	0.108 ± 0.111
	2010	327 (363)	16.2	-1.225 ± 0.104	-2.226 ± 0.129
G 25.65+1.04	2009	333 (0)	26.2	-0.647 ± 0.091	0.560 ± 0.105
	2010	61 (93)	35.3	0.738 ± 0.060	-0.417 ± 0.066
	2010	131 (163)	22.1	1.014 ± 0.091	-0.736 ± 0.108
	2010	248 (280)	68.7	0.444 ± 0.024	-1.791 ± 0.032

†: Signal-to-noise ratio of maser image.

Table 4.3: Relative maser spot motions from absolute spots positions.

Source	Data	μ_{RA} [mas yr^{-1}]	$\mu_{\mathrm{RA_{err}}}$ [mas yr^{-1}]	$\mu_{\mathrm{RA_{err}}}$ [%]	μ_{dec} [mas yr^{-1}]	$\mu_{\mathrm{dec_{err}}}$ [mas yr^{-1}]	$\mu_{\mathrm{dec_{err}}}$ [%]
G 351.41+0.64	epoch 1, 2	4.70	-	-	−6.72	-	-
G 25.70−0.04	epoch 1, 2	1.51	-	-	−4.57	-	-
G 28.14+0.00	epoch 1 - 4	−2.84	0.35	12	−5.43	0.63	12
G 9.98−0.02	epoch 1, 2	0.88	-	-	−8.77	-	-
G 29.95−0.02	epoch 1, 2	0.98	-	-	−4.51	-	-
G 30.76−0.05	epoch 1 - 3	−1.59	0.61	36	−3.79	0.42	11
G 23.01−0.41	epoch 1, 3, 4	−1.52	0.40	26	−4.42	0.30	7
G 24.78+0.08	epoch 1 - 4	−1.89	0.62	33	−4.82	0.53	11
G 25.65+1.04	epoch 1 - 4	1.31	1.29	98	−2.98	0.24	8

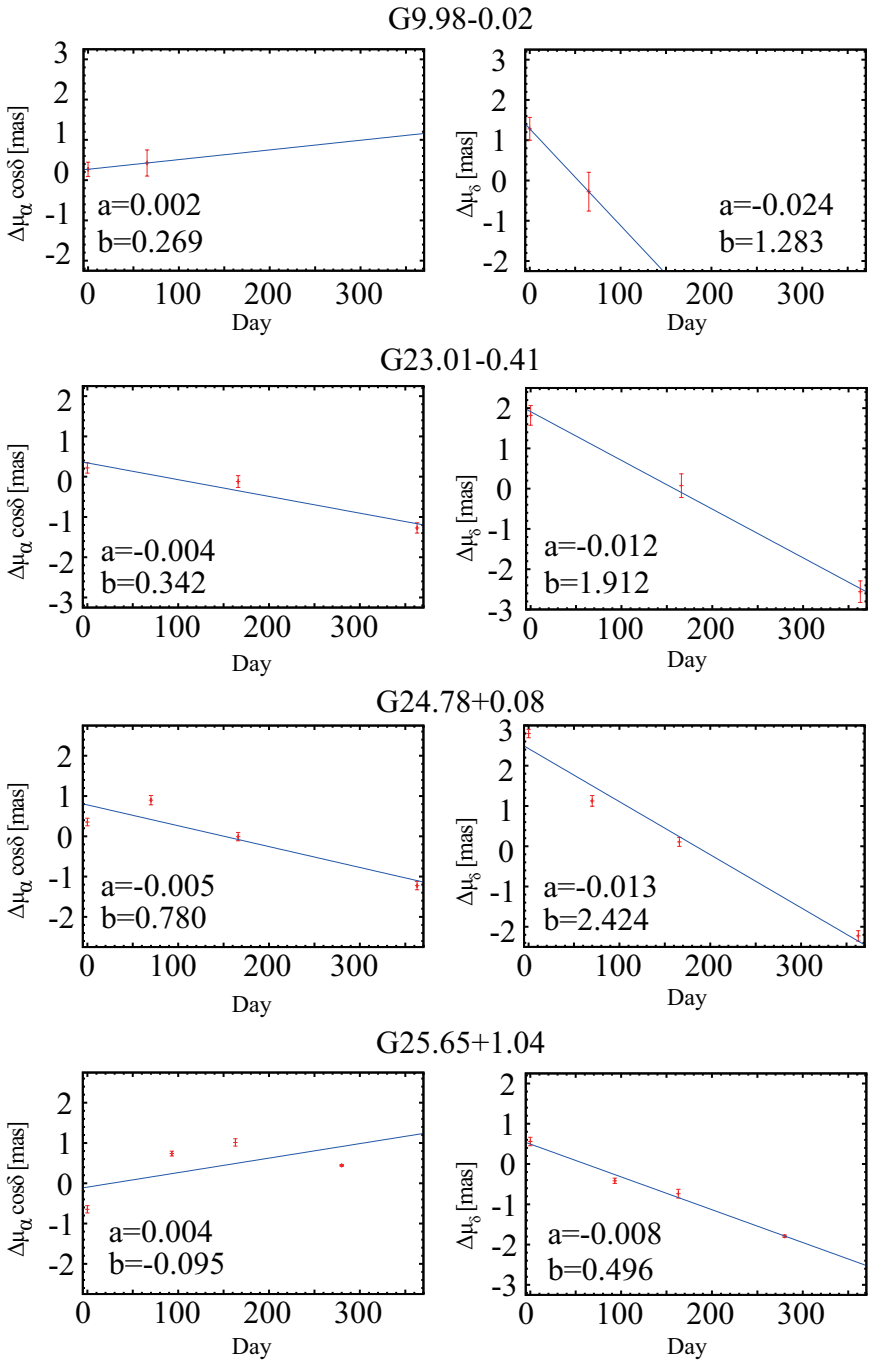

Figure 4.1: The fitting results of linear proper motions.

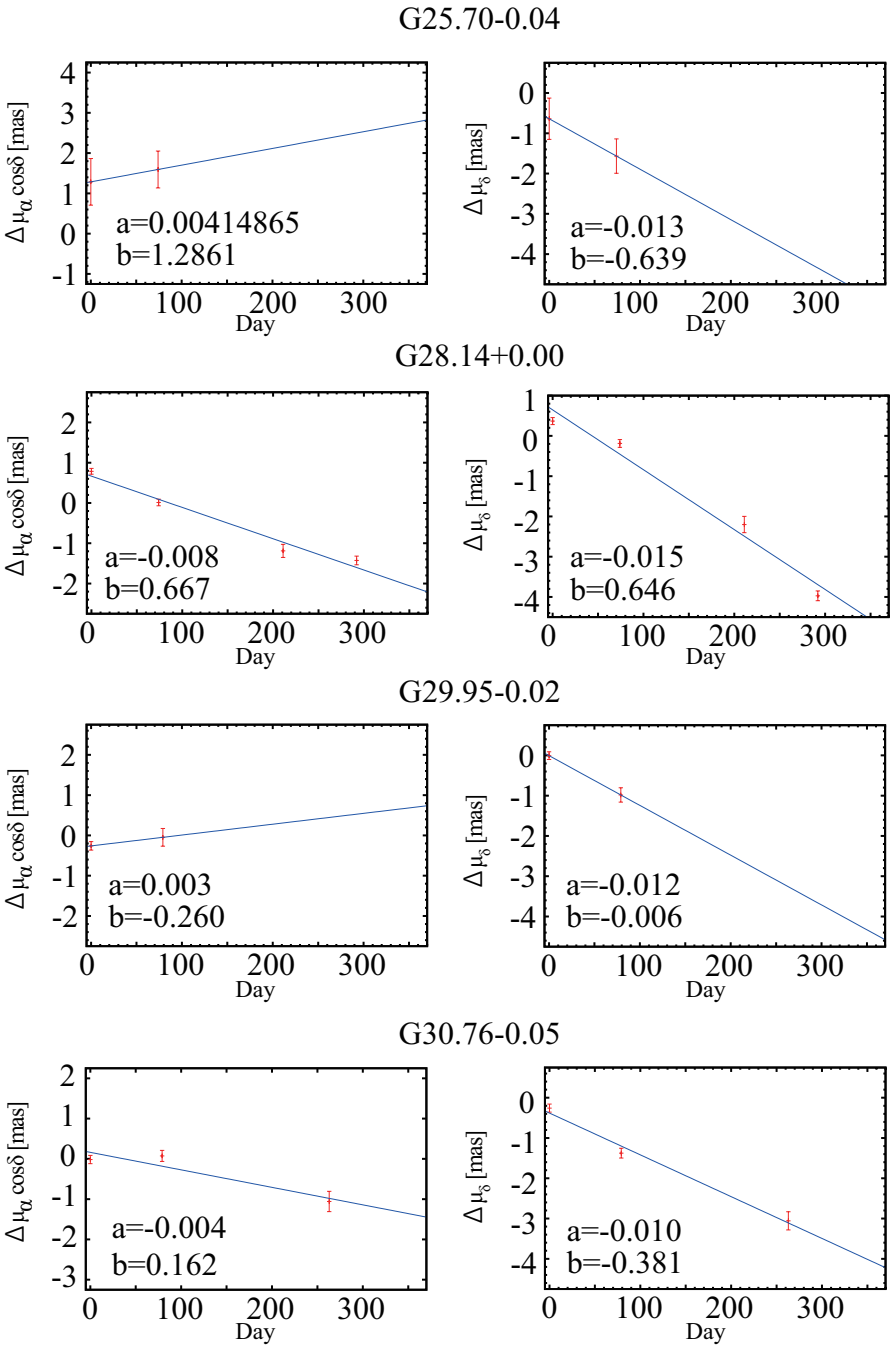

Figure 4.1: Continue

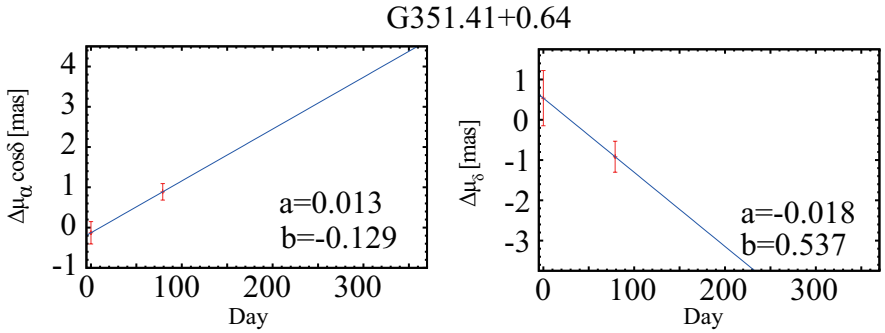

Figure 4.1: Continue

Table 4.4: Absolute proper motions in the galactic coordinate from the table 4.3.

	Source Name	$V_{\rm LSR}$ [km s^{-1}]	$\mu_l \cos b$ [mas yr^{-1}]	μ_b [mas yr^{-1}]
	G 351.41+0.64	−10±1.4	−2.84	−7.69
	G 9.98−0.02	42.0±1.4	−7.24	−5.03
○	G 30.76−0.05	91.0±1.4	-4.09 ± 0.66	-0.32 ± 0.35
○	G 25.70+0.04	95.3±1.4	−3.37	−3.44
○	G 28.14+0.00	101.0±1.4	-6.12 ± 0.72	0.04 ± 0.03
○	G 29.95−0.02	95.5±1.4	−3.56	−2.93
†	G 23.01−0.41	75.0±1.4	-4.62 ± 0.45	-0.69 ± 0.22
○	G 24.78+0.08	113.5±1.4	-5.14 ± 0.76	-0.53 ± 0.31
	G 25.65+1.04	41.9±1.4	-2.04 ± 0.81	-2.54 ± 1.03

○: $V_{\rm LSR} > 50$ km s^{-1} and selected sources for the discussions.

†: $V_{\rm LSR} > 50$ km s^{-1} and previous study also estimated proper motions.

and G 23.44−0.18 (Brunthaler et al. (2009)). Proper motions and parallax of this three sources were measured with 12 GHz methanol maser. There source are located in $|l| < 40^\circ$ with the distances from the Galactic center projected in the Galactic plane $R_{\rm GC} \lessapprox 5$ kpc, and $V_{\rm LSR} > 50$ km s^{-1}. G 23.01−0.41 was also observed in our 6.7 GHz observations, and values of the proper motion are consistent with the previous results of 12 GHz within the error. Here we adopted the 12 GHz data for G 23.01−0.41 because accuracy is better than our data. Thus finally we picked up eight data sets, five of which are from our results (G 24.78+0.08, G 25.70+0.04, G 28.14+0.00, G 29.95−0.02 and G 30.76−0.05) and three of which are from previous observations (G 23.65−0.127, G 23.01−0.41, G 23.44−0.18). The adopted sources and values are listed in table 4.6 and shown in figure 4.2 with a simulation model of Baba et al. (2010). The values of the proper motions are referred from the tables 4.4 and 4.5. For uncertainties of the proper motions, we suppose that a random motion of the molecular gas is 10 km s^{-1} from Reid et al. (2009a), which is corresponding to 0.4 mas yr^{-1} at the distance of 5 kpc. Thus, if the observational error is smaller than 0.4 mas yr^{-1}, we adopt this random motion as the uncertainties of the real proper motions due to the systematic motion in the Galaxy (i.e., the galactic rotation and/or streaming motion due to the Galactic bar). In opposite case, we adopt the observational error as the uncertainties of the real proper motion. For the estimated values with only two epochs, deviations of the proper motions were not estimated from the least-square fittings of the linear proper motions. On the other hand, a typical error is 0.7 mas yr^{-1} in our results with the data having more than two data points and the time span of ∼300 days. The time span of the two epochs data sets are ∼75 days which is four times smaller than the 300 days. Thus, we respected that the errors with two epochs data become quadruple of 0.7 mas yr^{-1}.

4.5.1 Flat Circular Rotation Model

As the first approach, we compared these VLBI data with a flat circular rotation model at the three dimensions of (l, $\mu_l \cos b$, $V_{\rm LSR}$). Equations about $V_{\rm LSR}$ [km s^{-1}]

Table 4.5: The distances and proper motions obtained by previous VLBI astrometry, which data sets are included in our discussions.

SourceName	Distance [kpc]	$V_{\rm LSR}$ [km s^{-1}]	$\mu_l \cos b$ [mas yr^{-1}]	μ_b [mas yr^{-1}]	Ref.
G 23.65−0.127	$3.19^{+0.46}_{-0.35}$	83±3	−3.24±0.04	−0.19±0.004	a
G 23.01−0.41	$4.59^{+0.38}_{-0.33}$	81±3	−4.45±0.28,	−0.37±0.10	b
G 23.44−0.18	$5.88^{+1.37}_{-0.93}$	97±3	−4.54±0.11	−0.18±0.06	b

a: Bartkiewicz et al. (2008)

b: Brunthaler et al. (2009)

Table 4.6: Adopted values for our discussion.

Source Name	$V_{\rm LSR}$ ($\sigma_{V_{\rm LSR}}$) [km s^{-1}]	$\mu_l \cos b$ ($\sigma_{\mu_l \cos b}$) [mas yr^{-1}]	Reference
G 30.76−0.05	91.0 (10.0)	−4.09 (0.66)	Our data
G 25.70+0.04	95.3 (10.0)	−3.37 (2.80)	Our data
G 28.14+0.00	101.0 (10.0)	−6.12 (0.72)	Our data
G 29.95−0.02	95.5 (10.0)	−3.56 (2.80)	Our data
G 24.78+0.08	113.5 (10.0)	−5.14 (0.76)	Our data
G 23.65−0.127	83.0 (10.0)	−3.24 (0.40)	Bartkiewicz et al. (2008)
G 23.01−0.41	81.0 (10.0)	−4.45 (0.40)	Brunthaler et al. (2009)
G 23.44−0.18	97.0 (10.0)	−4.54 (0.40)	Brunthaler et al. (2009)

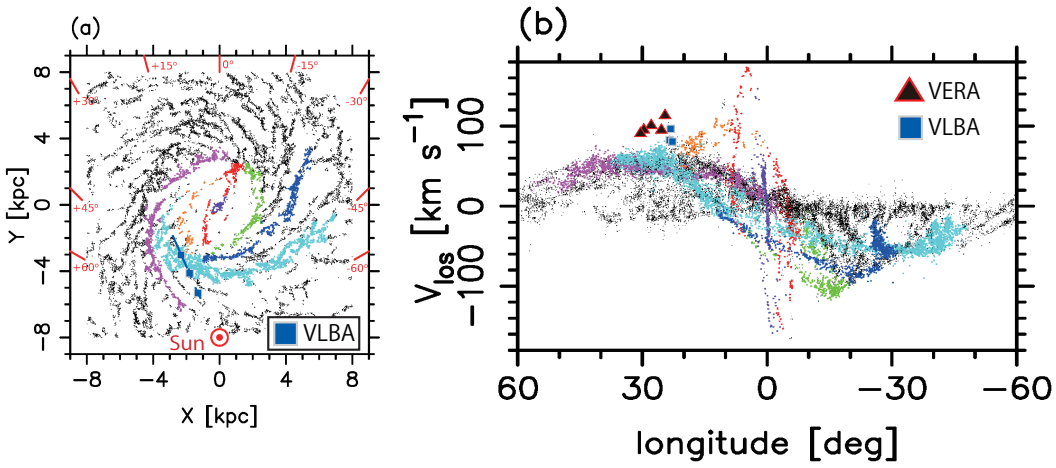

Figure 4.2: A X-Y plot and a l-v diagram of N-body simulation of Baba et al. (2010) with VLBI data in the table 4.6.

and $\mu_l \cos b$ [mas yr^{-1}] from flat rotation are as follow,

$$V_{\rm LSR} = \left(\frac{\Theta}{R} - \frac{\Theta_0}{R_0}\right) R_0 \sin l, \tag{4.3}$$

$$\mu_l \cos b = \frac{0.2108}{D}\left(\frac{\Theta}{R} - \frac{\Theta_0}{R_0}\right) R_0 \cos l - \frac{\Theta}{R}, \tag{4.4}$$

$$D = R_0 \cos l \pm \sqrt{R^2 - R_0^2 \sin^2 l}, \tag{4.5}$$

where l [deg] is galactic longitude, b [deg] is galactic latitude, D [kpc] is distance from the Sun, R [kpc] is radius from the Galactic center to any point, R_0 [kpc] is distance to the Galactic center from the Sun which is supposed to be 8.0 kpc, Θ [km s^{-1}] is rotational speed at any point, Θ_0 [km s^{-1}] is rotational speed of the local standard of the rest (LSR) of 220 km s^{-1}, 0.2108 is a conversion factor to the dimension of [mas yr^{-1}]. The second term of the equation 4.5 becomes positive value at out of heliocentric circle with the radius R_0 (see figure 4.3).

Figures 4.4 show the flat rotation at each longitude of the eight sources listed in table 4.6. The error bars of the systemic velocities in our data are ± 10 km s^{-1} supposed from a random motion of the Galactic molecular gas (Reid et al. 2009a).

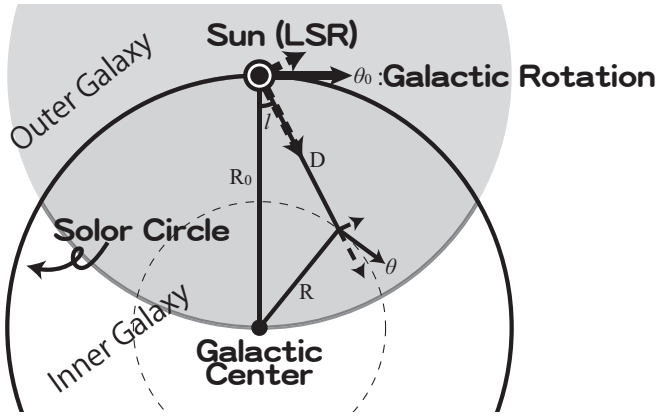

Figure 4.3: A graphical illustration of the flat circular rotation model.

As seen in figure 4.4, we found systematic deviation of $\mu_l \cos b$ from the flat rotation for some sources, with observed proper motions being always smaller than those expected from the flat rotation model. This trend becomes more prominent for the sources around the Galactic bar, such as G 23.01−0.41, G 23.44−0.18. These two sources show typically ∼0.5 - 1.0 mas yr^{-1} slower than other sources (1 mas yr at the distance of 5.0 kpc is corresponding to ∼24 km s^{-1}).

4.5.2 Non-flat Circular Rotation Model

In order to test if the observed radial velocities and proper motions can be explained without any non-circular motion, here we consider a non-flat rotation curve as follows,

$$\Theta(R) = \Theta_0 - \alpha(R_{\rm DP} - R) \qquad at\ (R \leq R_{\rm DP}), \tag{4.6}$$

$$\Theta(R) = \Theta_0 \qquad at\ (R > R_{\rm DP}), \tag{4.7}$$

where $\Theta(R)$ is rotational speed in the direction of the galactic rotation as a function of radius from the Galactic center R, Θ_0 is rotational speed at the Sun, α is speed gradient of the galactic rotation of $\Theta(R)$, $R_{\rm DP}$ is radius within which rotation velocity decreases linearly toward the Galactic center. Here we adopt $\Theta_0 = 220$ km s^{-1}. We substitute the equation 4.6 into the equation 4.3 and 4.4, and use these equations to the data of eight sources.

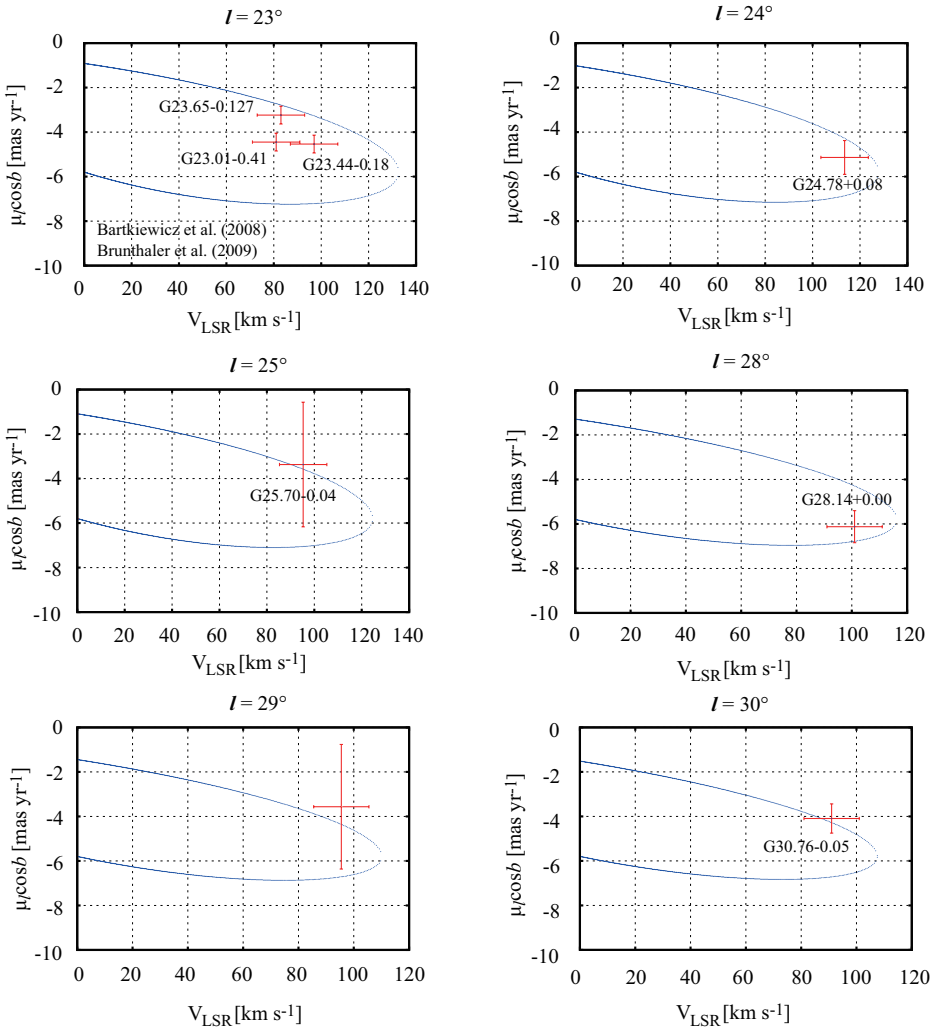

Figure 4.4: The flat rotation model on the ($V_{\rm LSR}$, $\mu_l \cos b$) plots at certain galactic latitudes and the results of the VLBI observations.

For purpose of estimation of best parameters, $R_{\rm DP}$ and α, we obtained reduced chi-square value (χ^2_ν) between above model and the VLBI data sets. The χ^2_ν is estimated by a following equation with each data point ($V_{{\rm LSR}j}$, $\mu_l \cos b_j$) and nearest model point ($V'_{{\rm LSR}j}$, $\mu'_l \cos b_j$).

$$\chi^2_\nu = \frac{1}{\nu} \sum_{j=1}^{N} \left[\frac{(V_{{\rm LSR}j} - V'_{{\rm LSR}j})^2}{\sigma^2_{V_{{\rm LSR}j}}} + \frac{(\mu_l \cos b_j - \mu'_l \cos b_j)^2}{\sigma^2_{\mu_l \cos bj}} \right], \tag{4.8}$$

where $\nu \equiv N - N_c$, N is number of data, N_c is degree of freedom, which is 2 in the present case. We searched minimum χ^2_ν with the VLBI data and the nearest model points between ranges of $1.0 \leq R_{\rm DP}[{\rm kpc}] \leq 6.5$ and $-10 \leq \alpha[{\rm kms}^{-1}] \leq 60$.

Fitting results are presented in figures 4.6 - 4.8. In the upper panel of figure 4.6, local minimums of the reduced chi-square values show some slope. In this trend, we picked up six parameter pairs of ($R_{\rm DP}$, α) with the smallest χ^2_ν, showing in bottom panel of figure 4.6. A value of χ^2_ν at flat rotation curve is also plotted in figure 4.6. The values of χ^2_ν is $\sim$0.5 at $\alpha = 9.5$ which is smaller than the $\chi^2_\nu \sim 2.7$ of the flat rotation by a factor of four, and supposed error of $\sigma_{V_{{\rm LSR}j}}$ and $\sigma_{\mu_l \cos bj}$ are also represent to acceptable value to this model. Using best parameters ($R_{\rm DP}$=5.5 kpc, $\alpha = 9.5$ km s^{-1} kpc^{-1}), we show ($V_{\rm LSR}$, $\mu_l \cos b$) plots in figure 4.7. The non-flat circular rotation model could be especially good for the proper motions of the sources at the galactic longitude around 23° than flat rotation in the figures 4.7. The radial velocities and proper motions of other sources are also reproduced by the best-model within their error bars. Therefore, as far as the eight sources in the present sample are considered, the non-flat circular rotation model can explain the observed radial velocities and proper motions.

On the other hand, we should test if the model can reproduce other properties of the galactic rotation, such as the H I longitude-velocity diagram. We also show the longitude-velocity map with H I map in figure 4.8 with rotation models considered here. The χ^2_ν is also estimated with comparing between the flat/non-flat circular rotation model and terminal velocities of H I, which are listed in table 4.7 and shown in figure 4.5. In these χ^2_ν estimations, we assumed that a typical uncertainty of the terminal velocity of H I is 10 km s^{-1} (McClure-Griffiths & Dickey (2007)). The χ^2_ν

for the flat rotation model is 10.4 and for the non-flat circular rotation model is 47.5. This value could be reflected that the rotational speed is about 20 km s^{-1} slower than flat rotation model at $l = 25°$ in figure 4.8. Thus, the non-flat circular rotation model can not reproduce the longitude-velocity map of H I map well.

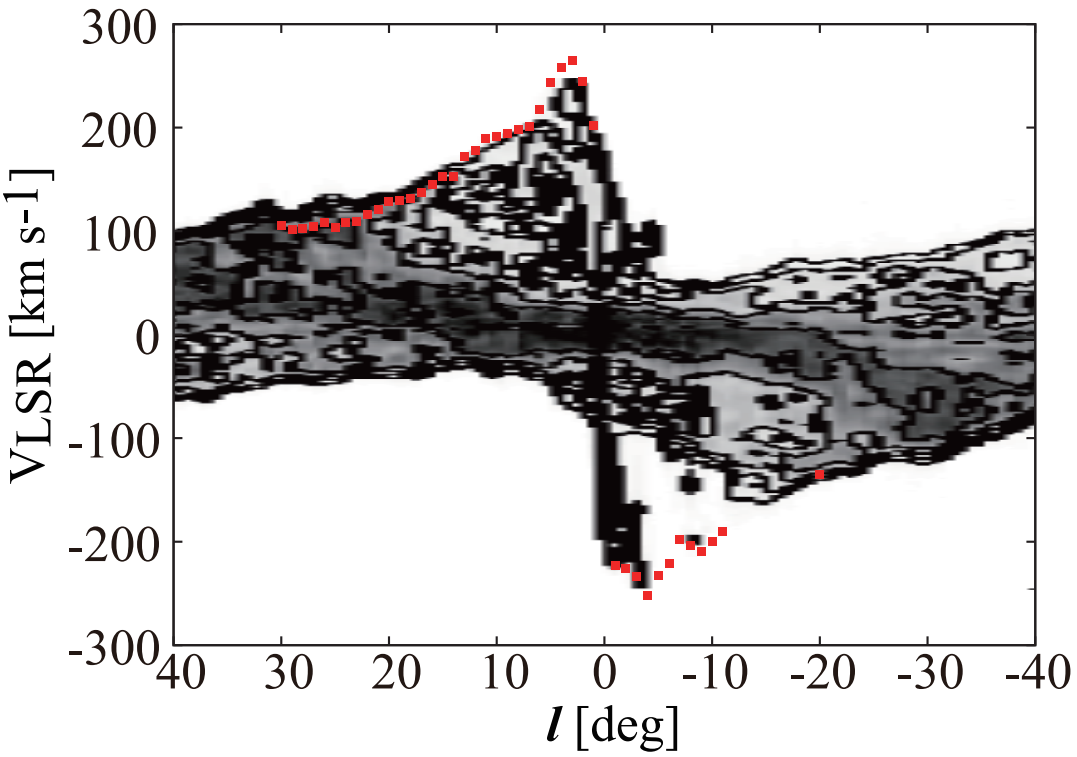

Figure 4.5: Terminal velocities in the table 4.7 and the l-v diagram of H I (Hartman & Burton (1997); Kerr et al. (1986); Burton & Listz (1983)).

In figure 4.8, we plotted tangential velocities for various rotation models. In these models, there is a cross point around the galactic longitude of 25°. This could be caused by that the VLBI data sets do not cover the all galactic longitude within 40° and only cover the range of 23° - 30°. Thus, any parameter sets naturally support this range of galactic longitude, $23° < l < 30°$. This trend is also shown in $R_{\rm DP}$ in upper panel of figure 4.6. Suitable $R_{\rm DP}$ could not appear below ∼4.0 kpc. From above results, it is more effective way to increase sample sources covering more wide range of galactic longitude.

Table 4.7: Terminal velocities of H I.

l [deg]	$V_{\rm term}$ [km s^{-1}]	Ref.	l [deg]	$V_{\rm term}$ [km s^{-1}	Ref.
40.0	77.8	a	9.0	194.5	c
39.0	85.5	a	8.0	198.5	c
38.0	87.3	a	7.0	201.5	c
37.0	85.4	a	6.0	218.0	c
36.0	88.0	a	5.0	244.0	c
35.0	96.1	a	4.0	258.5	c
34.0	99.8	a	3.0	265.0	c
33.0	102.0	a	2.0	245.0	c
32.0	106.5	a	1.0	202.5	c
31.0	111.5	a	−1.0	−222.5	c
30.0	105.8	a	−2.0	−226.0	c
29.0	101.9	a	−3.0	−233.5	c
28.0	102.3	a	−4.0	−252.0	c
27.0	104.5	a	−5.0	−232.5	c
26.0	107.9	a	−6.0	−221.0	c
25.0	103.9	a	−7.0	−197.5	c
24.0	107.9	a	−8.0	−204.0	c
23.0	109.4	a	−9.0	−209.5	c
22.0	115.7	a	−10.0	−200.0	c
21.0	121.2	a	−11.0	−190.0	c
20.0	129.0	b	−20.0	−135.5	d
19.0	130.0	b			
18.0	132.0	b			
17.0	137.0	b			
16.0	145.0	b			
15.0	153.0	b			
14.0	153.0	b			
13.0	172.0	c			
12.0	177.5	c			
11.0	189.5	c			
10.0	191.5	c			

a: Levine et al. (2008)
b: McClure-Griffiths et al. (2005)
c: Burton & Listz (1993)
d: McClure-Griffiths & Dickey (2007)

Therefore, as the figure 4.7, the circular rotation models could not be approximated to the VLBI data without slower rotation speed than Θ_0 of 220 km s^{-1}. However, such an rotation curve cannot explain the terminal velocities of the longitude-velocity map of H I gas as shown in figure 4.8. Thus it is difficult to explain both of 3-D motion and the l-v diagrams of H I without non-circular motion.

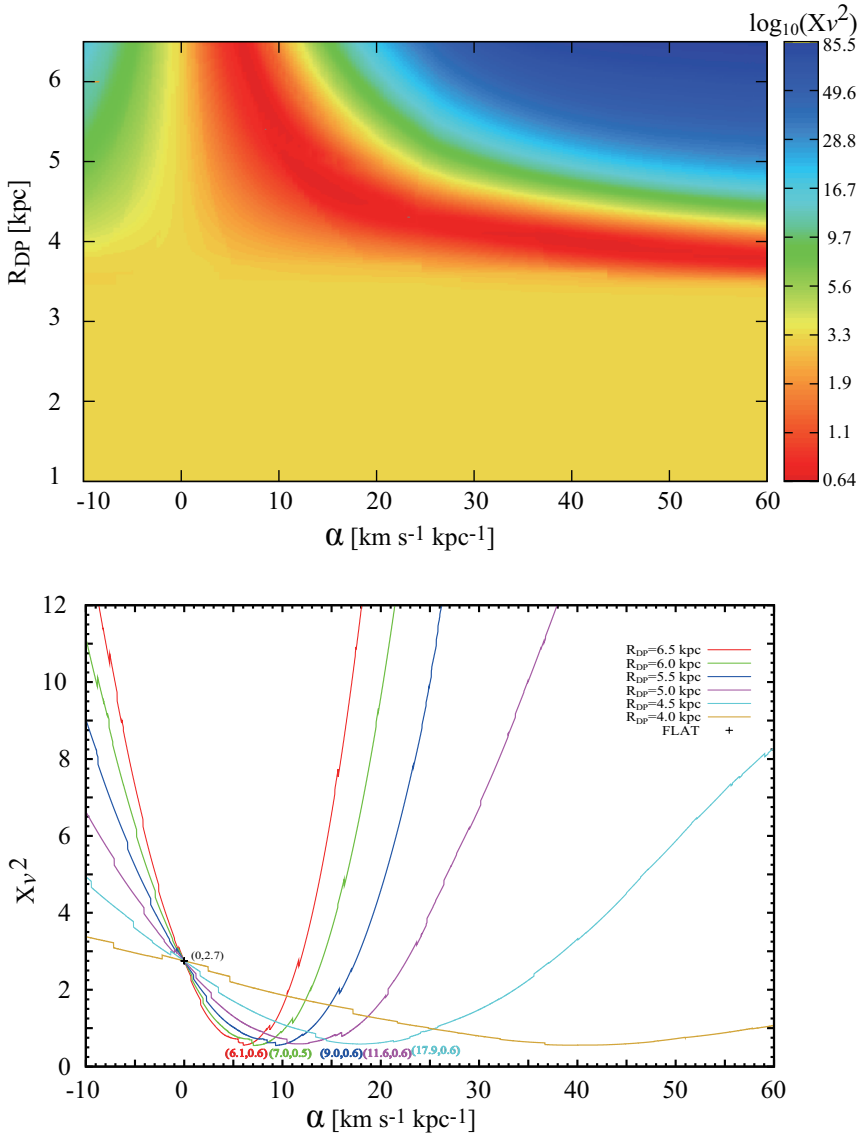

Figure 4.6: The fitting results of the non-flat circular rotation model. Marked coordinates are sample points with small χ^2_ν and at the flat rotation with $\Theta_0 = 220$ km s^{-1}.

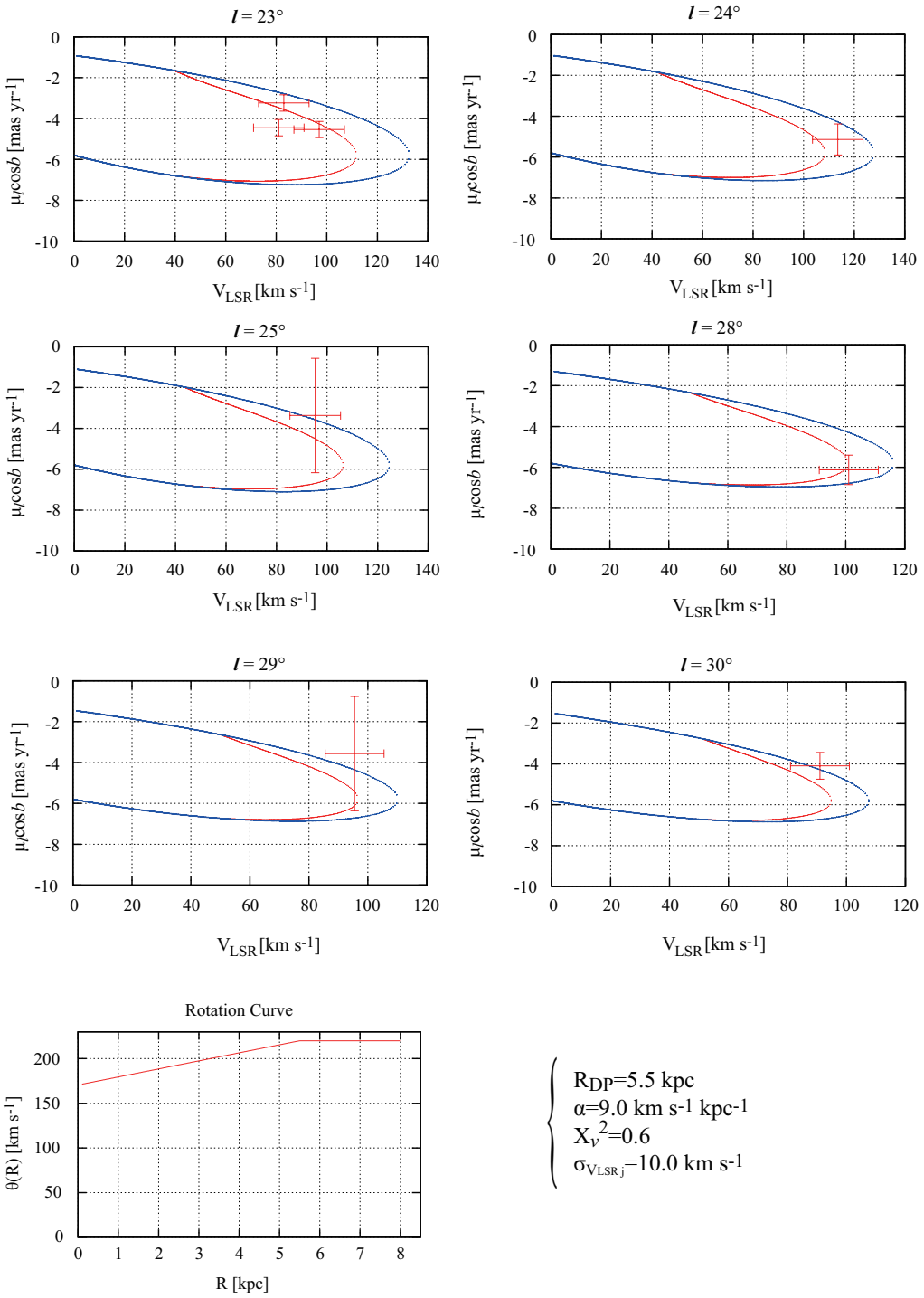

Figure 4.7: The fitting results of non-flat circular rotation model (red lines) with ($R_{DP} = 5.5$ kpc, $\alpha = 9.0$ km s^{-1} kpc^{-1}, R_0=8.0 kpc). Blue lines are the flat rotation model with $\Theta_0 = 220$ km s^{-1}.

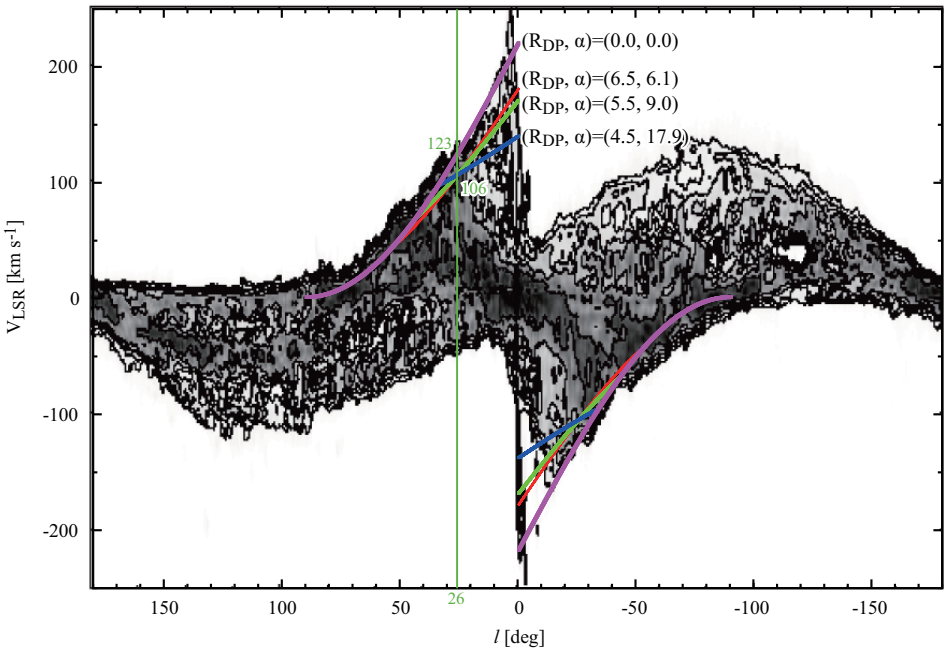

Figure 4.8: The fitting results of non-flat rotation model at the l-v map with H I (Hartman & Burton (1997), Kerr et al. (1986), Burton & Listz (1983)).

4.5.3 Damped Oval Orbit Model

Here we take another model including non-circular motion due to the Galactic bar to explain the observed radial velocities and the proper motions of our samples and the longitude-velocity diagram of H I. In this subsection, we use a damped oval orbit model with a weak bar potential, basically following Wada (1994), Sakamoto et al. (1999) and Binney & Tremaine (2008). The damped oval orbit model describes orbits of gas particles in the weak bar potential based on a linearized perturbation. Here, self gravitation of the gas particle is not considered, and an axisymmetric potential and an asymmetric bar potential are supposed. This model approximates the collisional nature of the gas by a damping term, which tend to force the gas motion back to circular rotation.

In the present study, we adopt a axisymmetric potential Φ_0 in polar coordinate (R, ϕ) as follows (Binney & Tremaine (2008)),

$$\Phi_0(R_{\rm g}) = \frac{1}{2} v_0^2 \ln(R_{\rm c}^2 + R_{\rm g}^2), \tag{4.9}$$

where $R_{\rm g}$ is radius of guiding center, $R_{\rm c}$ is core radius describing a dropping point on a rotation curve, v_0 is constant of a speed of the galactic circular rotation. Here we suppose that $R_c = 0.01 \ll 1$ and $v_0 = 220$ km s^{-1} to describe the flat rotation curve with Θ_0=220 km s^{-1}. Non-axisymmetric part of a potential $\Phi_{\rm b}$ (Wada (1994)) as follows,

$$\Phi_{\rm b}(R_{\rm g}) = -\epsilon \frac{{\rm a} R_{\rm g}^2}{(R_{\rm g}^2 + {\rm a}^2)^2}, \tag{4.10}$$

where ϵ is a constant value which represents strength of the bar potential, 'a' is an arbitrary constant, and supposed $a = 1$.

A equation of motion for the gas particle in the potential Φ at polar coordinate (R, ϕ) which rotate with a pattern speed of the bar Ω_b is as below,

$$\ddot{R} - R\dot{\phi}^2 = -\frac{\partial \Phi}{\partial R} + 2\Omega_b R\dot{\phi} + \Omega_b^2 R - 2\gamma \dot{R}, \tag{4.11}$$

$$R\ddot{\phi} + 2\dot{R}\dot{\phi} = -\frac{\partial \Phi}{R \partial \phi} - 2\Omega_b \dot{R}, \tag{4.12}$$

where γ is damping rate. From these linear simultaneous equations, solutions of the coordinate of the gas particle (R, ϕ) at each guiding center ($R_{\rm g}$, $\phi_{\rm g}$) at given time are derived as,

$$R = R_{\rm g} + A\cos\left[2(\Omega_0 - \Omega_{\rm b})t + \alpha\right] = R_{\rm g} + A\cos\left(2\phi_{\rm g} + \alpha\right), \tag{4.13}$$

$$\phi = (\Omega_0 - \Omega_{\rm b})t - \frac{B}{R_{\rm g}}\sin\left[2(\Omega_0 - \Omega_{\rm b})t + \beta\right] = \phi_{\rm g} - \frac{B}{R_{\rm g}}\sin\left(2\phi_{\rm g} + \beta\right), \tag{4.14}$$

where t is time and ϕ_g is $(\Omega_0 - \Omega_{\rm b})t$. Related equations also listed at the rest for the equation 4.13 and 4.14.

$$\Omega(R) \equiv \pm\sqrt{R^{-1}d\Phi_0/dR}, \tag{4.15}$$

and,

$$\Omega_0 \equiv \Omega(R_{\rm g}). \tag{4.16}$$

Then,

$$\Omega_0 = \frac{v_0}{\sqrt{R_{\rm c}^2 + R_{\rm g}^2}}, \tag{4.17}$$

$$\kappa_0 \equiv \sqrt{\left(\frac{d^2\Phi_0}{dR^2}\right)_{R_{\rm g}} + 3\Omega_0^2} = \frac{v_0\sqrt{4R_{\rm c}^2 + 2R_{\rm g}^2}}{R_{\rm c}^2 + R_{\rm g}^2}, \tag{4.18}$$

where κ_0 is an epicyclic frequency,

$$\lambda = \Lambda\kappa_0, \tag{4.19}$$

where λ is a damping rate and Λ is a constant value,

$$A \equiv -\frac{1}{\sqrt{\Delta^2 + 16\lambda^2(\Omega_0 - \Omega_{\rm b})^2}}\left[\left(\frac{d\Phi_{\rm b}}{dR}\right)_{R_{\rm g}} + \frac{2\Omega_0\Phi_{\rm b}(R_{\rm g})}{R_{\rm g}(\Omega_0 - \Omega_{\rm b})}\right], \tag{4.20}$$

and

$$A = \frac{2a\epsilon R_{\rm g}}{(R_{\rm g}^2 + {\rm a}^2)^2\sqrt{\Delta^2 + 16\lambda^2(\Omega_0 - \Omega_{\rm b})}} + \frac{4{\rm a}\epsilon R_{\rm g}^3}{(R_{\rm g}^2 + {\rm a}^2)^3 + \frac{2\Omega_0\Phi_{\rm b}}{R_{\rm g}(\Omega_0 - \Omega_{\rm b})}}, \tag{4.21}$$

$$\Delta = \kappa_0^2 - 4\left(\Omega_0 - \Omega_{\rm b}\right)^2, \tag{4.22}$$

$$\alpha = \arctan\left[\frac{-2\Lambda}{\kappa_0(\Omega_0 - \Omega_\mathrm{b})}\right], \tag{4.23}$$

$$B = \sqrt{(E+F)^2 + 2EF(\cos\alpha - 1)}, \tag{4.24}$$

$$E = \frac{\Omega_0}{\Omega_0 - \Omega_\mathrm{b}} A, \tag{4.25}$$

$$F = \frac{\Phi_\mathrm{b}(R_\mathrm{g})}{2R_\mathrm{g}(\Omega_0 - \Omega_\mathrm{b})^2}, \tag{4.26}$$

$$\beta = \arctan\left(\frac{\sin\alpha}{\cos\alpha + F/E}\right). \tag{4.27}$$

After (R, ϕ) is calculated, these are converted into the non-rotating galactic coordinate,

$$X = \mathrm{S}_1(R\cos\phi\cos\theta - R\sin\phi\sin\theta), \tag{4.28}$$

where S_1 is a scale factor for the length,

$$Y = \mathrm{S}_1(R\cos\phi\sin\theta + R\sin\phi\cos\theta). \tag{4.29}$$

Thus the distance of each gas particle from the Sun is calculated with the distance between the Sun and the Galactic center (R_0),

$$D = \sqrt{(R_0 + Y)^2 + X^2}, \tag{4.30}$$

where the R_0 is supposed to 8.0 kpc, and the galactic longitude is,

$$l = \arctan\left(\frac{X}{R_0 + Y}\right). \tag{4.31}$$

From equation 4.13 and 4.14, velocity in direction of R and ϕ are obtained,

$$V_R = \mathrm{S}_2[-2(\Omega_0 - \Omega_\mathrm{b})A\sin(2\phi_g + \alpha)], \tag{4.32}$$

$$V_\phi = \mathrm{S}_2\left\{(\Omega_0 - \Omega_\mathrm{b})[R_\mathrm{g} + A\cos(2\phi_{\mathrm{g}+\alpha}) - 2B\cos(2\phi_\mathrm{g} + \beta)]\right\}, \tag{4.33}$$

where S_2 is a scale factor for the velocity to convert to actual dimension of [km s^{-1}]. These velocities are also converted to the Cartesian coordinates and rotate the bar major axis around $\theta\,(=\theta'-90)$ degrees toward the Sun in the direction of the galactic longitude,

$$V_X = (V_R\cos\phi - V_\phi\sin\phi)\cos\theta' - (V_R\sin\phi + V_\phi\cos\phi)\sin\theta', \tag{4.34}$$

$$V_Y = (V_R\cos\phi - V_\phi\sin\phi)\sin\theta' + (V_R\sin\phi + V_\phi\cos\phi)\cos\theta'. \tag{4.35}$$

Finally, to obtain $V_{\rm LSR}$ [km s^{-1}] and μ_l [mas yr^{-1}], V_X and V_Y are convert to the galactic coordinate and subtracted the rotating speed of LSR (Θ_0),

$$V_{\rm LSR} = V_X\sin l + V_Y\cos l - \Theta_0\sin l, \tag{4.36}$$

$$\mu_l = \frac{0.2108}{D}(V_X\cos l - V_Y\sin l - \Theta_0\cos l), \tag{4.37}$$

where 0.2108 is a conversion factor to the dimension of [mas yr^{-1}]. Here the galactic latitude are supposed to be $b = 0$.

Properties of this model are shown in figure 4.9 and 4.10. In these figures, several orbits of the damped oval orbit model (green colored plots) and the flat rotation model (red colored plots), the reduced chi-squares of each parameter and the rotation curve are plotted. Unlike the damped oval orbit model, the flat rotation model is shown include around corotation area at (X, Y) plots and ($V_{\rm LSR}$, $\mu_l\cos b$) plots. Here we assumed that $v_0 = 0.71$ which is a dimensionless parameter. We also assumed that the $S_1 = 1.5$ and the $S_2 = 310$ which satisfy the l-v map of flat rotation.

To estimate the bar parameter of ($\Omega_{\rm b}$, ϵ, θ), we estimate two kind of the reduced chi-square value (χ^2_ν). One is the χ^2_ν between above model and the observational data sets in table 4.6. Another is the χ^2_ν between above model and the terminal velocities of H I in table 4.7. Here we do not discuss about unknown parameter of Λ, and suppose $\Lambda = 0.10$ (c.f., Sakamoto et al. (1999)). χ^2_ν are calculated between ranges of $0.1 < R_{\rm g} < 8.0$ and $-180^\circ < \phi_{\rm g} < 180^\circ$. When the amplitude of radial non-circular motion A in equation 4.21 becomes ∞ at the corotation radius, where

$(\Omega_0 - \Omega_b) = 0$, the model considered here (which is based on linearized equations of small perturbations) becomes invalid. Therefore,we reject around this point by upper threshold of $A = 0.37$ and lower threshold of $A = -0.37$ to include inner Lindblad resonance and reject around corotation in this model calculation.

The best fit parameter is ($\Omega_{\rm b}$, ϵ, θ) = (0.13, 0.10, 30°) in the least-square fitting, and shown in figure 4.9 and top panel of figure 4.11. The $\Omega_{\rm b}$ of 0.13 is corresponding to 26.8 km s^{-1} kpc^{-1}. Each value of χ^2_ν are 0.8 and 7.0 at ($V_{\rm LSR}$, $\mu_l \cos b$) plot and (l, $V_{\rm LSR}$) plot, respectively. However, in this parameters, the radius of corotation ($R_{\rm CR}$) become 8.2 kpc, which is out of the Sun from the Galactic center. Generally, $R_{\rm CR}$ should be located in the inner part between the Sun and the Galactic center. This is too large when comparing with the previous studies.

The pattern speed of the Galactic bar are expected to be $\sim$ 50 - 60 km s^{-1} kpc^{-1} (Debattista et al. (2002); Dehnen (2000); Minchev et al. (2007)). If we used the general value of $\Omega_{\rm b} \sim 55$ km s^{-1} kpc^{-1} corresponding to the $R_{\rm CR} \sim$ 3 - 4.6 kpc, the regions where can not hold linearization are located in our sample of data within $l \sim$ 20 - 30°. Thus, this model have limitations to discuss the motion with the typical galactic parameter of $\Omega_{\rm b}$ associate with $R_{\rm CR}$. Thus, in this discussion with this model, we use the larger $\Omega_{\rm b}$ of 0.24 (which is corresponding to 49.7 km s^{-1} kpc^{-1}) which is able to obtain smaller values of χ^2_ν. This value corresponds to a $R_{\rm CR}$ of 4.4 kpc. This $R_{\rm CR}$ value was consistent with the general values.

The results of comparison with the acceptable galactic parameters of ($\Omega_{\rm b}$, ϵ, θ) = (0.24, 0.10, 50°) are shown in figure 4.10 and bottom panel of figure 4.11. Values of χ^2_ν are 1.2 and 4.0 at ($V_{\rm LSR}$, $\mu_l \cos b$) plot and (l, $V_{\rm LSR}$) plot, respectively. From the plots of χ^2_ν, we can see that the reasonable value of the galactic parameter of $\theta \sim$ 30° - 50°. This value is consistent with the value of 10° - 50° obtained by completely other kind of observations at optical (e.g., Rattenbury et al. (2007a)).

From the value of $\Omega_{\rm b} = 0.24$ or 0.13 around extreme in the χ^2_ν plot of Ω_b for ($V_{\rm LSR}$, $\mu_l \cos b$) plot, this model suggest that peculiar motion between ILR and CR can explain the slower proper motions of VLBI data to the flat circular rotation. In figure 4.12 - 4.15, ($V_{\rm LSR}$, $\mu_l \cos b$) and (l, $V_{\rm LSR}$) diagrams and orbits on a (X, Y) plane

are shown every radius between each resonance. In these figures, a trend of slower proper motion to the flat circular rotation is remarkable tendency between ILR and CR, as shown in figure 4.14.

We show the summary of the values of χ^2_ν of each models in our discussions in table 4.8. The flat rotation model is able to reproduce the l-v map of the H I gas well. However, this model is not suitable to reproduce the ($V_{\rm LSR}$, $\mu_l \cos b$) plot with slower proper motions deviating from circular motions. On the other hand, the non-flat rotation model is opposite situation. Only the damped oval orbit model was able to explain the l-v map and the ($V_{\rm LSR}$, $\mu_l \cos b$) plot well.

Table 4.8: Summary of χ^2_ν of each model.

	χ^2_ν of ($V_{\rm LSR}$, $\mu_l \cos b$) with VLBI data		χ^2_ν of (l, $V_{\rm LSR}$) with H I data	
Flat rotation	2.7	○	10.4	○
Non-flat rotation	0.6	◎	47.5	×
Damped oval orbit	0.8 (best) / 1.2 ($\Omega_{\rm b,accept}$)	◎	7.0 (best) / 4.0($\Omega_{\rm b,accept}$)	◎

Therefore, introducing that the non-circular motion due to the Galactic bar is naturally explains the observed properties of maser proper motions as well as H I terminal velocities. In addition, our model calculations based on the damped orbit model predict that the suitable parameter of the bar inclination is 30° - 50°, which is most affected by systemic velocity at each galactic longitude in the VLBI data, and consistent with other studies. Thus, it is rather natural to conclude that the our maser proper motions are also tracing the non-circular motions of the bar, and they provide another evidence of the bar, which is based on the 3-D motions of the gas for the first time.

In the future, we would like to get more samples toward wider range of the galactic longitude and get a trend of whole motions around the Galactic bar. If we compare with VLBI data and any models, we can not see distinct difference between each model, because each data accuracy is limited by amplitude of random motion in the

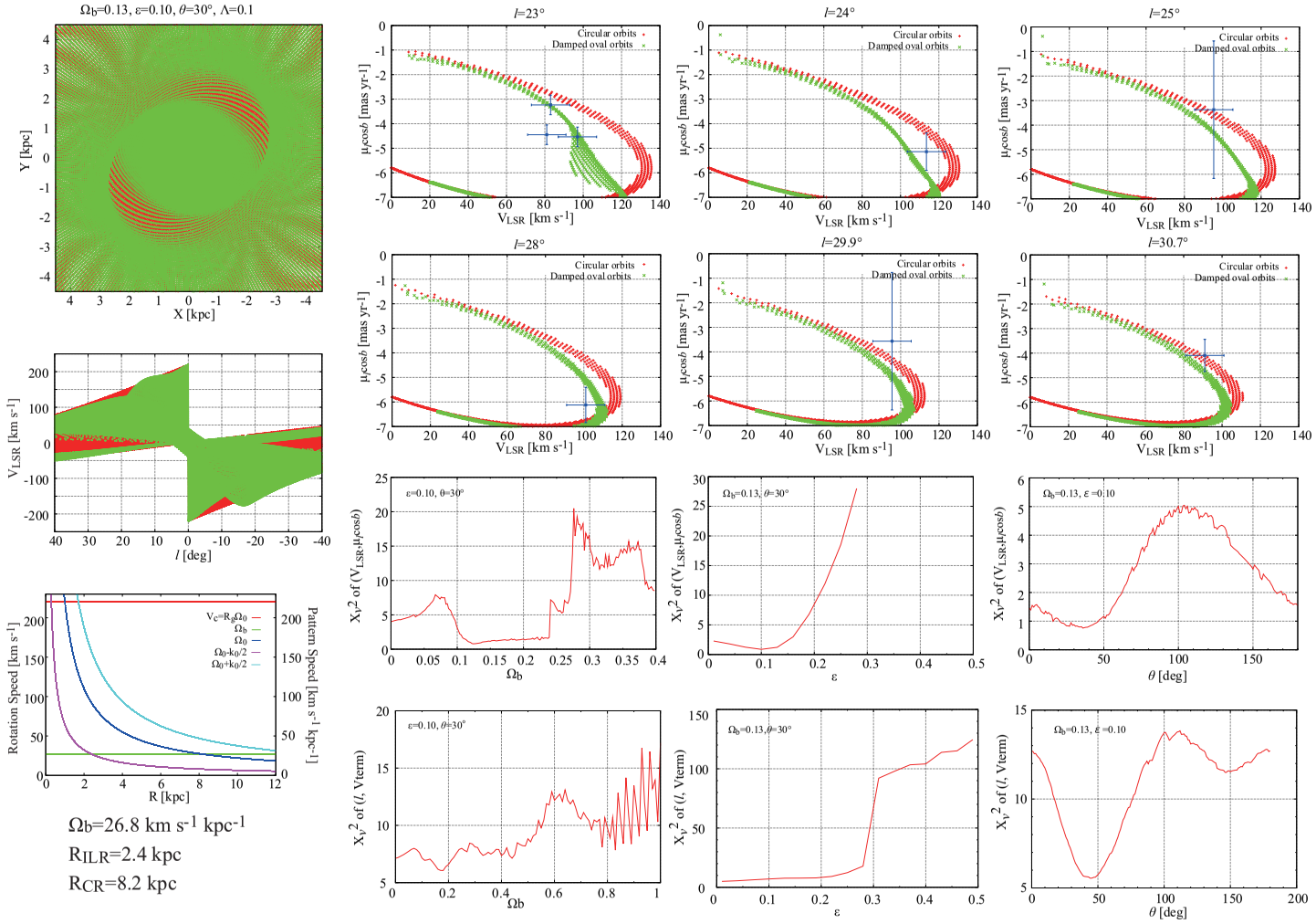

Figure 4.9: Fitting results of the damped oval orbit model with smallest chi-square value.

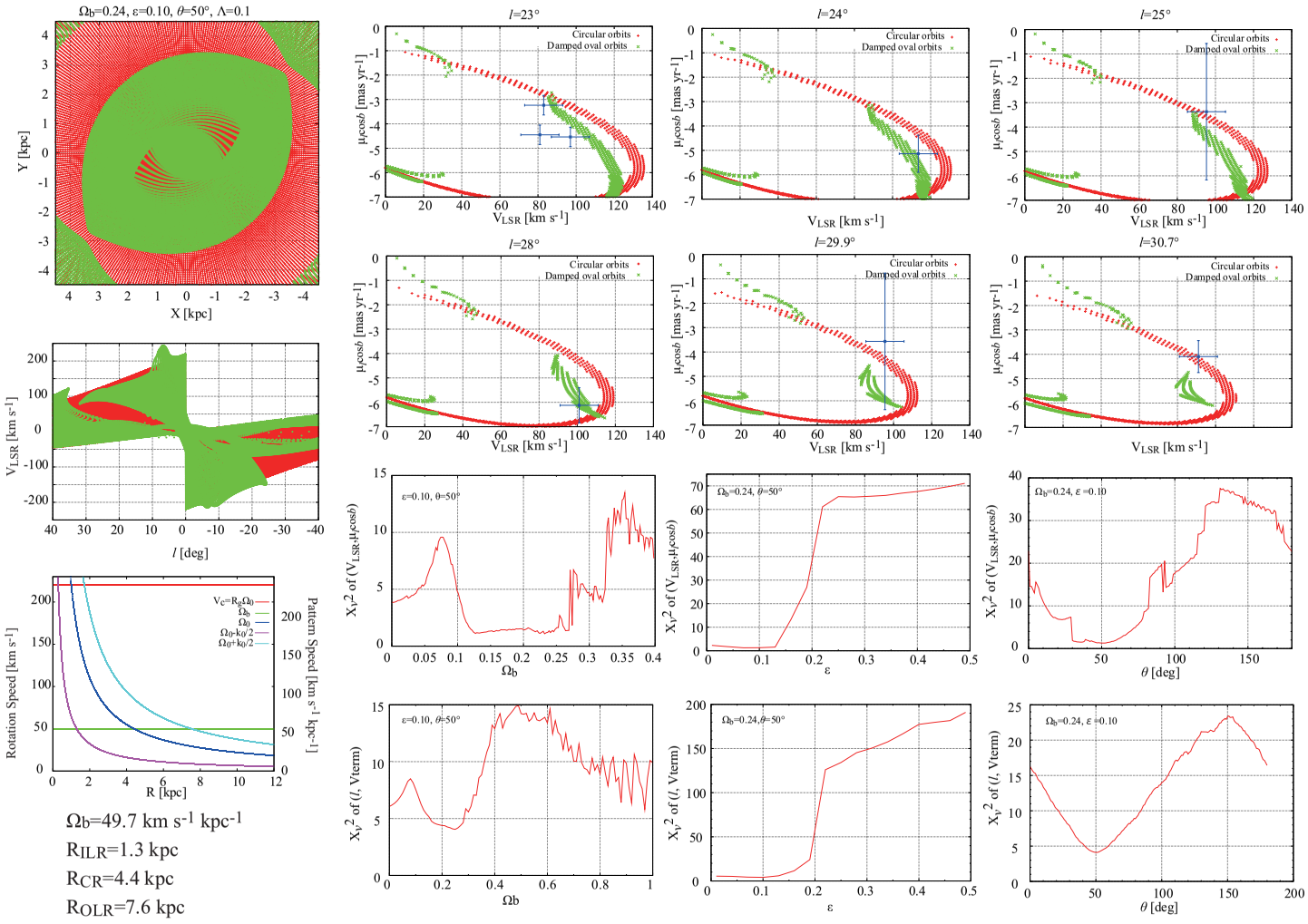

Figure 4.10: Fitting results of the damped oval orbit model with maximum possible value of Ω_b and terminal velocities of H I.

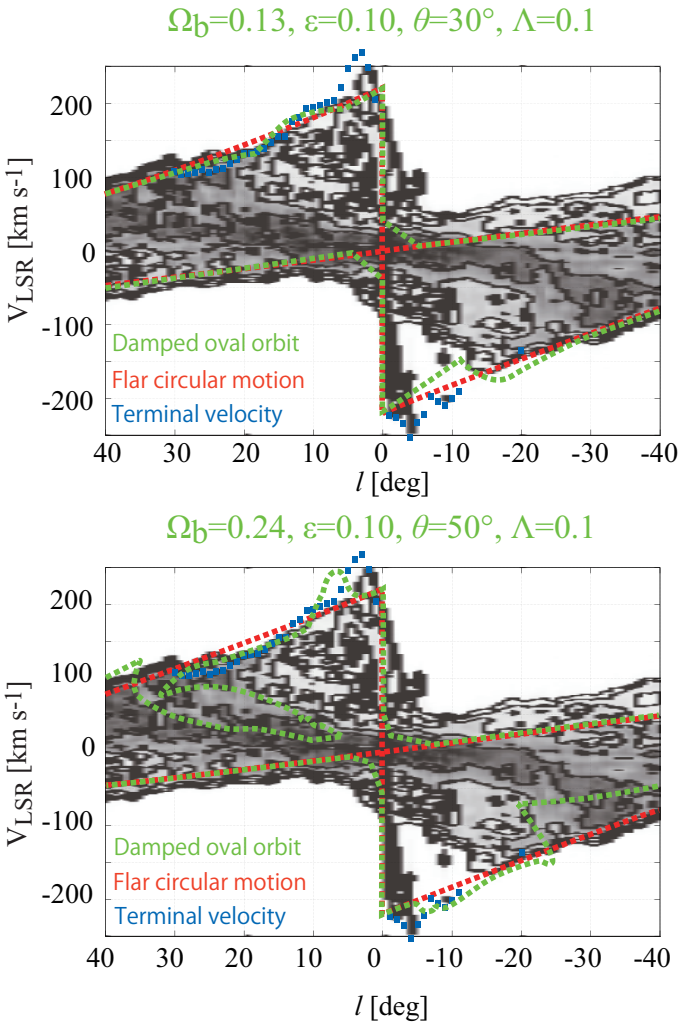

Figure 4.11: The longitude-velocity map of and H I, the flat circular rotation model and the damped oval orbit model with two parameter sets.

Galactic gas. Thus we ideally have to get more samples. For example, figures 4.12 - 4.15 show entire trend each region between each resonance predicted by the damped oval orbit model. However, we only used simple models in this study. Therefore if we want to understand gas proper motions around the Galactic bar with suitable bar parameters, we have to compare with more complicating models which can reproduce the Galactic various structures, like N-body simulation (e.g., Baba et al. (2009, 2010)).

4.6 Summary

We performed astrometric observations with the VERA toward ten 6.7 GHz methanol maser sources associated with star forming regions to investigate the Galactic kinematics around the Galactic bar. The primary results are summarized as follows.

1. We measured absolute proper motions for nine 6.7 GHz methanol maser sources. The proper motions ($\mu_\alpha \cos\delta$ [mas yr^{-1}], μ_δ [mas yr^{-1}]) of these sources are (4.70, −6.72) for G 351.41+0.64, (1.51, −4.57) for G 25.70+0.04, (−2.84±0.35, −5.43±0.63) for G 28.14+0.00, (0.88, −8.77) for G 9.98−0.02, (0.98, −4.51) for G 29.95−0.02, (−1.59±0.61, −3.79±0.42) for G 30.76−0.05, (−1.52±0.40, −4.42±0.30) for G 23.01−0.41, (−1.89±0.62, −4.82±0.53) for G 24.78+0.08, (1.31±1.29, −2.98±0.24) for G 25.65+1.04.

2. The proper motions are $\sim$ 0.5 - 2.0 mas yr^{-1} slower than the flat rotation model with Θ_0 = 220 km s^{-1} in the direction of the galactic longitude at certain systemic velocity for G 23.65−0.127, G 23.44−0.18, G 23.01−0.41, G 28.01+0.00, G 24.78+0.08. Especially for the sources near the Galactic bar, G 23.01−0.41 and G 23.44−0.18, this slower trend could be strong.

3. While circular rotation models cannot reproduce the slower trend of the proper motion in the direction of the galactic longitude, and the l-v map of H I, these observed properties can be well explained by non-circular motion due to the Galactic bar. Thus, our proper motion measurements may also indicates the

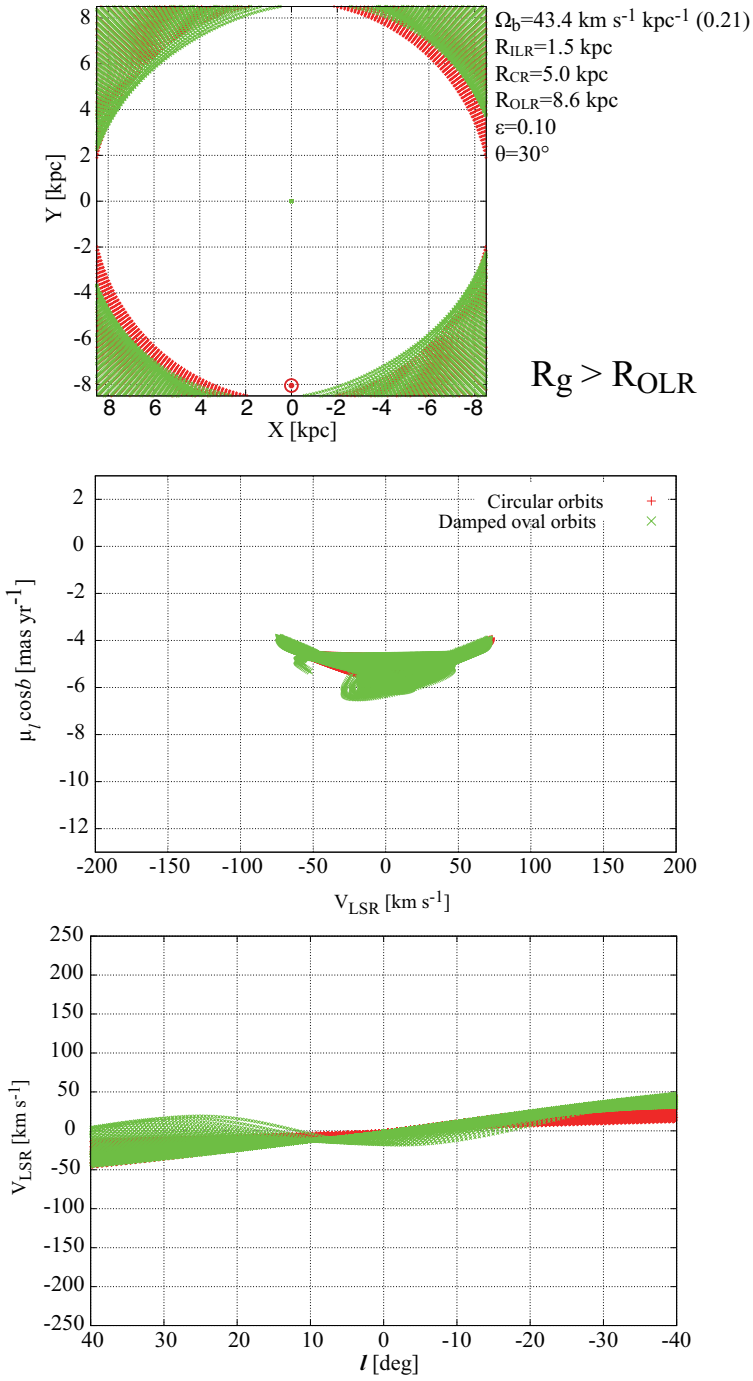

Figure 4.12: (X, Y), $(V_{\rm LSR}, \mu_l \cos b)$, $(l, V_{\rm LSR})$ plots with $l < |90°|$ at $R_g > R_{\rm OLR}$ with the parameter sets of $(\Omega_{\rm b}, \epsilon, \Theta, \Lambda)$=(0.21, 0.1, 30°, 0.1).

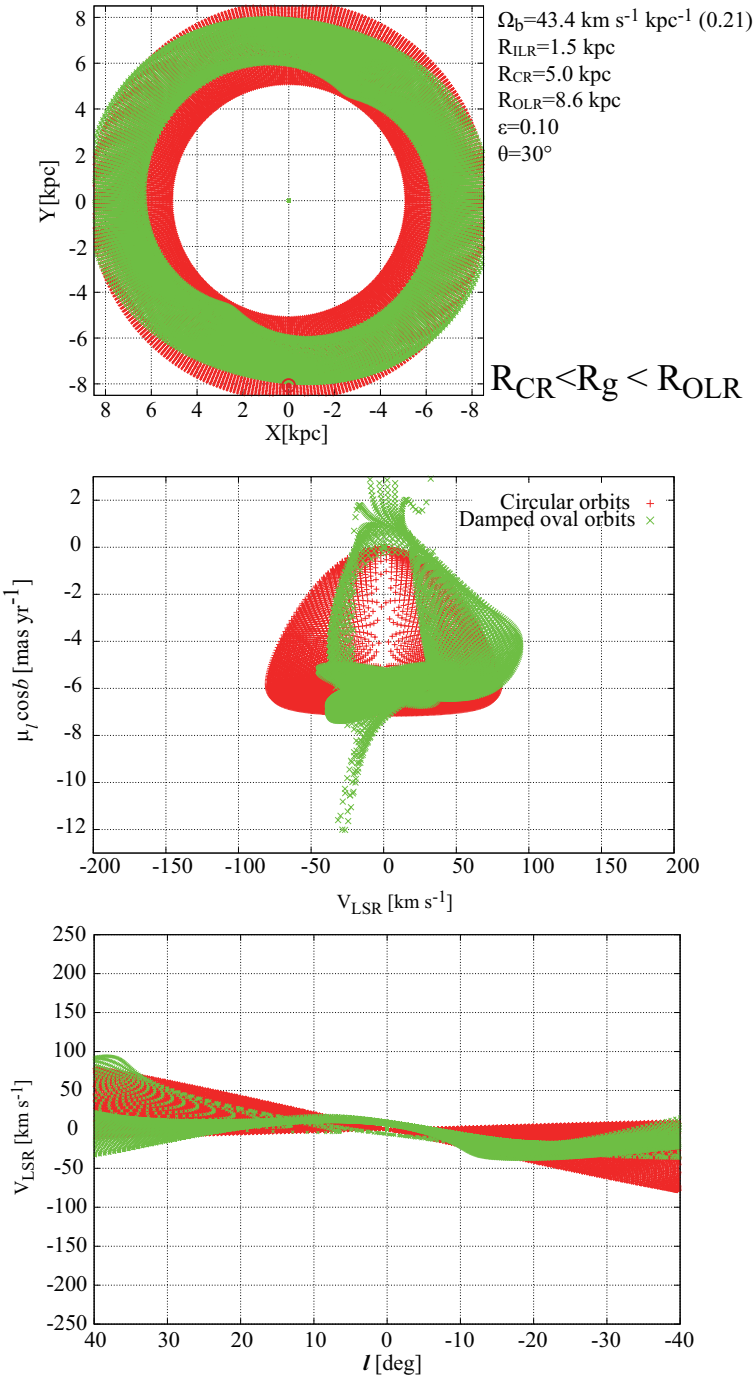

Figure 4.13: $(X,\ Y)$, $(V_{\rm LSR},\ \mu_l \cos b)$, $(l,\ V_{\rm LSR})$ plots with $l < |90°|$ at $R_{\rm CR} < R_{\rm g} < R_{\rm OLR}$ with the parameter sets of $(\Omega_{\rm b},\ \epsilon,\ \Theta,\ \Lambda)$=(0.21, 0.1, 30°, 0.1).

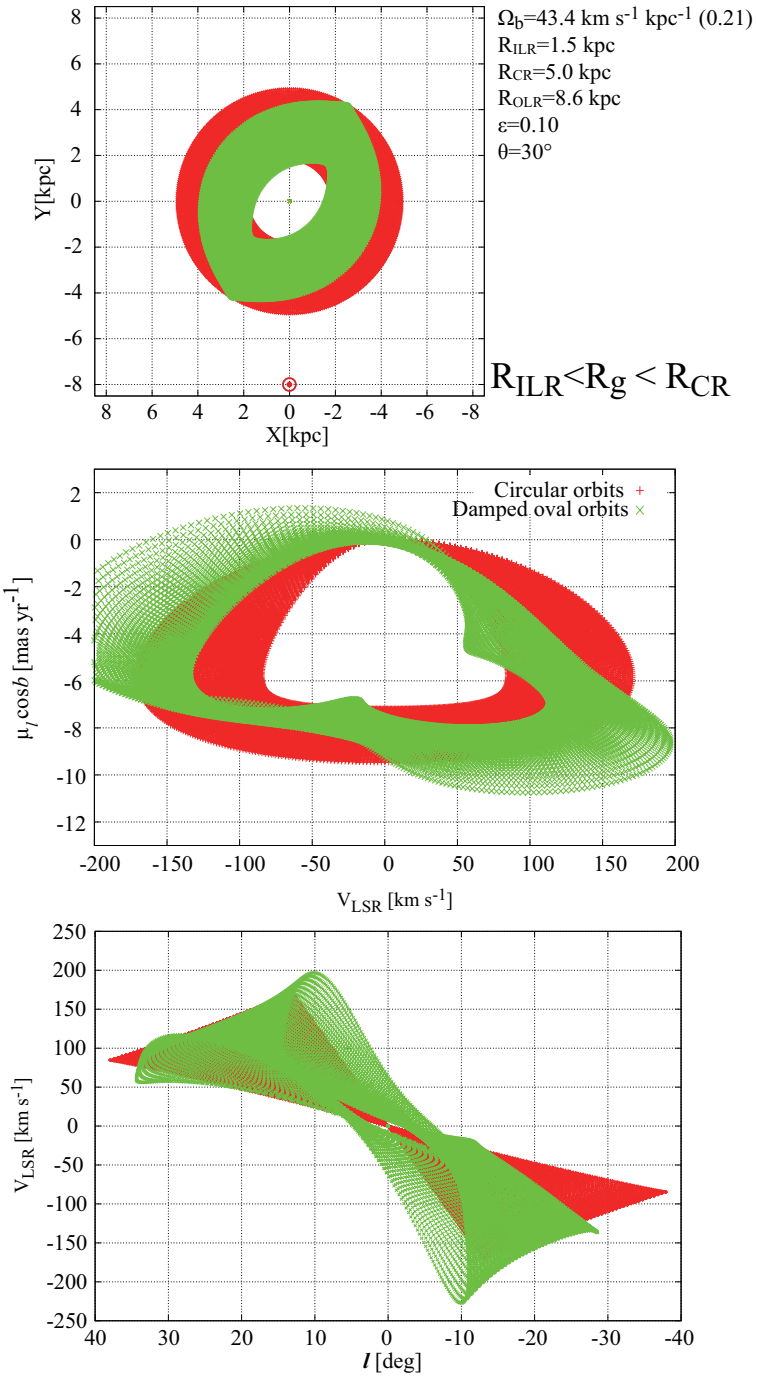

Figure 4.14: (X, Y), $(V_{\rm LSR}, \mu_l \cos b)$, $(l, V_{\rm LSR})$ plots with $l < |90°|$ at $R_{\rm ILR} < R_{\rm g} < R_{\rm CR}$ with the parameter sets of $(\Omega_{\rm b}, \epsilon, \Theta, \Lambda)$=(0.21, 0.1, 30°, 0.1).

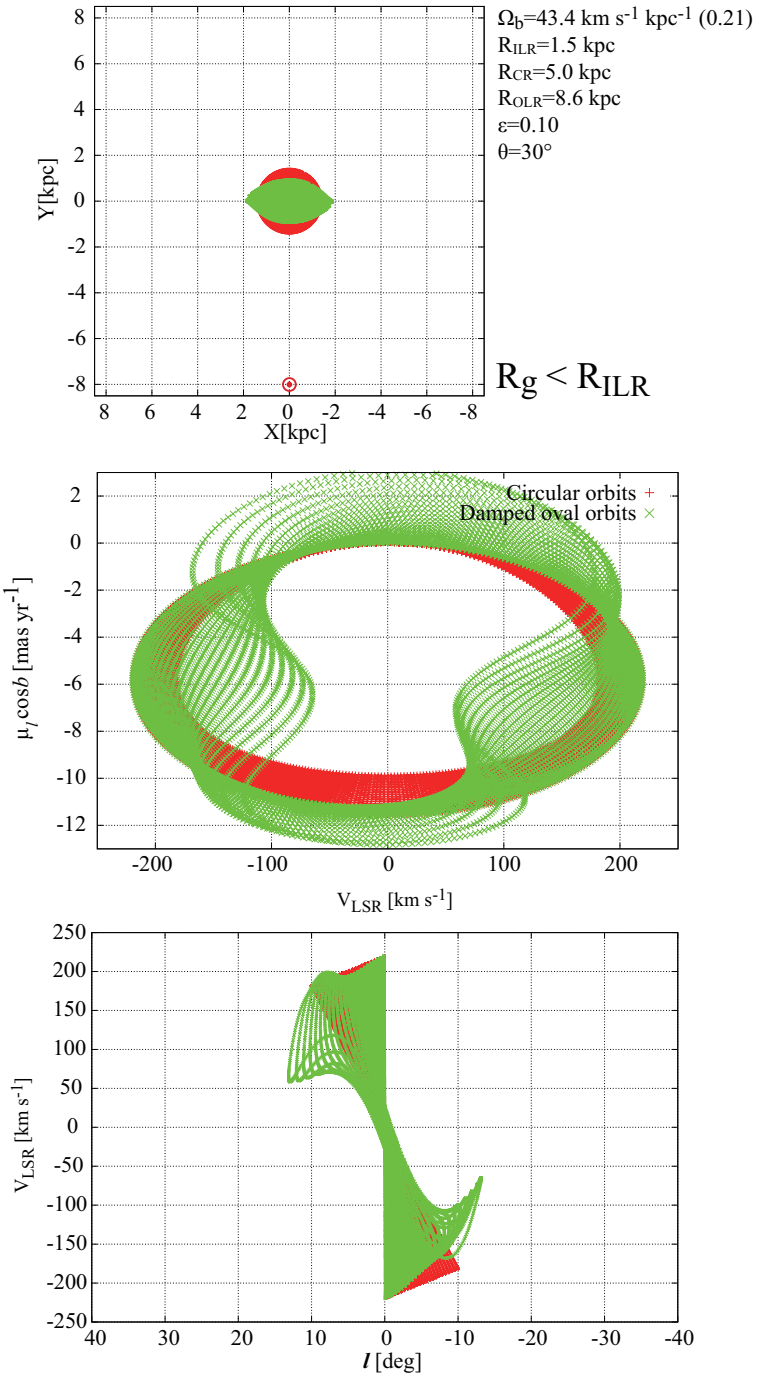

Figure 4.15: (X, Y), $(V_{\rm LSR}, \mu_l \cos b)$, $(l, V_{\rm LSR})$ plots with $l < |90°|$ at $R_{\rm g} < R_{\rm ILR}$ with the parameter sets of $(\Omega_{\rm b}, \epsilon, \Theta, \Lambda)$=(0.21, 0.1, 30°, 0.1).

existence of the Galactic bar, which is the first indication of the Galactic bar based on the absolute astrometry of Galactic maser sources.

Chapter 5

Conclusions

5.1 Conclusions

This thesis has described first results of phase-referencing observations of 6.7 GHz methanol maser sources with the VERA/JVN. First, we test the measurement of an annual parallax and absolute proper motions of 6.7 GHz methanol maser source. The test source was one of the most brightest 6.7 GHz methanol maser source toward the UC H II region of W3(OH). The distance to W3(OH) from the Sun is $1.58^{+0.34}_{-0.24}$ kpc. With the current status of the VERA and the JVN, we could measure annual parallaxes of sources within $\sim$2 kpc far from the Sun. Next, we conducted the fringe check observations to select observable target sources around the Galactic bar. In total, 75 maser sources were observed, and 26 maser sources were detected with signal to noise ratio of more than 5σ at the baseline of more than 1,000 km, corresponding to the detection rate of 35%. In the 26 sources, the 10 sources were not resolved out at the VERA baselines of more than 1,000 km and their reference sources were also detected. Thus these 10 sources were selected for astrometric observations (G 353.4+0.64, G 351.41+0.64, G 30.76−0.05, G 29.95−0.02, G 28.14+0.00, G 25.70−0.04, G 25.65+1.04, G 24.78+0.08, G 23.01−0.41 and G 9.98−0.02). From the results of the astrometric observations, we discussed 3-D motions of the eight sources with the data of five sources from our data (G 24.78+0.08, G 25.70+0.04, G 28.14+0.00, G 29.95−0.02, G 30.76−0.05) and three sources from data of previous

studies (G 23.65−0.127, G 23.01−0.41, G 23.44−0.18). These selected sources have $V_{\rm LSR} > 50$ km s^{-1} and a range of galactic longitude of ∼23° - 30°, and considered to locate around the tip of the Galactic bar. In this discussion, we compered these data with three models of the flat rotation model, the non-flat circular rotation model and the damped oval orbit model. Finally we conclude that while circular rotation models cannot reproduce the slower trend of the proper motions in the direction of the galactic longitude, and the l-v map of H I, these observed properties can be well explained by non-circular motion due to the Galactic bar. Thus, our proper motion measurements also indicates the existence of the Galactic bar, which is the first indication of the Galactic bar based on the absolute VLBI astrometry of Galactic maser sources.

5.2 Future Works

This study suggested that it is more important to increase samples for the wider galactic longitude than increase measurement accuracy of each data points from the limitation by random motion of the Galactic gas. With current status and from this study, more seven 6.7 GHz methanol maser sources can be observed with the VERA/JVN in $|l| < 40°$ and Dec$> -37°$ except no detectable-reference sources. In addition, if detection sensitivity become better for reference sources with wider bandwidth, it is not impossible to take samples with all range in $|l| < 40°$ and Dec$> -37°$. We will get parallaxes for near sources out of ten in chapter 4 within a year, and we will be able to discuss about gas proper motions with the values of distance.

Astrometric observations of 6.7 GHz methanol maser sources are important to study the galactic kinematics. With phase referencing VLBI observations, we are able to measure the mas-scale proper motions and annual parallaxes. Larger number of sources have to be observed to estimate more realistic galactic parameters and/or construct an ideal galactic model. If enough sources are observed, we will be able to understand the Galactic gas motions and the Galactic star formations in more details.

However, 6.7 GHz methanol maser sources are significantly resolved out, and short baselines and high sensitive arrays are important for future observations. In our next step, we are planning the JVN/EAVN observations. With the JVN/EAVN observations, short baselines will be increase and sensitivity also will be improved. This will provide increase of observable sources. Actually, more 7 sources are observable sources with the JVN array. On the other hand, position reference sources are also needed to phase-referencing, and wide-band receiving system is also important. If position reference sources will be detected at the wider range of the galactic longitude around the bar, 6.7 GHz methanol maser sources in the astrometric observations will also be able to cover the wider range of the galactic longitude and comprehensive discussion of the bar will be allowed. Frequency resolution of the correlator is also important for low frequency and narrow spectrum of 6.7 GHz methanol maser sources. In the near future, we will operate with the software correlator for the VERA/JVN data, and the frequency resolution will be substantially improve. By improve the sensitivity and short baselines of VLBI array, we expect that distant SiO maser sources toward the evolved stars also will be able to observe to investigate the Galactic bulge. Thus the investigation of the kinematics of the evolved stars is important to estimate the Galactic potential.

Bibliography

Baba, J., Asaki, Y., Makino, J., Miyoshi, M., Saitoh, T. R., & Wada, K. 2009, ApJ, 706, 471

Baba, J., Saitoh, T. R., & Wada, K. 2010, PASJ, 62, 1413

Babusiaux, C., & Gilmore, G. 2005, MNRAS, 358, 1309

Bally, J., Stark, A. A., Wilson, R. W., & Henkel, C. 1988, ApJ, 324, 223

Bartkiewicz, A., Brunthaler, A., Szymczak, M., van Langevelde, H. J., & Reid, M. J. 2008, A&A, 490, 797

Baudry, A., Herpin, F., & Lucas, R. 1998, A&A, 335, 654

Baudry, A., Menten, K. M., Walmsley, C. M., & Wilson, T. L. 1993, A&A, 271, 552

Beaulieu, S. F., Freeman, K. C., Kalnajs, A. J., Saha, P., & Zhao, H. 2000, AJ, 120, 855

Benjamin, R. A., et al. 2005, ApJL, 630, L149

Binney, J., Gerhard, O. E., Stark, A. A., Bally, J., & Uchida, K. I. 1991, MNRAS, 252, 210

Binney, J., Gerhard, O., & Spergel, D. 1997, MNRAS, 288, 365

Binney, J., Tremaine, S. 2008, Galactic Dynamics Second Edition (New Jersey, Princeton University Press), 75

Binney, J., Tremaine, S. 2008, Galactic Dynamics Second Edition (New Jersey, Princeton University Press), ch. 3.3.3

Bissantz, N., Englmaier, P., Binney, J., & Gerhard, O. 1997, MNRAS, 289, 651

Bissantz, N., Englmaier, P., & Gerhard, O. 2003, MNRAS, 340, 949

Blitz, L., & Spergel, D. N. 1991a, ApJ, 370, 205

Blitz, L., & Spergel, D. N. 1991b, ApJ, 379, 631

Blitz, L. 1993, Back to the Galaxy, 278, 98

Blitz, L., Binney, J., Lo, K. Y., Bally, J., & Ho, P. T. P. 1993, Nature, 361, 417

Brunthaler, A., Reid, M. J., Menten, K. M., Zheng, X. W., Moscadelli, L., & Xu, Y. 2009, ApJ, 693, 424

Burton, W. B., & Liszt, H. S. 1983, A&AS, 52, 63

Burton, W. B., & Liszt, H. S. 1993, A&A, 274, 765

Bloemhof, E. E., Reid, M. J., & Moran, J. M. 1992, ApJ, 397, 500

Brand, J., et al. 1994, A&AS, 103, 541

Cabrera-Lavers, A., Hammersley, P. L., González-Fernández, C., López-Corredoira, M., Garzón, F., & Mahoney, T. J. 2007, A&A, 465, 825

Campbell, M. F., Lester, D. F., Harvey, P. M., & Joy, M. 1989, ApJ, 345, 298

Caswell, J. L. 2009, PASA, 26, 454

Caswell, J. L., et al. 2010, MNRAS, 404, 1029

Chikada, Y., et al. 1991, in Frontiers of VLBI ed. H. Hirabayashi, M. Inoue, & H. Kobayashi (Tokyo: Universal Academy Press), 79

Clemens, D. P. 1985, ApJ, 295, 422

Combes, F. 1996, Unsolved Problems of the Milky Way, 169, 133

Comoretto, G., et al. 1990, A&AS, 84, 179

Churchwell, E., et al. 2009, PASP, 121, 213

Dame, T., M., Hartmann, D., & Thaddeus, P. 2001, ApJ, 547, 792

Debattista, V. P., Gerhard, O., & Sevenster, M. N. 2002, MNRAS, 334, 355

Dehnen, W. 1999, ApJL, 524, L35

Dehnen, W. 2000, AJ, 119, 800

Desmurs, J. F., Baudry, A., Wilson, T. L., Cohen, R. J., & Tofani, G. 1998, A&A, 334, 1085

De Buizer, J. M., Piña, R. K., & Telesco, C. M. 2000, ApJS, 130, 437

Deguchi, S., Fujii, T., Izumiura, H., Kameya, O., Nakada, Y., Nakashima, J.-i., Ootsubo, T., & Ukita, N. 2000a, ApJS, 128, 571

Deguchi, S., Fujii, T., Izumiura, H., Kameya, O., Nakada, Y., & Nakashima, J.-i. 2000b, ApJS, 130, 351

Deguchi, S., Fujii, T., Nakashima, J.-I., & Wood, P. R. 2002, PASJ, 54, 719

Deguchi, S., Shimoikura, T., Koike, K. 2010, PASJ, 62, 525

de Vaucouleurs, G. 1964, in Kerr F. J., eds, The Galaxy and The Magellanic Clouds. Aust. Sci., Canberra, p. 195

de Vaucouleurs, G., Pence, W. D. 1978, AJ, 83, 1163

Diamond, P. J., & Kemball, A. J. 2003, ApJ, 599, 1372

Dickel, H. R., & Goss, W. M. 1987, A&A, 185, 271

Dwek, E., et al. 1995, ApJ, 445, 716

Dreher, J. W., & Welch, WM. J. 1981, ApJ, 245, 857

Elitzur, M. 1992, Astronomical Masers (Netherlands, Kluwer Academic Publishers)

Englmaier, P., & Gerhard, O. 1999, MNRAS, 304, 512

Englmaier, P., & Gerhard, O. 2006, Celestial Mechanics and Dynamical Astronomy, 94, 369

Etoka, S., Cohen, R. J., & Gray, M. D. 2005, MNRAS, 360, 1162

Feast, M. W., & Whitelock, P. A. 2000, MNRAS, 317, 460

Feigelson, E. D., & Townsley, L. K. 2008, ApJ, 673, 354

Fish, V. L., Brisken, W. F., & Sjouwerman, L. O. 2006, ApJ, 647, 418

Fish, V. L., Sjouwerman, L. O. 2007, ApJ, 668, 331

Foster, T., & Cooper, B. 2010, arXiv:1009.3220

Fujii, T., Deguchi, S., Ita, Y., Izumiura, H., Kameya, O., Miyazaki, A., & Nakada, Y. 2006, PASJ, 58, 529

Fux, R. 1997, A&A, 327, 983

Fux, R. 1999, A&A, 345, 787

Gerhard, O. 2002, in G.S. Da Costa, H. Jerjen, eds., ASP Conf. Ser. 273: The Dynamics, Structure & History of Galaxies, 73

Gerhard, O. 2010, arXiv:1003.2489, invited talk to appear in "Tumbling, twisting, and winding galaxies: Pattern speeds along the Hubble sequence", E. M. Corsini and V. P. Debattista (eds.), Memorie della Societa'Astronomica Italiana

Goedhart, S., Gaylard, M. J., & van der Walt, D. J. 2004, MNRAS, 355, 553

Goedhart, S., Minier, V. Gaylard, M. J., & van der Walt, D. J. 2005, MNRAS, 356, 839

Gonidakis, I., Diamond, P. J., & Kemball, A. J. 2006 AIP Conf. Proc., 848, 333

Green, J. A., et al. 2009, MNRAS, 392, 783

Green, J. A., et al. 2010, MNRAS, 409, 913

Guilloteau, S., Stier, M. T., & Downes, D. 1983, A&A, 126, 10

Gyuk, G. 1999, ApJ, 510, 205

Habing, H. J., Sevenster, M. N., Messineo, M., van de Ven, G., & Kuijken, K. 2006, A&A, 458, 151

Hachisuka, K., Brunthaler, A., Menten, K. M., Reid, M. J., Imai, H., Hagiwara, Y., Miyoshi, M., Horiuchi, S., & Sasao, T. 2006, ApJ, 645, 337

Hammersley, P. L., Garzón, F., Mahoney, T. J., López-Corredoira, M., & Torres, M. A. P. 2000, MNRAS, 317, L45

Harper, D. A. 1974, ApJ, 192, 557

Hartmann, D., & Burton, W. B. 1997, Atlas of Galactic Neutral Hydrogen (Cambridge: Cambridge University Press)

Harvey-Smith, L., & Cohen, R. J. 2006, MNRAS, 371, 1550

Harvey-Smith, L., & Cohen, R. J. 2005, MNRAS, 356, 637

Hirota, T., et al. 2008, PASJ, 60, 961

Honma, M., et al. 2007, PASJ, 59, 889

Honma, M., Tamura, Y., & Reid, M. J. 2008b, PASJ, 60, 951

Izumiura, H., et al. 1993, Galactic Bulges, 153, 303

Izumiura, H., Deguchi, S., Hashimoto, O., Nakada, Y., Onaka, T., Ono, T., Ukita, N., & Yamamura, I. 1994, ApJ, 437, 419

Izumiura, H., et al. 1995a, ApJS, 98, 271

Izumiura, H., Deguchi, S., Hashimoto, O., Nakada, Y., Onaka, T., Ono, T., Ukita, N., & Yamamura, I. 1995b, ApJ, 453, 837

Kawamura, J. H., & Masson, C. R. 1998, ApJ, 509, 270

Kamohara, R., et al. 2010, A&A, 510, 69

Keto, E. R., Welch, W. J., Reid, M. J., & Ho, P. T. P. 1995, ApJ, 444, 765

Kerr, F. J., Bowers, P. F., Jackson P. D., Kerr, M. 1986, A&AS, 66, 373

Kim, S.-J., Kim, H.-D., Lee, Y., Minh, Y. C., Balasubramanyam, R., Burton, M. G., Millar, T. J., & Lee, D.-W. 2006, ApJS, 162, 161

Kim, M., et al. 2008, PASJ, 60, 991

Kozłowski, S., Woźniak, P. R., Mao, S., Smith, M. C., Sumi, T., Vestrand, W. T., & Wyrzykowski, Ł. 2006, MNRAS, 370, 435

Kuijken, K., & Rich, R. M. 2002, AJ, 124, 2054

Kurayama, T., Sasao, T., & Kobayashi, H. 2005, ApJ, 627, L49

Levine, E. S., Heiles, C., & Blitz, L. 2008, ApJ, 679, 1288

Liszt, H. S., & Burton, W. B. 1978, ApJ, 226, 790

McClure-Griffiths, N. M., Dickey, J. M., Gaensler, B. M., Green, A. J., Haverkorn, M., & Strasser, S. 2005, ApJS, 158, 178

McClure-Griffiths, N. M., & Dickey, J. M. 2007, ApJ, 671, 427

McWilliam, A., & Zoccali, M. 2010, ApJ, 724, 1491

Manabe, S., & Miyamoto, M. 1975, PASJ, 27, 35

Matsumoto, N., et al. 2008, PASJ, 60, 1039

Mendez, R. A., Rich, R. M., van Altena, W. F., Girard, T. M., van den Bergh, S., & Majewski, S. R. 1996, The Galactic Center, 102, 345

Menten, K. M., 1991a, ASPC, 16, 119

Menten, K. M., 1991b, ApJ, 380, L75

Menten, K. M., Reid, M. J., Pratap, P., Moran, J. M., & Wilson, T. L. 1992, ApJ, 401, L39

Minchev, I., Nordhaus, J., & Quillen, A. C. 2007, ApJ, 664, L31

Minier, V., Booth, R. S., & Conway, J. E. 2000, A&A, 362, 1093

Minniti, D. 1996, ApJ, 459, 579

Minniti, D., & Zoccali, M. 2008, IAUS, 245, 323

Moscadelli, L., Menten, K. M., Walmsley, C. M., & Reid, M. J. 1999, ApJ, 519, 244

Moscadelli, L., Menten, K. M., Walmsley, C. M., & Reid, M. J. 2002, ApJ, 564, 813

Moscadelli, L., Xu, Y., & Chen, X. 2010, ApJ, 716, 1356

Mould, J., "Galactic Bulge" Encyclopedia of Astronomy and Astrophysics, Inst. of Physics Publishing, 2001, v.1

Nakada, Y., Onaka, T., Yamamura, I., Deguchi, S., Hashimoto, O., Izumiura, H., & Sekiguchi, K. 1991, Nature, 353, 140

Nakada, Y., Onaka, T., Yamamura, I., Deguchi, S., Ukita, N., & Izumiura, H. 1993, PASJ, 45, 179

Nakagawa, A., et al. 2008, PASJ, 60, 1013

Nakanishi, H., & Sofue, Y. 2003, PASJ, 55, 191

Nakanishi, H., & Sofue, Y. 2006, PASJ, 58, 847

Nikolaev, S., & Weinberg, M. D. 1997, ApJ, 487, 885

Nishiyama, S., et al. 2005, ApJ, 621, L105

Norris, R. P., Booth, R. S., & Diamond, P. J. 1982, MNRAS, 201, 209

Paczynski, B., Stanek, K. Z., Udalski, A., Szymanski, M., Kaluzny, J., Kubiak, M., Mateo, M., & Krzeminski, W. 1994, ApJL, 435, L113

Pandian, J. D., Goldsmith, P. F, & Deshpande, A. A. 2007, ApJ, 656, 255

Pestalozzi, M. R., Chrysostomou, A., Collett, J. L., Minier, V., Conway, J., & Booth, R. S 2007, 463, 1009

Pestalozzi, M. R., Minier, V., & Booth, R. S. 2005, A&A432, 737

Rattenbury, N. J., Mao, S., Sumi, T., & Smith, M. C. 2007a, MNRAS, 378, 1064

Rattenbury, N. J., Mao, S., Sumi, T., & Smith, M. C. 2007b, MNRAS, 382, 1376

Reid, M. J., Myers, P. C., & Bieging, J. H. 1987, ApJ, 312, 830

Reid, M. J., Haschick, A. D., Burke, B. F., Moran, J. M., Johnston, K. J., & Swenson, G. W., Jr. 1980, ApJ, 239, 89

Reid, M. J., Schneps, M. H., Moran, J. M., Gwinn, C. R., Genzel, R., Downes, D., & Rönnäng, B. 1988, ApJ, 330, 809

Reid, M, J., et al. 2009a, ApJ, 700, 137

Reid, M. J., Menten, K. M., Zheng, X. W., Brunthaler, A., & Xu, Y. 2009b, ApJ, 705, 1548

Reid, M. J., Brunthaler, A., Menten, K. M., Loinard, L., & Wrobel, J. 2009c, arXiv:0902.3932

Rich, R. M. 1998, IAUS, 184, 11

Rodriguez-Fernandez, N. J., & Combes, F. 2008, A&A, 489, 115

Rygl, K. L. J., Brunthaler, A., Reid, M. J., Menten, K. M., van Langevelde, H. J., & Xu, Y. 2010, A&A, 511, A2

Sakamoto, K., Okumura, S. K., Ishizuki, S., & Scoville, N. Z. 1999, ApJS, 124, 403

Sanna, A., Reid, M. J., Moscadelli, L., Dame, T. M., Menten, K. M., Brunthaler, A., Zheng, X. W., & Xu, Y. 2009, A&A, 706, 464

Sato, M., Hirota, T., Reid, M. J., Honma, M., Kobayashi, H., Iwadate, K., Miyaji, T., & Shibata, K. M. 2010, PASJ, 62, 287

Seth, A. C., Greenhill, L. J., & Holder, B. P. 2002, ApJ, 581, 325

Sevenster, M. N. 1996, IAU Colloq. 157: Barred Galaxies, 91, 536

Simonson, S. C., III, & Mader, G. L. 1973, A&A, 27, 337

Soto, M., Kuijken, K. H., & Lub, J. 2007, Island Universes - Structure and Evolution of Disk Galaxies, 153

Sjouwerman, L. O., Messineo, M., & Habing, H. J. 2003, Astronomische Nachrichten Supplement, 324, 73

Spaenhauer, A., Jones, B. F., & Whitford, A. E. 1992, AJ, 103, 297

Sugiyama, K., Fujisawa, K., Doi, A., Honma, M., Isono, Y., Kobayashi, H., Mochizuki, N., & Murata, Y. 2008a, PASJ, 60, 1001

Sugiyama, K., Fujisawa, K., Doi, A., Homna, M., Kobayashi, H., Bushimata, T., Mochizuki, N., & Murata, Y. 2008b, PASJ, 60, 23

Stanek, K. Z., Udalski, A., Szymanski, M., Kaluzny, J., Kubiak, M., Mateo, M., & Krzeminski, W. 1997, ApJ, 477, 163

Szymczak, M., & Kus, A. J. 2000, A&A, 360, 311

Szymczak, M., Kus, A. J., Hrynek, G., Kępa, A., & Pazderski, E. 2002, A&A, 392, 277

Valdettaro, R., et al. 2001, A&A, 368, 845

Vieira, K., et al. 2007, AJ, 134, 1432

Wada, K. 1994, PASJ, 46, 165

Wada, K., Taniguchi, Y., Habe, A., & Hasegawa, T. 1994, ApJL, 437, L123

Walsh, A. J., Burton, M. G., Hyland, A. R., & Robinson, G. 1998, MNRAS, 301, 640

Weiland, J. L., et al. 1994, ApJL, 425, L81

Weinberg, M. D. 1992a, ApJ, 384, 81

Weinberg, M. D. 1992b, ApJL, 392, L67

Weiner, B. J., & Sellwood, J. A. 1999, ApJ, 524, 112

Whitelock, P. 1992, Variable Stars and Galaxies, in honor of M. W. Feast on his retirement, 30, 11

Wilner, D. J., Reid, M. J., & Menten, K. M. 1999, ApJ, 513, 775

Wright, M. M., Gray, M. D., & Diamond, P. J. 2004a, MNRAS, 350, 1272

Wright, M. M., Gray, M. D., & Diamond, P. J. 2004b, MNRAS, 350, 1253

Xu, Y., Reid, M. J., Zheng, X., & Menten, K. M. 2006, Science, 351, 54

Xu, Y., Li, J. J., Hachisuka, K., Pandian, J. D., Menten, K. M., & Henkel, C. 2008, A&A, 485, 729

Zhao, H., & Mao, S. 1996, MNRAS, 283, 1197

Zhao, H., Rich, R. M., & Spergel, D. N. 1996, MNRAS, 282, 175

Appendix A

Spectra and Maps of the 6.7 GHz Methanol Maser Sources in Chapter 4

Here we present the cross power spectra and spacial distribution maps of phase-referencing of ten sources observed with VERA in chapter 4.

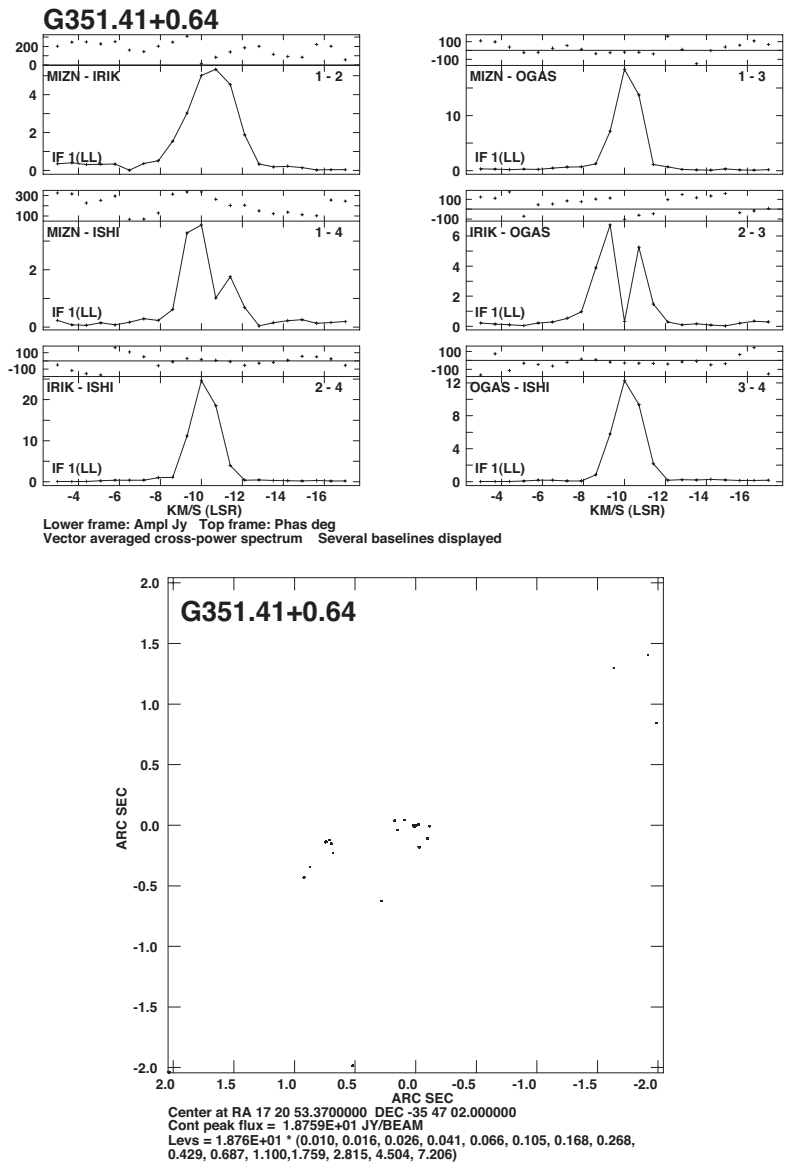

Figure A.1: Top: Cross power spectra of G 351.41+0.64. Bottom: A velocity integrated map of G 351.41+0.64.

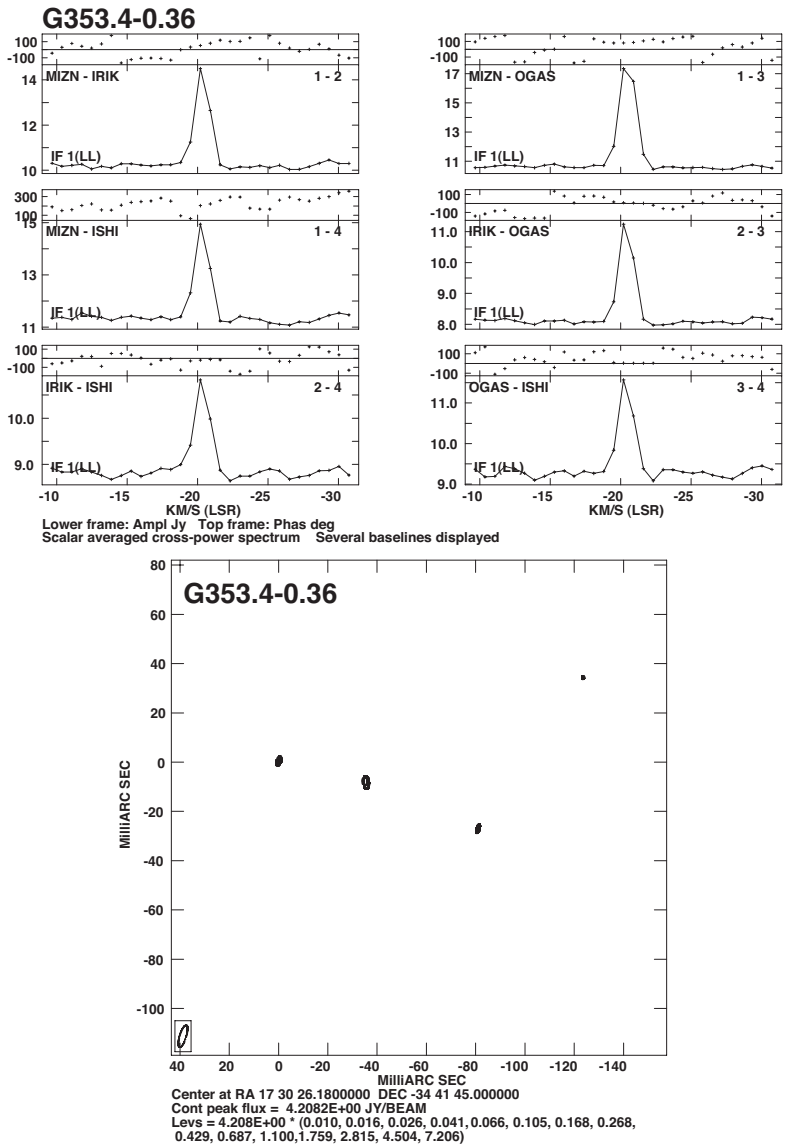

Figure A.2: Top: Cross power spectra of G 353.4−0.36. Bottom: A velocity integrated map of G 353.4−0.36.

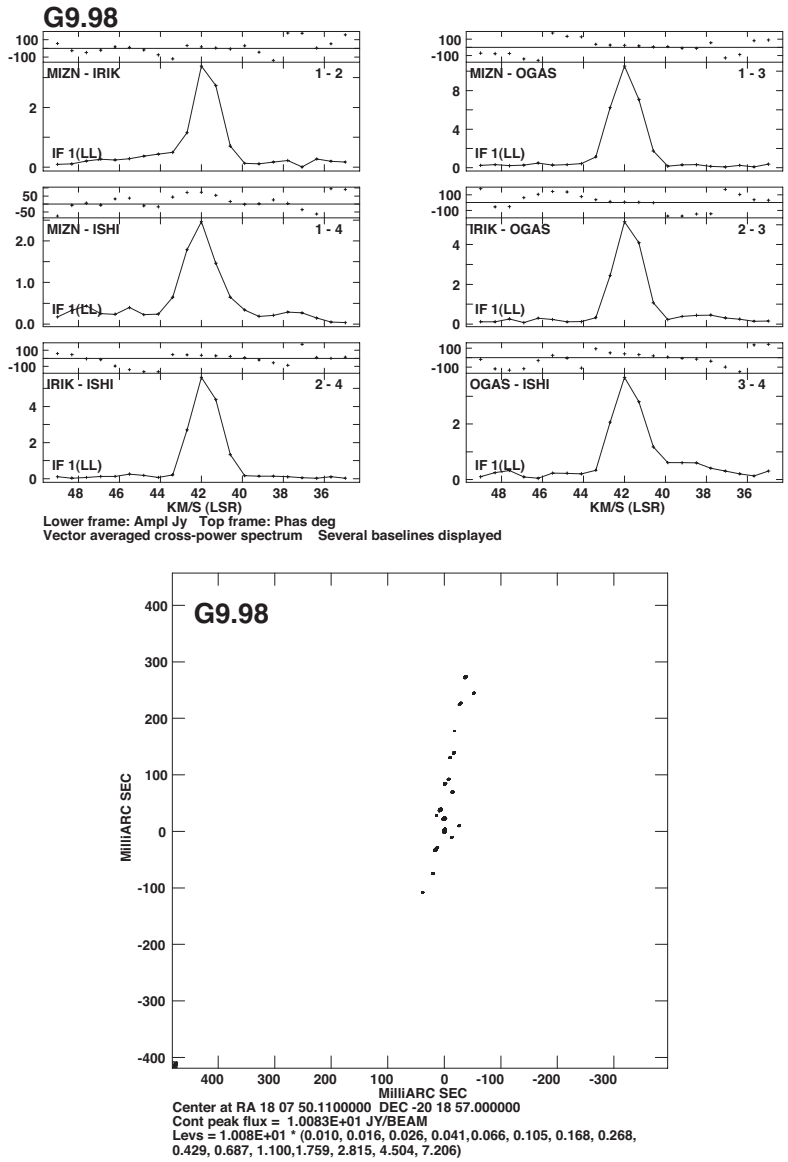

Figure A.3: Top: Cross power spectra of G 9.98−0.02. Bottom: A velocity integrated map of G 9.98−0.02.

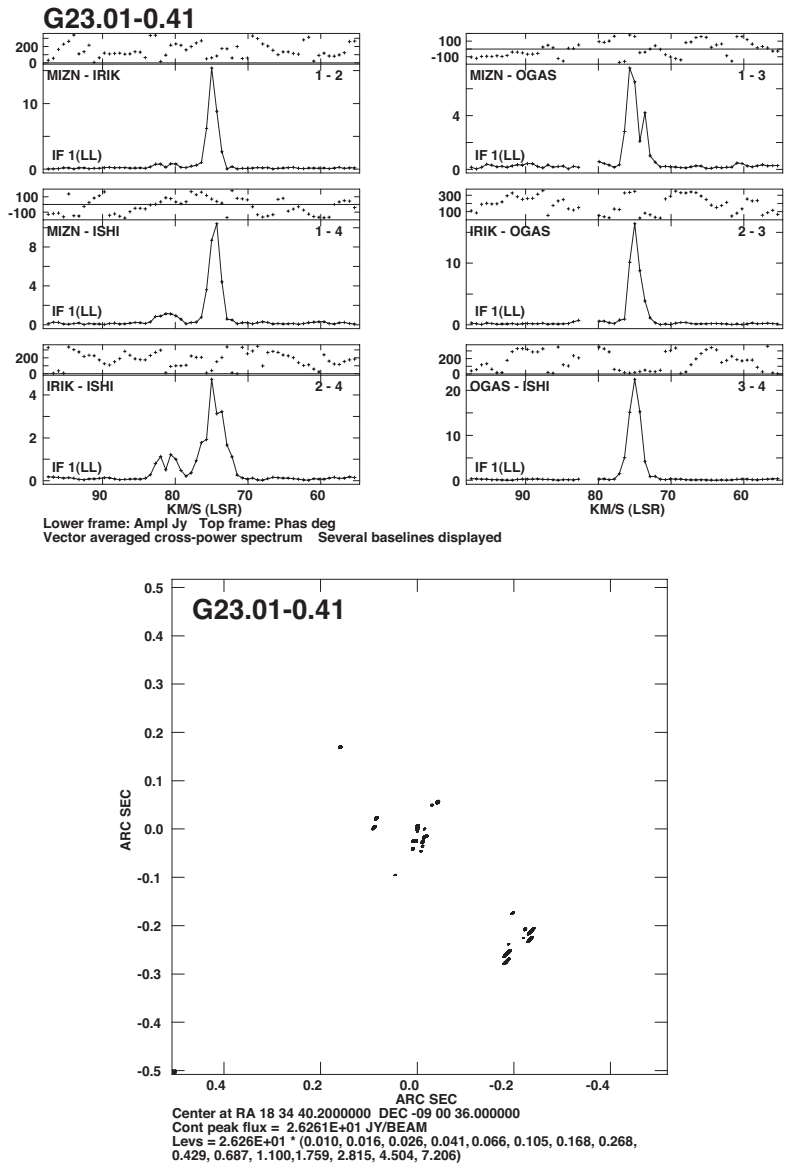

Figure A.4: Top: Cross power spectra of G 23.01−0.41. Bottom: A velocity integrated map of G 23.01−0.41.

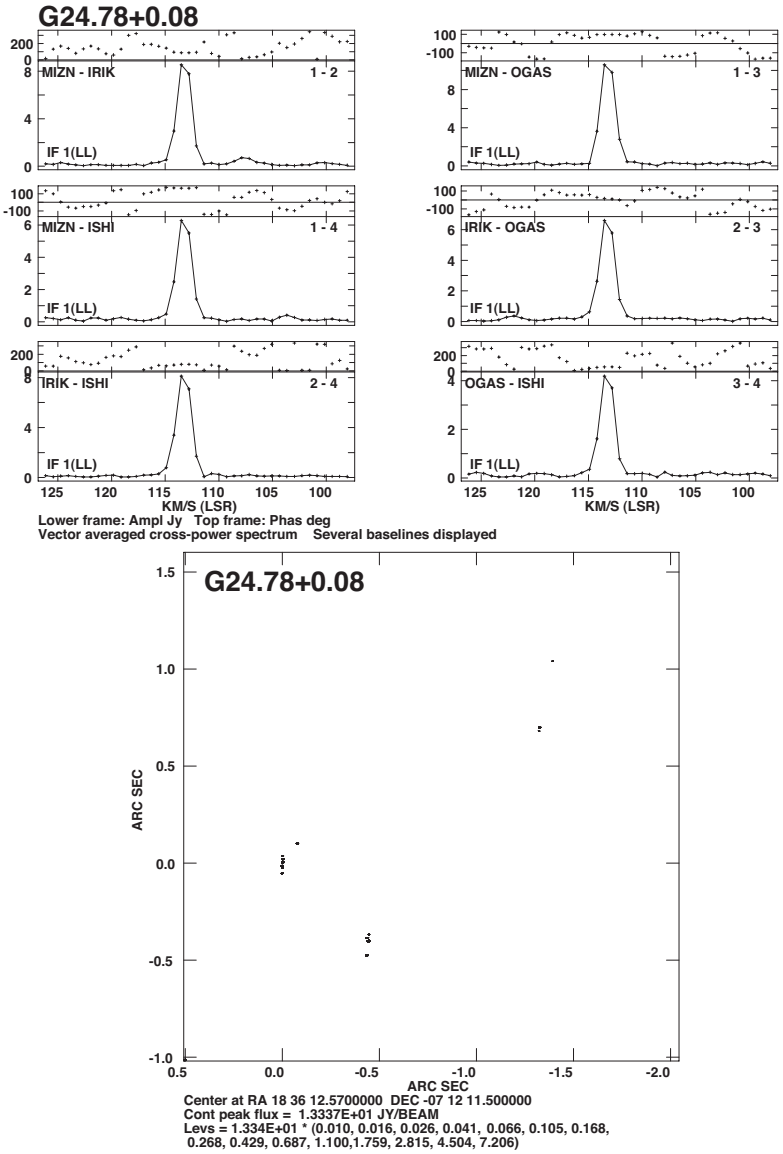

Figure A.5: Top: Cross power spectra of G 24.78+0.08. Bottom: A velocity integrated map of G 24.78+0.08.

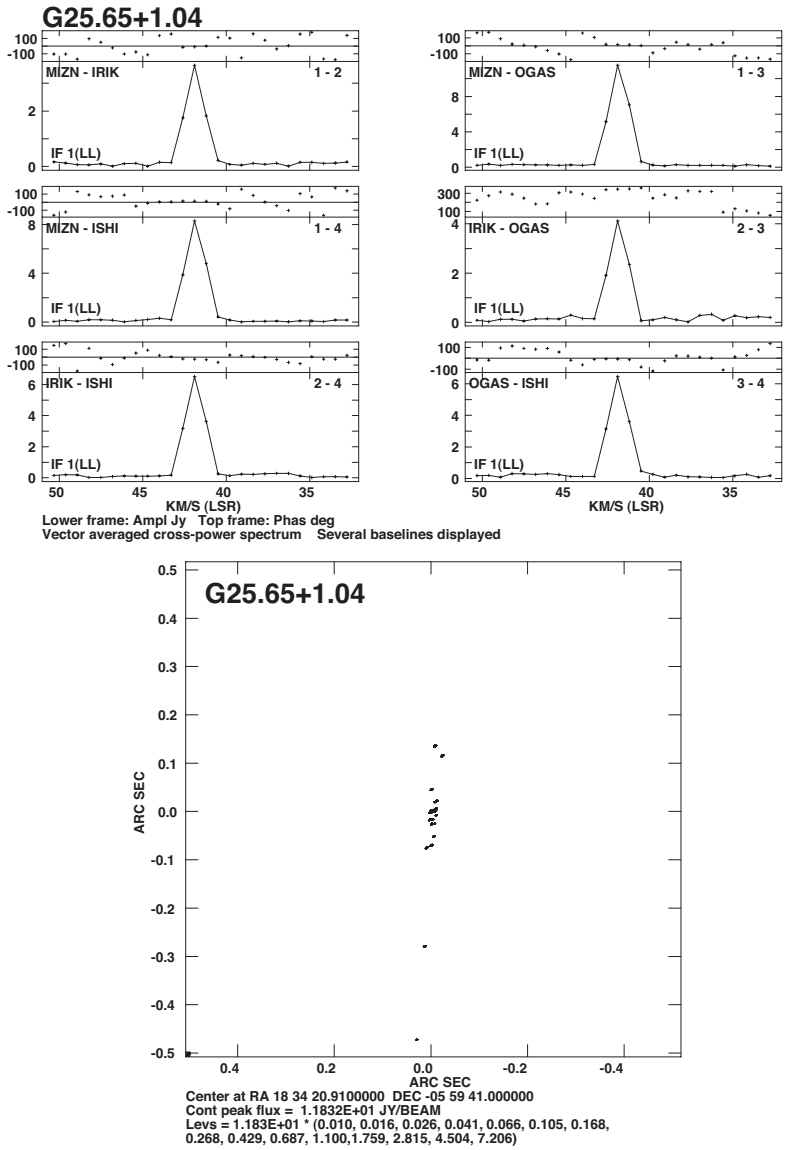

Figure A.6: Top: Cross power spectra of G 25.65+1.04. Bottom: A velocity integrated map of G 25.65+1.04.

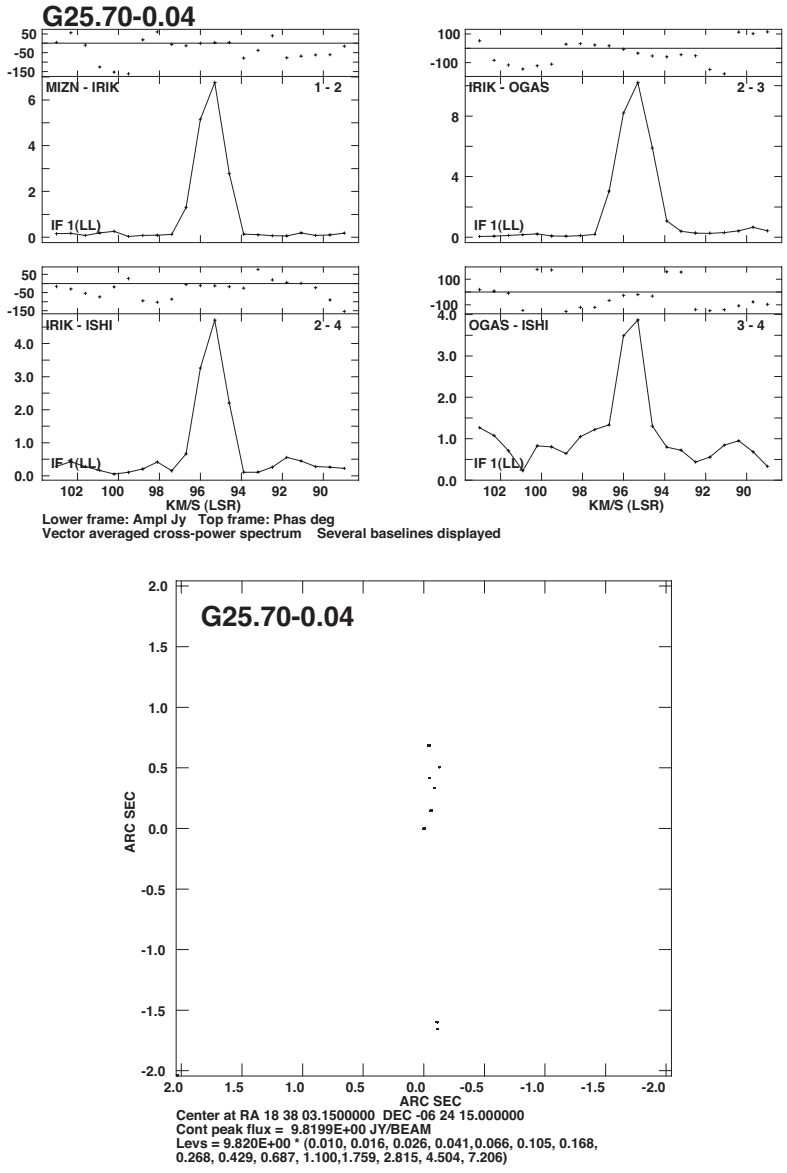

Figure A.7: Top: Cross power spectra of G 25.70−0.04. Bottom: A velocity integrated map of G 25.70−0.04.

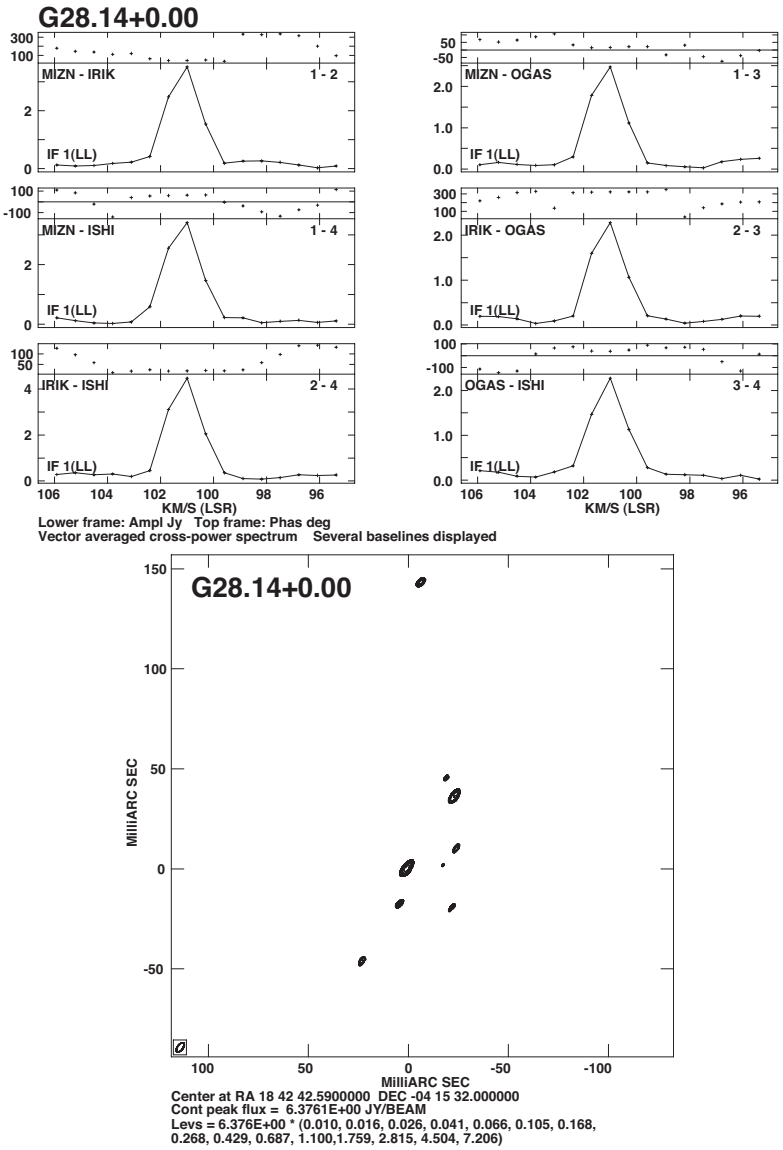

Figure A.8: Top: Cross power spectra of G 28.14+0.00. Bottom: A velocity integrated map of G 28.14+0.00.

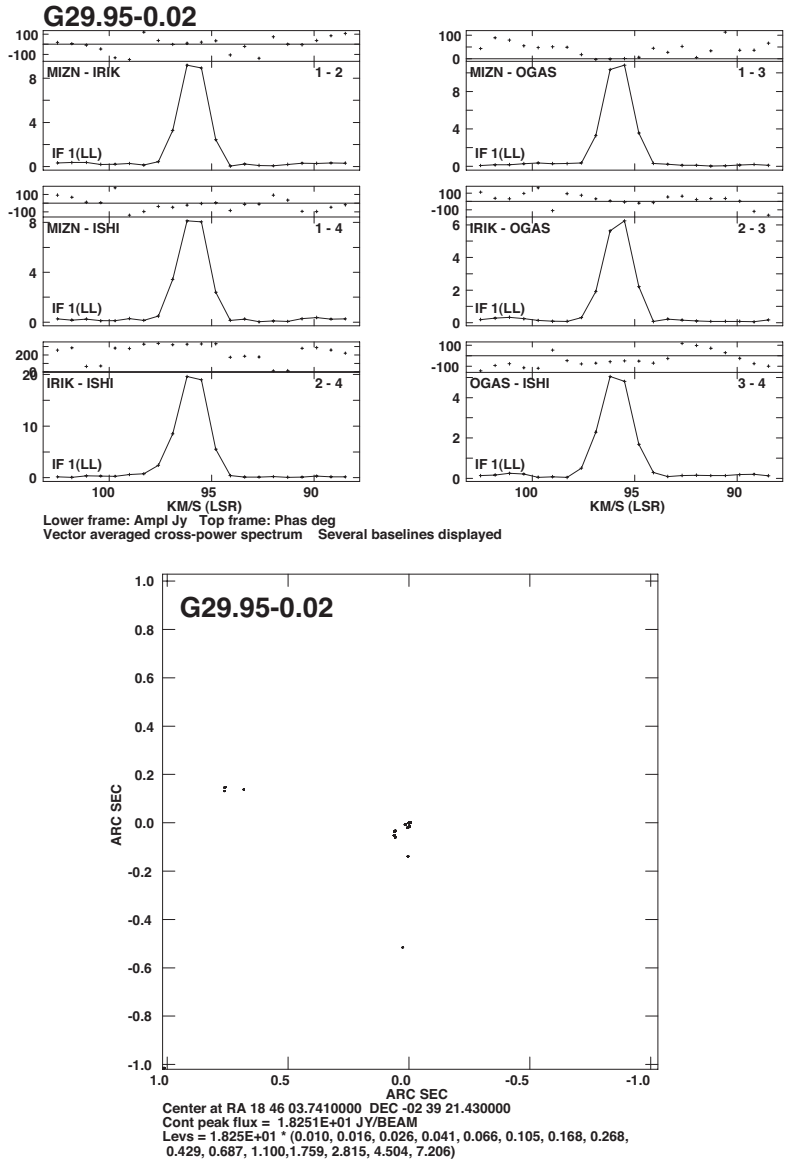

Figure A.9: Top: Cross power spectra of G 29.95−0.02. Bottom: A velocity integrated map of G 29.95−0.02.

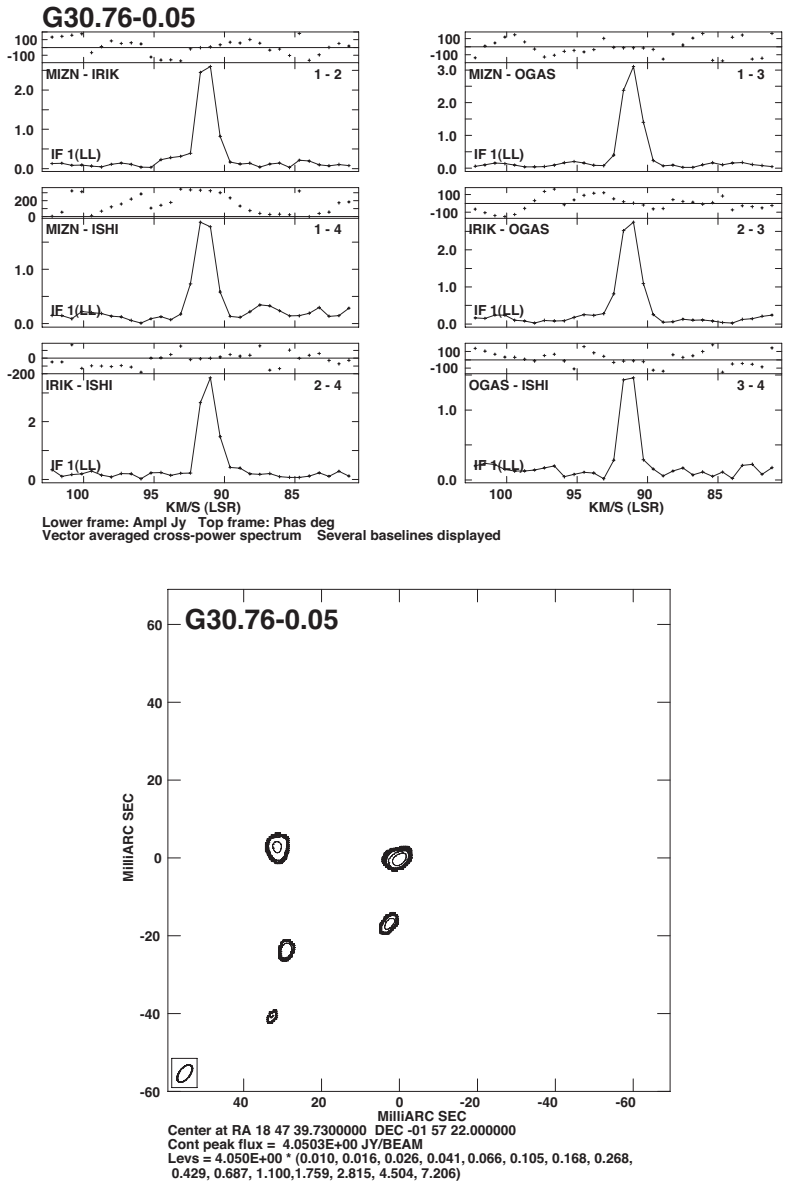

Figure A.10: Top : Cross power spectra of G 30.76−0.05. Bottom: A velocity integrated map of G 30.76−0.05.